Tensor Tomography

Desai, Naeem M

2018

MIMS EPrint: **2018.1**

ISSN 1749-9097

TENSOR TOMOGRAPHY

A thesis submitted to the University of Manchester
for the degree of Doctor of Philosophy
in the Faculty of Science and Engineering

2018

Naeem Mustaq Desai
School of Mathematics

Contents

Word count 36925

List of Tables

List of Figures

The University of Manchester

Naeem Mustaq Desai
Doctor of Philosophy
Tensor Tomography
January 26, 2018

Rich tomography is becoming increasingly popular since we have seen a substantial increase in computational power and storage. Instead of measuring one scalar for each ray, multiple measurements are needed per ray for various imaging modalities. This advancement has allowed the design of experiments and equipment which facilitate a broad spectrum of applications.

We present new reconstruction results and methods for several imaging modalities including x-ray diffraction strain tomography, Photoelastic tomography and Polarimetric Neutron Magnetic Field Tomography (PNMFT). We begin with a survey of the Radon and x-ray transforms discussing several procedures for inversion. Furthermore we highlight the Singular Value Decomposition (SVD) of the Radon transform and consider some stability results for reconstruction in Sobolev spaces.

We then move onto define the Non-Abelian Ray Transform (NART), Longitudinal Ray Transform (LRT), Transverse Ray Transform (TRT) and the Truncated Transverse Ray Transform (TTRT) where we highlight some results on the complete inversion procedure, SVD and mention stability results in Sobolev spaces. Thereafter we derive some relations between these transforms. Next we discuss the imaging modalities in mind and relate the transforms to their specific inverse problems, primarily being linear. Specifically, NART arises in the formulation of PNMFT where we want to image magnetic structures within magnetic materials with the use of polarized neutrons. After some initial numerical studies we extend the known Radon inversion presented by experimentalists, reconstructing fairly weak magnetic fields, to reconstruct PNMFT data up to phase wrapping.

We can recover the strain field tomographically for a polycrystalline material using diffraction data and deduce that a certain moment of that data corresponds to the TRT. Quite naturally the whole strain tensor can be reconstructed from diffraction data measured using rotations about six axes. We develop an innovative explicit plane-by-plane filtered back-projection reconstruction algorithm for the TRT, using data from rotations about three orthogonal axes and state the reasoning why two-axis data is insufficient. For the first time we give the first published results of TRT reconstruction. To complete our discussion we present Photoelastic tomography which relates to the TTRT and implement the algorithm discussing the difficulties that arise in reconstructing data.

Ultimately we return to PNMFT highlighting the nonlinear inverse problem due to phase wrapping. We propose an iterative reconstruction algorithm, namely the Modified Newton Kantarovich method (MNK) where we keep the Jacobian (Fréchet derivative) fixed at the first step. However, this is shown to fail for large angles suggesting to develop the Newton Kantarovich (NK) method where we update the Jacobian at each step of the iteration process.

Declaration

No portion of the work referred to in the thesis has been submitted in support of an application for another degree or qualification of this or any other university or other institute of learning.

Copyright Statement

i. The author of this thesis (including any appendices and/or schedules to this thesis) owns certain copyright or related rights in it (the "Copyright") and he has given The University of Manchester certain rights to use such Copyright, including for administrative purposes.

ii. Copies of this thesis, either in full or in extracts and whether in hard or electronic copy, may be made **only** in accordance with the Copyright, Designs and Patents Act 1988 (as amended) and regulations issued under it or, where appropriate, in accordance with licensing agreements which the University has from time to time. This page must form part of any such copies made.

iii. The ownership of certain Copyright, patents, designs, trade marks and other intellectual property (the "Intellectual Property") and any reproductions of copyright works in the thesis, for example graphs and tables ("Reproductions"), which may be described in this thesis, may not be owned by the author and may be owned by third parties. Such Intellectual Property and Reproductions cannot and must not be made available for use without the prior written permission of the owner(s) of the relevant Intellectual Property and/or Reproductions.

iv. Further information on the conditions under which disclosure, publication and commercialisation of this thesis, the Copyright and any Intellectual Property and/or Reproductions described in it may take place is available in the University IP Policy (see http://documents.manchester.ac.uk/DocuInfo.aspx?DocID=24420), in any relevant Thesis restriction declarations deposited in the University Library, The University Library's regulations (see http://www.library.manchester.ac.uk/about/regulations/) and in The University's Policy on Presentation of Theses.

Acknowledgements

I would like to thank several people who have assisted me during the course of my PhD. Firstly from the bottom of my heart, I am indebted to the affection and encouragement of my supervisor, Professor Bill Lionheart. Truly for his guidance, support, patience and for always being a source of inspiration. Furthermore, many thanks to my examiners Professor Manuchehr Soleimani, Dr. Sean Holman and Dr Oliver Dorn (independent chair) for their useful comments and suggestions to improve this piece of work.

I would also like to thank the other members of the Inverse Problems group; Mike, Russell, Sophia, Henry, Francis, James, Taufiq, Ashkan, Alex and Philip. A special thanks to my Mum and Dad for their constant support throughout as well as my sister and brother. Also my wife for keeping me sane and always being there to comfort me in times of stress and worry. Lastly, I can not forget my son Ahmad, to him I dedicate this thesis.

Chapter 1

Introduction

Due to requirements from applications both in industry and various academic disciplines, the field of *inverse problems* has undergone a tremendous growth resulting in the formation of an essentially multidisciplinary scientific subject. It is not entirely clear who the founder of inverse problems is. However, the work of Georgian physicist Ambartsumian in 1929 is usually attributed to be the first of the kind wherein he solved the inverse Sturm-Liouville problem, namely the recovery of the differential operator from its eigenvalues. The paper [3] was published in the journal *Zeitschrift für Physik*. The actual term *inverse problem* has gained popularity since the middle of the 20th century. Inverse problems arise whenever one searches for causes of observed or desired effects that cannot be perceived directly, e.g. Geophysical inverse problems [34], like determining a spatially varying density distribution in the earth from gravity measurements.

We quote the statement of J.B. Keller [1], "We call two problems inverses of each other if the formulation of one problem involves the solution of the other one. Hence one is termed as the *forward* problem and the other is an *inverse* problem. Generally the forward problem involves solving some system of differential equations and usually this indicates the evolution of the described system from two attributes; knowledge of its current state and the governing physical laws including information on all physically relevant parameters. Conversely a possible inverse problem would be to estimate (some of) these parameters from observations of the evolution of the system. Sometimes this distinction is not so obvious, e.g. differentiation and integration are inverse to each other but how would we articulate this properly. According to Hadamard [14], a mathematical problem is called *well-posed* if

- for all admissible data, a solution exists,
- for all admissible data, the solution is unique and
- small perturbations in the data does not affect the solution largely.

Thus we regard integration to be well-posed and differentiation is *ill-posed*, a property common to most inverse problems. So integration is the forward problem and differentiation is the inverse problem.

Amongst the many inverse problems is x-ray Computerized Tomography (CT), which is central to the ideas developed within this thesis. Specifically tomography is when images of internal structures of a solid object such as the human body (medical x-ray) or the Earth are created. This is done by observing and recording the differences in the effects on the passage of waves of energy, impinging on specific structures. The origin of the word tomography recapitulates its usage today as the derivation stems to Ancient Greece; $\tau o \mu o \zeta$ *tomos* means slice section and $\gamma \rho \alpha \phi \omega$ *graph* means to write. The Radon transform introduced by *Johann Radon* in 1917 laid the foundation to x-ray CT but the recognition goes to Godfrey Hounsfield and Allan Cormack as they developed the first practical implementation of x-ray CT in 1972 as well as receiving the Nobel Prize in Medicine in 1979.

Over the years the field of x-ray CT has developed and evolved with applications including but not limited to nondestructive materials testing, geophysics, and archaeology. Furthermore, it became the motivation for scientists to develop other novel imaging modalities as they started to realise that x-rays whilst passing through crystals would give diffraction patterns. Another advancement was when one uses different rays from the electromagnetic spectrum, e.g. gamma rays and infra-red, or to use neutrons and electrons which exhibit wave-particle duality for imaging purposes. Indeed in 1994, the Nobel Prize in Physics was given partly to Clifford G. Shull for the development of the neutron diffraction technique. Nowadays especially for applications in material science where information related to the crystal structure (strain, phase, texture) of polycrystalline materials is sought, techniques such as Neutron Bragg Edge Tomography [48] and x-ray diffraction tomography [24] are becoming increasingly popular.

As the diversity of applications continues to preponderate with mathematics being applied to a manifold of disciplines and supercomputing is escalating, the need to design robust and revolutionary reconstruction algorithms is much more in demand than ever before. Increasingly we need to image quantities with more degrees of freedom than a simple scalar such as magnetic fields (vector) and tensor fields (strain). To do this tomographically we need richer data than one scalar per line (ray). In some types of innovative tomography we have a function for each line (ray), from varying wavelength, energy, diffraction angle etc, giving more data. The rise in computational storage ability has aided problems of this type (big data). Korsunsky [24] (perhaps others also) call this *Rich Tomography.* As new tomographic measurement modalities arise we need to understand what data is needed for a stable reconstruction and how to do that reconstruction numerically.

Such experimental techniques are not carried out in small scale laboratories within universities or research institutes. In fact throughout the last few decades and continuing to proliferate are the construction of synchroton facilities throughout the world. The demand for such sites are a source of attraction for research grants from governments and industrial sponsors. One such site is the European Spallation Source (ESS) based in Lund, Sweden, which is believed to be the worlds most powerful pulsed neutron source when the framework will be completed by 2025. The estimated cost of the facility in 2013 was 1.843 billion euros. On the occasion of ICTMS 2017, the third international conference on tomography of material and structures held in Lund, between 26th - 30th of June 2017, participants were given a guided tour of ESS and MAXIV, the new Swedish synchroton facility. Here in the United Kingdom, we have a site in Harwell, Oxfordshire, named the Diamond Light Source, adjacent to which is the Rutherford Appleton Laboratory (RAL) where we have a research group named Manchester x-ray Imaging Facility (MXIF). Moreover, the Queen's Anniversary Prize Award (2012-2014) was given for *new techniques in x-ray imaging of materials critical for power, transport and other key industries* to Prof Phil Withers, MXIF director and Regius professor of materials.

Just before the start of the new millennium it was proposed to image magnetic domains in bulk samples non-destructively with the idea to use polarized neutrons. The trend in using neutrons for tomography is that it provides important complementary information to that given by x-rays as neutrons have zero electrical charge and can penetrate deeply into massive samples, see [45]. Neutrons are highly sensitive to magnetic fields owing to their magnetic moment and thus they can be used for real space tomographic imaging investigations of magnetic structures. The first simulations were presented by [19, 25] and developed further by Kardjilov [22] to make two and three dimensional images of magnetic fields. Initially the setup did not measure the full spin rotation matrix but only a single diagonal element of it was recorded. Correspondingly, the method has been applied for strongly oriented fields and high symmetry cases providing significant *a priori* knowledge for analysis, e.g. through field modeling and simulation matching with data. In this manner magnetic fields of electromagnetic devices and electric currents, [22, 41, 44, 29, 47], but also quantum mechanical effects in superconductors [22, 44, 7] could be studied successfully.

Recently experimentalists have succeeded to ensure the measurement of these polarized neutrons, the feasibility demonstrated in [44], giving rise to a rich tomography problem as each ray of an ensemble of neutrons gives nine scalars, resulting in a 3×3 matrix. Although no official name has been assigned to the new imaging modality, pilot studies suggest giving the name Polarimetric Neutron Magnetic Field Tomography (PNMFT). Indeed the only apparatus able to acquire PNMFT data in the world as yet has been innovatively assembled at the Japan Proton Accelerator Research Complex (J-PARC) [41] in Tokai, Japan. Interestingly, we have devised an inventive reconstruction algorithm for the reconstruction of weak magnetic fields. Furthermore for the first time we show reconstructions of simulated PNMFT data in this thesis which has motivated physicists and experimentalists to reconstruct experimental data. Moreover for stronger magnetic fields we have pioneered a method which is capable to reconstruct magnetic fields where phase wrapping issues arise since a well known phenomenon is that neutrons revolve around their axis when coming into contact with a magnetic field.

The diffraction pattern of an x-ray (or neutrons) through polycrystalline solids such as metals has been used extensively to study the crystal structure and atomic spacing. Only very recently though have scientists realised that it can be possible to use this technique to image and visualise strain patterns in a polycrystalline material. Nevertheless strain is a symmetric rank two tensor which means that the diffraction pattern gives rise to more information than just a scalar per ray, an example of rich tomography. Several research groups have devised a reconstruction technique to image strain but have not realised that they are actually calculating the overall change in thickness of the sample along the ray. An alternative viewpoint proposed two years ago by Lionheart and Withers in [27] is to use a certain moment of the diffraction pattern which relates to the Transverse Ray Transform (TRT). To acquire measurement data for such a modality would require a laborious scan, one which would necessitate revolving the sample around six axes. Experimentalists would adore an innovation where less time and effort is required to gather data. Indeed work in this thesis outlines such a reconstruction algorithm which would half the amount of data to store as well as halving the time spent in collecting data. A new three axes explicit plane-by-plane reconstruction procedure is derived and first time numerics on simulated data are shown suggesting the technique can be used on experimental data. Such an experimental setup would need to be set up at a synchroton facility.

Numerous situations in mechanical engineering involve prediction of the stress behaviour in solid components under load. Nondestructive methods to measure stresses in three-dimensional photoelastic models of engineering components are currently of great interest to the aerospace and automotive industries. Only recently a new instrument has been developed in conjunction with Rachel Tomlinson, University of Sheffield, allowing experimental verification of the design for prototypes to be performed quickly and efficiently. As yet no reconstruction of raw experimental data has been successful, even for weak stress. We outline the causes and theoretical reasoning why the case may be so and suggest another technique which may give a breakthrough. Indeed the author has made contributions to the reconstruction code running on the machines in the PSI [1] (previously) and now the University of Sheffield, recognising the bugs and fixing these.

Now we give a brief outline of each chapter of this thesis, drawing attention to the main results. In Chapter 2 we introduce the Radon and x-ray transforms and consider the inversion procedures. Specifically for the two dimensional case (one slice) numerical results for several reconstruction procedures are shown. Moreover we display a slice by slice approach to reconstruct a three dimensional phantom before stating

---

[1] Photon Science Institute, University of Manchester

the singular value decomposition for the Radon transform. For completeness we state some stability results. In Chapter 3 several ray transforms are introduced and their inversion formulae are derived for complete data before stating results which relate some of these transforms.

In Chapter 4 we explain three different imaging modalities and mention which ray transforms are associated with them. For the linear inverse problem of PNMFT numerics are shown. In Chapter 5 we derive explicit plane-by-plane reconstruction formulae for symmetric rank two tensor fields and display the numerics for the first time. In Chapter 6 we introduce the nonlinear inverse problem of PNMFT. The drawback of using the Modified Newton Kantarovich (MNK) method is illustrated whilst a possible way to resolve this is suggested, the Newton Kantarovich (NK) method.

Throughout the period of study for this PhD, three journal articles have been produced. One has been published [10], another undergoing corrections [37] and the third [11] on the verge of submission. These are

1. An explicit reconstruction algorithm for the transverse ray transform of a second rank tensor field from three axis data - Naeem M. Desai and William R.B. Lionheart.
2. Three Dimensional Polarimetric Neutron Tomography of Magnetic Fields - Morten Sales et al.
3. Polarimetric Neutron Magnetic Field Tomography : a non-Abelian ray transform - Naeem Desai et al.

Specifically in [10], the author developed the explicit reconstruction algorithm in collaboration with Bill Lionheart and numerically implemented it. Likewise in [37], the author formulated the PNMFT problem as a non-abelian ray transform type problem. Finally, for [11], the author developed the forward solver whilst numerically implementing the reconstruction of simulated data by the use of MNK. Moreover an improved method, precisely, NK was suggested.

Chapter 2

The Radon Transform

To develop the necessary machinery to aid us throughout this thesis, this chapter outlines some of the fundamental results within the literature. We start off in Section 2.1 with the notion of a distribution in order to define the Fourier transform on the correct spaces. Thereafter the Radon and x-ray transforms are introduced with some inversion results. In Section 2.2 we discuss how to discretize the Radon operator and its adjoint in a two dimensional setting. Numerical implementations of filters are described in Section 2.3.1 and the CGLS algorithm is introduced in 2.3.2. It is well known that a volumetric reconstruction is possible by a slice by slice approach. An example of this is introduced in Section 2.3.3 using a Hilbert transform reconstruction approach. In Section 2.4 the range of the Radon transform is discussed with its ill-posedness property. Finally to complete, some stability estimates are mentioned in Section 2.5.

2.1 Distribution Theory

A distribution is a kind of generalised[1] function. Every reasonable function corresponds to a distribution, however the converse is not necessarily true. The theory of distributions has a coherence and power that the classical theory of functions lacks, e.g. the derivative of a distribution always exists and is another distribution. By contrast, there are many continuous functions which have no derivatives in the classical sense, e.g. Weierstrass function. Hence for our purpose it suffices to study the Fourier

---

[1] classical sense

transform in a distribution sense.

To show the nature of the difficulties for the Fourier transform in the classical sense, we shall glance briefly on the definition of the Fourier transform based on $L^1(\mathbb{R})$ (integrable) functions. Since the definition involves an integral, $\hat{f}(\xi) = \int_{-\infty}^{\infty} e^{-\mathrm{i}x\cdot\xi} f(x)\, dx$, it is quite natural to require that this integral converges which demands the integrability of the function $f(x)$. However the Fourier transform $\hat{f}(\xi)$ is not necessarily integrable making the Fourier inversion theorem meaningless. With the theory of tempered distributions, all of these difficulties disappear. We will study the Fourier transform in the Schwartz space $\mathcal{S}(\mathbb{R}^n)$ and in it's dual $\mathcal{S}'(\mathbb{R}^n)$ but before we define the Fourier transform properly, several definitions are given.

A *test function*, ϕ, is a C^∞ function with compact support which means it has continuous derivatives of all orders and it vanishes outside some bounded set. In $\mathbb{R}$ there is only one derivative operator $\frac{\mathrm{d}}{\mathrm{d}x}$ and the most general higher order derivative is simply $\frac{\mathrm{d}^n}{\mathrm{d}x^n}$. However when working in $\mathbb{R}^q$, where $q \neq 1$, there are q first order derivatives $\frac{\partial}{\partial x_i}$, $1 \leq i \leq q$. Hence rather cumbersome higher order expressions arise, like

$$\frac{\partial^{\alpha_1+\alpha_2+...+\alpha_q}}{\partial x_1^{\alpha_1}\partial x_2^{\alpha_2}....\partial x_q^{\alpha_q}}. \tag{2.1}$$

We require an abbreviated form of the differential operator mentioned in (2.1) which leads us quite naturally to define the notion of **multi-indices** helping us to define an open support test function.

Definition 2.1 *Let us define a q-tuple of non-negative integers,* $\alpha = (\alpha_1, ..., \alpha_q)$ *and let* $|\alpha| = \alpha_1 + \alpha_2 + ... + \alpha_q$. *Then the differential operator in (2.1) can be written as* $\mathcal{D}^\alpha = \frac{\partial^{|\alpha|}}{\partial x^\alpha}$. *Such a q-tuple is defined as a multi-index.*

Definition 2.2 *A function* $\phi \in C^\infty(\mathbb{R}^n)$ *is called an* ***open support test function*** *if for every* $n, k \in \mathbb{N}$, $x^n\phi^{(k)}(x)$ *remains bounded as* $x \to \pm\infty$. *The space of open support test functions on* $\mathbb{R}^n$ *is denoted by* $\mathcal{S}(\mathbb{R}^n)$ *and is known as the* ***Schwartz*** *space.*

Before we state the definition of a *distribution* the description of an inner product space is given below.

Definition 2.3 *An* ***inner product*** *space is a linear function space, on which there is defined an inner (scalar) product* $\langle f, g\rangle \in \mathbb{R}$ *(or* $\mathbb{C}$*) such that*

- $\langle g, f\rangle = \langle f, g\rangle -$ *real,*
  (or $\langle g, f\rangle = \overline{\langle f, g\rangle} -$ *complex - bar denotes complex conjugate),*
- $\langle g, \alpha f_1 + \beta f_2\rangle = \alpha\langle g, f_1\rangle + \beta\langle g, f_2\rangle$,
- $\langle f, f\rangle \geq 0$ *with equality* $\Leftrightarrow f = 0$.

Definition 2.4 *A* ***tempered distribution*** T *is a mapping from the set of open support test functions* $\mathcal{S}(\mathbb{R}^n)$ *into the complex numbers* $(\mathbb{C})$ *which satisfies the following*

- ***(Linearity)*** $\langle T, a\phi(x) + b\psi(x)\rangle = a\cdot\langle T, \phi(x)\rangle + b\cdot\langle T, \psi(x)\rangle,\ \forall\phi, \psi \in \mathcal{S}(\mathbb{R}^n)$ *and* $a, b \in \mathbb{C}$.
- ***(Continuity)*** *If* $\phi_n \to 0$ *in* $\mathcal{S}(\mathbb{R}^n)$, *then* $\langle T, \phi_n\rangle \to 0$.

A remark on the *inner product* notation $\langle T_f, \phi\rangle = \int_{-\infty}^{\infty} f(x)\phi(x)\ dx$, where T_f is the distribution corresponding to f. This reminds us of the underlying idea that the transition from functions to distributions is given by an integral. The set of all tempered distributions is denoted by $\mathcal{S}'(\mathbb{R}^n)$ and is defined by the (continuous) dual of the Schwartz space, $\mathcal{S}$.

For a function $\phi \in \mathcal{S}(\mathbb{R}^n)$ we denote the Fourier transform $\hat{\phi}$ and its inverse $\check{\phi}$ using the following

$$\hat{\phi}(y) = (2\pi)^{-\frac{n}{2}} \int_{\mathbb{R}^n} e^{-\mathrm{i}x\cdot y}\phi(x)\ dx. \tag{2.2}$$

$$\check{\phi}(x) = (2\pi)^{-\frac{n}{2}} \int_{\mathbb{R}^n} e^{\mathrm{i}x\cdot y}\phi(y)\ dy. \tag{2.3}$$

Often a need arises to use the partial Fourier transform where we consider a k-dimensional vector subspace $V \subset \mathbb{R}^n$ with Cartesian coordinates $(x_1, x_2, ..., x_n)$ in $\mathbb{R}^n$ such that $V = \{x\ |x_{k+1} = ... = x_n = 0\}$. The partial Fourier transform can then be written as

$$\hat{\phi}(y_1, ..., y_k, x_{k+1}, ..., x_k) = (2\pi)^{-\frac{k}{2}} \int_{\mathbb{R}^k} e^{-\mathrm{i}(y_1x_1+....y_kx_k)}\phi(x)\ dx_1....dx_k. \tag{2.4}$$

If any introduction to distribution theory is consulted, like [35], it can be seen that if $\phi \in \mathcal{S}(\mathbb{R}^n)$, then so are $\hat{\phi}, \check{\phi} \in \mathcal{S}(\mathbb{R}^n)$. Above in (2.2) and (2.3) we have defined the Fourier transform. However, in reality we require the definition of the Fourier transform for distributions which is given below.

Definition 2.5 *Let $T \in \mathcal{S}'(\mathbb{R}^n)$. The Fourier transform of T is the map $\hat{T} : \mathcal{S}(\mathbb{R}^n) \to \mathbb{C}$ defined by*

$$\hat{T}\phi := T\hat{\phi}, \quad \forall \phi \in \mathcal{S}(\mathbb{R}^n). \tag{2.5}$$

Now for example, consider $f \in L^1(\mathbb{R}^n)$ and let T_f be the distribution defined by $T_f\phi = \int_{\mathbb{R}^n} f(x)\phi(x)\ \mathrm{d}x$ for all $\phi \in \mathcal{S}(\mathbb{R}^n)$. Then by Definition 2.5 we have

$$\widehat{T_f}\phi = \int_{\mathbb{R}^n} f(x)\ \hat{\phi}(x)\ \mathrm{d}x = \int_{\mathbb{R}^n} \left(\int_{\mathbb{R}^n} e^{-\mathrm{i}y\cdot x} f(x)\ dx \right)\ \phi(y)\ \mathrm{d}y = T_{\hat{f}}\phi.$$

In other words, when you Fourier transform the distribution associated to f, you get the distribution associated to $\hat{f}$, the ordinary Fourier transform of f.

Now that the Fourier transform has been defined properly in a distribution sense the Radon and x-ray transforms which are fundamental tools to several ideas developed within this thesis have to be clearly specified. The (n-dimensional) Radon transform R maps a function on $\mathbb{R}^n$ into the set of its integrals over hyperplanes of $\mathbb{R}^n$. Consider $\xi \in \mathbb{S}^{n-1}$ and $p \in \mathbb{R}$ then we have

$$R : \mathcal{S}(\mathbb{R}^n) \to \mathcal{S}(Z), \quad \text{with } Z = \mathbb{S}^{n-1} \times \mathbb{R}.$$

The Radon transform can be defined as follows

$$Rf(\xi, p) = \int_{x\cdot\xi=p} f(x)\ dx = \int_{\xi^{\perp}} f(p\xi + y)\ dy, \tag{2.6}$$

which is the integral of $f \in \mathcal{S}(\mathbb{R}^n)$ over the hyperplane perpendicular to ξ with (signed) distance p from the origin (when $n = 2$, see Figure 2.1).

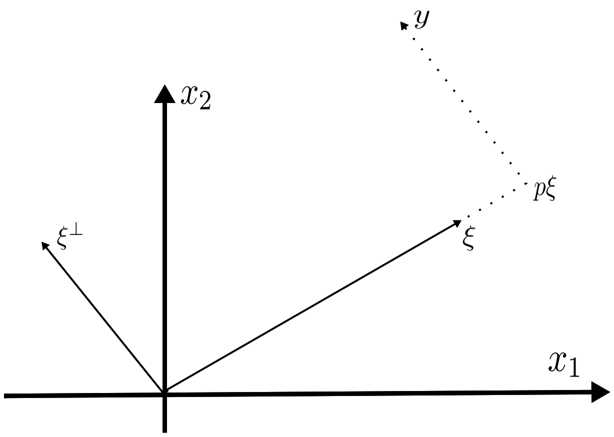

Figure 2.1: Parameterisation of a line.

The (n-dimensional) x-ray transform X maps a function on $\mathbb{R}^n$ into the set of its line integrals. Consider $\xi \in \mathbb{S}^{n-1}, x \in \mathbb{R}^n$ and $t \in \mathbb{R}$, then

$$Xf(\xi, x) = \int_{-\infty}^{\infty} f(x + t\xi)\ dt \tag{2.7}$$

is the integral of $f \in \mathcal{S}(\mathbb{R}^n)$ over the straight line through x with direction ξ. Note that if x is moved in the direction of ξ then $Xf(\xi, x)$ does not change, hence we restrict x to $\xi^{\perp}$. The x-ray transform is an integral operator which can be realised as follows

$$X : \mathcal{S}(\mathbb{R}^n) \to \mathcal{S}(T\mathbb{S}^{n-1}), \text{ where}$$

$$T\mathbb{S}^{n-1} = \{(\xi, x) \in \mathbb{R}^n \times \mathbb{R}^n \mid |\xi| = 1, \xi \cdot x = 0\} \subset \mathbb{R}^n \times \mathbb{R}^n \tag{2.8}$$

is the tangent bundle of the unit sphere $\mathbb{S}^{n-1}$. For $n = 2$, topologically one can understand this by considering all the tangent space to a circle, $\mathbb{S}^1$, joining these tangents in a smooth and non overlapping manner described in Figure 2.2.

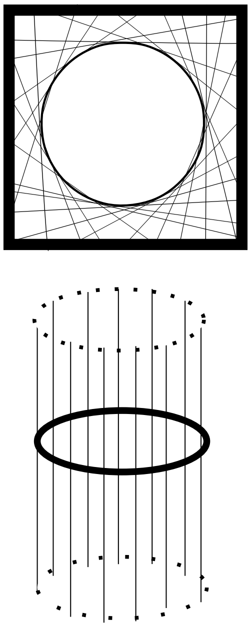

Figure 2.2: Tangent bundle of the unit sphere, $T\mathbb{S}^1$.

Before we state further results, let us take a look at Radon data for the case $n = 2$ which is often referred to as a *sinogram*. The Radon transform of a Dirac delta function is a distribution supported on the graph of a sine wave. Hence let us consider $f(x)$ to be zero except for a delta measure centred on the point $x = (x_1, x_2)^T \in \mathbb{R}^2$. Any line that misses the delta measure gives us an integral of zero. However those that hit the delta measure give a positive value. We know that for each angle, ξ, the lines will hit the delta measure. Hence from definition

$$x \cdot \xi = x_1 \cos\phi + x_2 \sin\phi = p,$$

since we just need the p for each ξ. Now if we plot the (ξ, p) pairs, which give lines through x we yield a cosine curve. This is because we can also write p in terms of polar coordinates, α and $\sqrt{x_1^2 + x_2^2}$. Hence

$$p = \sqrt{x_1^2 + x_2^2}\cos(\phi + \alpha).$$

The amplitude and phase of the cosine curve indicate the position of the object. Thus by superposition, several distinct objects produce several sine waves. Hence the name sinogram. Trivially it can be shown that $Rf(\xi, p) = Rf(-\xi, -p)$ which means that Rf is an even function and topologically the range of the Radon transform, $\mathbb{S}^1 \times \mathbb{R}$ is an infinite cylinder. One interesting fact is the range of the x-ray transform $(n = 2)$ is $T\mathbb{S}^1$, tangent bundle to the unit sphere, which is diffeomorphic to $\mathbb{S}^1 \times \mathbb{R}$, suggesting a link between $Rf(\xi, p)$ and $Xf(\xi, x)$ in two dimensions. Of course $Xf(\xi, x)$ and $Rf(\omega, p)$ where $\xi \perp \omega$ coincide (except for the notation of arguments) since

$$Rf(\omega, p) = \int_{x \in \xi^\perp, x \cdot \omega = p} Xf(\xi, x)\ dx. \tag{2.9}$$

The above arguments show in the two dimensional case what Radon (x-ray) data looks like. Regardless of this insight into the range, how would one characterise the range of (2.6) and (2.7) in arbitrary dimension n? The answer to this lies in [31, Theorem 4.1].

Theorem 2.1 *Let $f \in \mathcal{S}(\mathbb{R}^n)$. Then, for $m = 0, 1, ...$*

$$\int_{\mathbb{R}} s^m Rf(\xi, s)\ ds = p_m(\xi), \tag{2.10}$$

$$\int_{\xi^\perp} (x \cdot v)^m Xf(\xi, x)\ dx = q_m(v), \quad v \perp \xi, \tag{2.11}$$

with p_m, q_m homogeneous polynomials of degree m, q_m being independent of ξ.

Proof We compute

$$\int_{\mathbb{R}} p^m Rf(\xi, p)\ dp = \int_{\mathbb{R}} p^m \int_{\xi^\perp} f(p\xi + y)\ dy\ dp = \int_{\mathbb{R}^n} (x \cdot \xi)^m f(x)\ dx,$$

where we have used the substitution $x = p\xi + y$ and indeed this is a homogeneous polynomial of degree m in ξ. Similarly,

$$\int_{\xi^\perp} (x \cdot v)^m Xf(\xi, x)\; dx = \int_{\xi^\perp} (x \cdot v)^m \int_{\mathbb{R}} f(x + t\xi)\; dt\; dx = \int_{\mathbb{R}^n} (u \cdot v)^m f(u)\; dz,$$

for $v \perp \xi$ where we have put $u = x + t\xi$. This is a homogeneous polynomial of degree m in v being independent of ξ. $\square$

Prior to the explanation of why Theorem 2.1 was stated, we define **special functions** which arise mainly as the eigenfunctions of self-adjoint[2] ordinary differential equations. These are orthogonal bases for weighted L^2 spaces on intervals and are often associated with 19th century European mathematicians.

Definition 2.6 *The* ***Gegenbauer*** *polynomials* $C_l^\lambda, \lambda > -\frac{1}{2}$, *of degree* l *are defined as the orthogonal polynomials on* $[-1, +1]$ *with weight function* $(1-x^2)^{\lambda-\frac{1}{2}}$. *We normalize* C_l^λ *by requiring* $C_l^\lambda(1) = 1$. *We then have*

$$\int_{-1}^{+1} (1 - x^2)^{\lambda-\frac{1}{2}} C_l^\lambda(x) C_k^\lambda(x)\; dx = \begin{cases} 0, & l \neq k \\ \frac{2^{2\lambda-1}(\Gamma(\lambda+\frac{1}{2}))^2 l!}{(1+\lambda)\Gamma(l+2\lambda)}, & l = k \end{cases} \tag{2.12}$$

where Γ *is the Gamma function.*

For $\lambda = 0$, these can be recognised as the *Chebyshev* polynomials of the first kind, $T_l = C_l^0$ which are given by the formula $T_l(x) = \cos(l \arccos(x))$. In other words, $T_l(x)$ is a polynomial that expresses $\cos(l\theta)$ in terms of $\cos(\theta)$, e.g. $T_3(x) = \cos(3\theta) = 4\cos^3(\theta) - 3\cos(\theta) = 4x^3 - 3x$. Moreover Chebyshev polynomials of the second kind when $\lambda = 1$ are defined by

$$U_l(x) = (l + 1)C_l^1 = \frac{\sin((l + 1) \arccos(x))}{\sin(\arccos(x))}. \tag{2.13}$$

Definition 2.7 *A spherical harmonic* Y_l *of degree* l *is the restriction to* $\mathbb{S}^{n-1}$ *of a harmonic polynomial homogeneous of degree* l *on* $\mathbb{R}^n$. *There are*

$$N(n, l) = \frac{(2l + n - 2)(n + l - 3)!}{l!(n - 2)!},\; N(n, 0) = 1$$

linearly independent spherical harmonics of degree l, *and spherical harmonics of different degree are orthogonal on* $\mathbb{S}^{n-1}$.

---

[2] defined later in Section 2.3

The motivation in stating (2.10) of Theorem 2.1 is if $f \in C_0^\infty$, where f is continuously many times differentiable (smooth) and is compactly supported on the unit disk, then the expansion of $Rf(\xi, p)$ can be written in terms of the products $C_l^\lambda Y_{kj}$, where C_l^λ are the Gegenbauer polynomials and Y_{kj} the spherical harmonics. This will have consequences which we shall use later in Section 2.4. Note that these functions form a complete orthogonal system in $L^2(Z, (1-p^2)^{\lambda-\frac{1}{2}})$. Hence the expansion reads

$$Rf(\xi, p) = (1-p^2)^{\lambda-\frac{1}{2}} \sum_{l=0}^{\infty} \sum_{k=0}^{\infty} \sum_{j} c_{lkj} C_l^\lambda(p) Y_{kj}(\xi)$$

where j runs over all $N(n,k)$ spherical harmonics of degree k. The C_l^λ are orthogonal in $[-1,+1]$ with respect to the weight function $(1-p^2)^{\lambda-\frac{1}{2}}$, hence

$$\int_{-1}^{+1} C_l^\lambda(p) Rf(\xi, p)\, dp = \sum_{k=0} \sum_{j} c_{lkj} \int_{-1}^{+1} (1-p^2)^{\lambda-\frac{1}{2}} (C_l^\lambda(p))^2\, dp\; Y_{kj}(\xi).$$

In accordance to (2.10), the left hand side of the above is a polynomial of degree l in ξ which due to the evenness of Rf, is even for l even and odd, for l odd. Hence $c_{lkj} \neq 0$ only for $k = l, l-2, ...$, and $Rf(\xi, p)$ assumes the form

$$Rf(\xi, p) = (1-p^2)^{\lambda-\frac{1}{2}} \sum_{l=0}^{\infty} C_l^\lambda(p) h_l(\xi) \tag{2.14}$$

where h_l is a linear combination of spherical harmonics of degree $l, l-2, ...$ In the literature (2.10) and (2.11) are known as the **Helgason-Ludwig** consistency conditions.

2.2 Ray Tracing Algorithm

In the literature the Shepp-Logan phantom is used as an image $f \in \mathcal{S}(\mathbb{R}^2)$ to simulate a sinogram. Several procedures are known to computationally implement this including the usage of the Image Processing Toolbox in MATLAB which has built in functions. However, we will simulate a sinogram by discretizing the Radon (x-ray) transform as a sparse matrix which acts on the image (e.g. the Shepp-Logan phantom) to resemble the slice of a 3D volume for CT data. The methodology adopted is to solve several line integrals for different $\xi \in \mathbb{S}^1$ which emulates x-rays fired from sources traversing a voxel grid through to detectors. In order to do this effectively, a parallel beam geometry is setup with sources and detectors lying on a circle, a certain distance from the Shepp-Logan phantom. The machinery involved to calculate a line integral relies on knowing the intersection length that a given ray makes with an indexed voxel, which is multiplied by the value of the phantom in that specific voxel. All such intersections the ray makes throughout the discretized grid are added up to give the contribution to the sinogram. This rather complex process requires the attention of [20], a revised form of [42] which is followed to explain what is known as **forward projection**.

This specific method recognises the voxels as volumes separated by the intersection of planes and calculates the intersection of a ray with those planes. The two dimensional (pixel) setting is described underneath and is easily extendable to a three dimensional setting (voxels). Suppose we parameterize a ray and consider the difference in the parameter value between consecutive lines of a given orientation defining the pixels. Let us define a pixel grid of N_x lines in the x-direction and N_y lines in the y-direction with d_x and d_y denoting the spacing between the lines. The first lines intersect at the point (b_x, b_y). The setup described above is encapsulated in Figure 2.3. The ray enters at (x_1, y_1) and leaves at (x_2, y_2) with the following parametric form

$$x(\alpha) = x_1 + \alpha(x_2 - x_1), \tag{2.15}$$

$$y(\alpha) = y_1 + \alpha(y_2 - y_1). \tag{2.16}$$

With the assumption that the ray is in a generic position (i.e. $x_1 \neq x_2$ and $y_1 \neq y_2$), the intersection points of the ray with the side of the grid are labelled $\alpha_{\min}$ and $\alpha_{\max}$. There are four situations to cover but here we will only consider the case when the ray starts and ends outside the grid. For rays that start or end inside the grid, we set $\alpha_{\min}$ or $\alpha_{\max}$ to 0 or 1 respectively.

Using the definition of α it is possible to calculate its value at the intersection of the ray with a certain line. If the line is parallel to the x-axis, set $\alpha = \alpha_x(i)$, otherwise set it to $\alpha = \alpha_y(j)$, where the line is parallel to the y-axis. These specific values are defined below

$$\alpha_x(i) = \frac{(b_x + id_x) - x_1}{x_2 - x_1}, \quad \text{and} \tag{2.17}$$

$$\alpha_y(j) = \frac{(b_y + jd_y) - y_1}{y_2 - y_1}. \tag{2.18}$$

To calculate the value of $\alpha_{\min}$ and $\alpha_{\max}$, consider

$$\alpha_{\min} = \max(0, \alpha_{x\min}, \alpha_{y\min}), \quad \text{and} \tag{2.19}$$

$$\alpha_{\max} = \min(1, \alpha_{x\max}, \alpha_{y\max}), \tag{2.20}$$

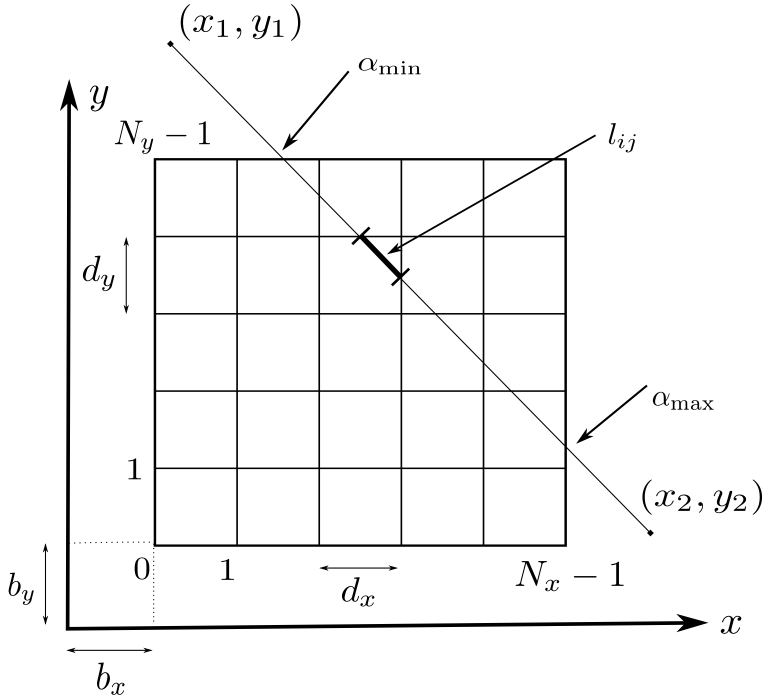

Figure 2.3: Procedure to calculate a line integral.

where

$$\alpha_{x\min} = \min(\alpha_x(1), \alpha_x(N_x)), \tag{2.21}$$

$$\alpha_{x\max} = \max(\alpha_x(1), \alpha_x(N_x)), \tag{2.22}$$

$$\alpha_{y\min} = \min(\alpha_y(1), \alpha_y(N_y)), \tag{2.23}$$

$$\alpha_{y\max} = \max(\alpha_y(1), \alpha_y(N_y)). \tag{2.24}$$

Now that $\alpha_{\min}$ and $\alpha_{\max}$ are known we can proceed to determine where the ray enters the pixel grid. The increment in α between lines in both x and y directions is also deduced. Eventually as we step through the pixel grid, we note which axis the next boundary is parallel to and update the value accordingly. For a detailed explanation, see [20]. Specifically the path length of a given ray through a certain pixel (i, j), denoted as l_{ij}, is stored as the difference between consecutive values of α. This process terminates when $\alpha > \alpha_{\max}$.

The above outlines how the intersection lengths of a given ray crossing a pixel grid are calculated. However to compute the integral we require the values of the given function specified on the pixel grid also. Thus the integral $\int_{\text{ray}} f = \sum l_{ij} f(i, j)$ which results in a very sparse matrix. Moreover this is just for a single ray, in a practical setting we usually have $\omega \times \theta$ rays where ω is the number of rays and θ is the number of

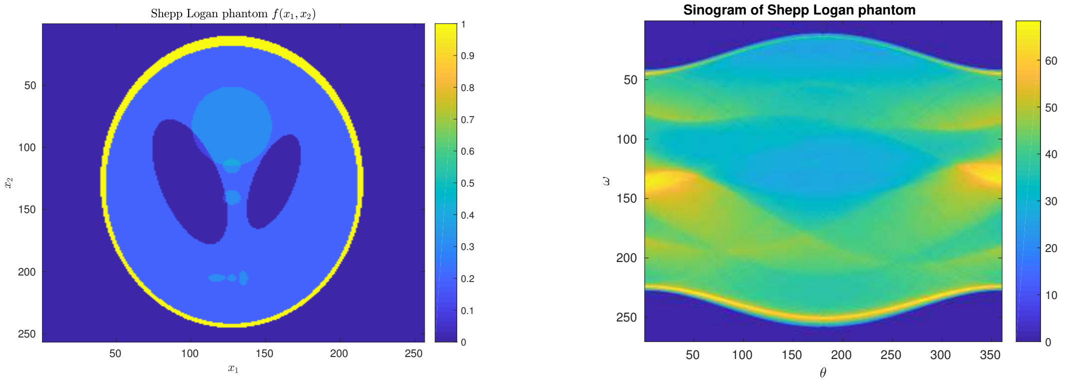

(a) Shepp Logan phantom.

(b) Sinogram data.

Figure 2.4: Forward projection illustration.

projections (views). Let A be an $(\omega \times \theta) \times (M \times N)$ matrix where $M \times N$ denotes the pixel grid size. The sinogram data is then simulated by $Af = d$, where f is a vector of length $M \times N$ whose entries consists of the value at each pixel and d is a vector of length $\omega \times \theta$. For efficient computation this process is done *on the fly* without storing the entire matrix. Figures 2.4a and 2.4b show a Shepp Logan phantom test image and the sinogram data generated by forward projection.

2.3 Reconstruction

Let us return to the general (n-dimensional) case by completing the definition of an *inner product*, Definition 2.3, which should ideally be defined via an integral. Hence the spaces $\mathcal{S}(\mathbb{R}^n), \mathcal{S}(Z)$ and $\mathcal{S}(T\mathbb{S}^{n-1})$ are equipped with the following inner products

$$\langle f_1, f_2 \rangle_{\mathcal{S}(\mathbb{R}^n)} = \int_{\mathbb{R}^n} f_1(x)\overline{f_2(x)}\, dx, \tag{2.25}$$

$$\langle g_1, g_2 \rangle_{\mathcal{S}(Z)} = \int_{\mathbb{S}^{n-1}} \int_{\mathbb{R}} g_1(\xi, p)\overline{g_2(\xi, p)}\, dp\, d\xi, \tag{2.26}$$

$$\langle h_1, h_2 \rangle_{\mathcal{S}(T\mathbb{S}^{n-1})} = \int_{\mathbb{S}^{n-1}} \int_{\xi^\perp} h_1(\xi, x)\overline{h_2(\xi, x)}\, dx\, d\xi. \tag{2.27}$$

The benefit of studying integral operators is due to their practical usage in the reconstruction of functions, e.g. Radon in medical CT. How is it possible to recover $f \in \mathcal{S}(\mathbb{R}^n)$, for some $h(\xi, x) \in \mathcal{S}(T\mathbb{S}^{n-1})$ or $g(\xi, p) \in \mathcal{S}(Z)$? This question motivates the following definition.

Definition 2.8 *Let S, T be inner product spaces, $\langle\rangle_S$, $\langle\rangle_T$ be the inner products on S, T respectively, and let $\mathcal{L} : S \to T$ be a linear operator. Then the* ***adjoint*** $\mathcal{L}^* : T \to S$ *of*

$\mathcal{L}$ is defined by

$$\langle g, \mathcal{L}f\rangle_T = \langle \mathcal{L}^* g, f\rangle_S,$$

$\forall f \in S$ and $\forall g \in T$.

Using the inner products defined in (2.25), (2.26) and (2.27), let us observe omitting the complex conjugation due to the usage of real valued function only that

$$\langle Rf(\xi,p), g(\xi,p)\rangle_{\mathcal{S}(Z)} = \int_{\mathbb{S}^{n-1}} \int_{\mathbb{R}} Rf(\xi,p) g(\xi,p)\ dp\ d\xi$$

$$= \int_{\mathbb{S}^{n-1}} \int_{\mathbb{R}} \int_{\xi^\perp} f(p\xi + y) g(\xi,p)\ dy\ dp\ d\xi.$$

Substituting a new variable of integration $x = p\xi + y$, we have $p = \xi \cdot x, dx = dy\ dp$, hence

$$\langle Rf(\xi,p), g(\xi,p)\rangle_{\mathcal{S}(Z)} = \int_{\mathbb{S}^{n-1}} \int_{\mathbb{R}^n} f(x) g(\xi, \xi\cdot x)\ dx\ d\xi = \int_{\mathbb{R}^n} f(x) \int_{\mathbb{S}^{n-1}} g(\xi,\xi\cdot x)\ d\xi\ dx,$$

by Fubini's theorem, see Appendix A.3. Thus $\langle Rf(\xi,p), g(\xi,p)\rangle_{\mathcal{S}(Z)} = \langle f(x), R^\sharp g(x)\rangle_{\mathcal{S}(\mathbb{R}^n)}$, where

$$R^\sharp g(x) = \int_{\mathbb{S}^{n-1}} g(\xi, \xi\cdot x)\ d\xi. \tag{2.28}$$

This is a *formal* adjoint and since $Rf(\xi,p)$ and $R^* g(x)$ form a dual pair in a geometric sense, it is often called the dual of the Radon transform, denoted as $R^\sharp g(x)$. Intuitively, it can be seen that the Radon transform integrates over all points on a given hyperplane, whilst the dual of the Radon transform integrates over all hyperplanes through a point which is why it is understood to be known as **backprojection** as it "projects back" the Radon data along the hyperplanes onto the image. Similarly for the x-ray transform, a formal adjoint can be derived as

$$\langle Xf(\xi,x), h(\xi,x)\rangle_{\mathcal{S}(T\mathbb{S}^{n-1})} = \int_{\mathbb{S}^{n-1}} \int_{\xi^\perp} Xf(\xi,x) h(\xi,x)\ dx\ d\xi$$

$$= \int_{\mathbb{S}^{n-1}} \int_{\xi^\perp} \int_{\mathbb{R}^1} f(x + t\xi) h(\xi,x)\ dt\ dx\ d\xi.$$

Natterer [31] shows this is $\langle Xf(\xi,x), h(\xi,x)\rangle_{\mathcal{S}(T\mathbb{S}^{n-1})} = \langle f(x), X^\sharp h(x)\rangle_{\mathcal{S}(\mathbb{R}^n)}$, where

$$X^\sharp g(x) = \int_{\mathbb{S}^{n-1}} h(\xi, \Pi_{\xi^\perp} x)\ d\xi. \tag{2.29}$$

The $\Pi_{\xi^\perp}$ indicates an orthogonal projection on $\xi^\perp$ defined properly in Section 3.2.2.

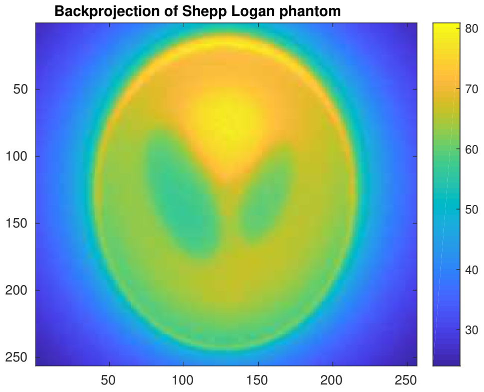

Figure 2.5: Backprojection of Radon data.

To implement backprojection numerically we reuse the same code in Section 2.2. In a discrete setting ray integration is a matrix, say A. Since we require the dual operator, then A^T is backprojection. If this process is used, it is termed as a matched backprojector considering there are other backprojection methods available.

From Figure 2.5, the issue of simply using backprojection for the reconstruction of functions has been illustrated, consequently requiring the derivation of a better reconstruction algorithm. Indeed, several reconstruction algorithms exist, some of which shall be exemplified in due course. To facilitate the derivation of such results we state the **Fourier slice theorem**. Note that we can write $Rf(\xi, p) = R_\xi f(p)$ and $Xf(\xi, x) = X_\xi f(x)$ which is also called the *projection* of f onto $\xi^\perp$.

Theorem 2.2 *Let $f \in \mathcal{S}(\mathbb{R}^n)$, then*

$$\widehat{R_\xi f}(\sigma) = (2\pi)^{\frac{n-1}{2}} \hat{f}(\sigma\xi), \quad \sigma \in \mathbb{R} \tag{2.30}$$

$$\widehat{X_\xi f}(\tau) = \sqrt{2\pi} \hat{f}(\tau), \quad \tau \in \xi^\perp \tag{2.31}$$

Proof By definition of the one dimensional Fourier transform ($k = 1$) from (2.4), we have

$$\widehat{R_\xi f}(\sigma) = \frac{1}{\sqrt{2\pi}} \int_{\mathbb{R}} e^{-\mathrm{i}\sigma p} R_\xi f(p)\; ds = \frac{1}{\sqrt{2\pi}} \int_{\mathbb{R}} e^{-\mathrm{i}\sigma p} \int_{\xi^\perp} f(p\xi + y)\; dy\; dp.$$

Suppose $x = p\xi + y$, then $p = \xi \cdot x,\; dx = dy\; dp$, so

$$\widehat{R_\xi f}(\sigma) = \frac{1}{\sqrt{2\pi}} \int_{\mathbb{R}^n} e^{-\mathrm{i}\sigma\xi\cdot x} f(x)\; dx = (2\pi)^{\frac{n-1}{2}} \hat{f}(\sigma\xi).$$

Equivalently,

$$\widehat{X_\xi f}(\tau) = (2\pi)^{-\frac{n-1}{2}} \int_{\xi^\perp} e^{-\mathrm{i}\tau\cdot y} X_\xi f(y)\, dy = (2\pi)^{-\frac{n-1}{2}} \int_{\xi^\perp} e^{-\mathrm{i}\tau\cdot y} \int_{\mathbb{R}} f(y+t\xi)\, dt\, dy$$

$$= (2\pi)^{-\frac{n-1}{2}} \int_{\mathbb{R}^n} e^{-\mathrm{i}\tau\cdot x} f(x) dx = \sqrt{2\pi}\hat{f}(\tau),$$

by the Fourier transform definition and the change of variables mentioned above. □

2.3.1 Filtered Backprojection

Here we derive inversion formulas for the Radon and x-ray transforms.

Definition 2.9 *Let $f \in Z$. The **Riesz potential** $\mathbb{I}^\alpha$ of a function is given by*

$$\widehat{\mathbb{I}^\alpha f}(\rho) = |\rho|^{-\alpha}\hat{f}(\rho), \tag{2.32}$$

where $\alpha < n$.

When $\mathbb{I}^\alpha$ is applied to functions on $T\mathbb{S}^{n-1}$ or Z, it acts on the second variable only.

Theorem 2.3 *Let $f \in \mathcal{S}(\mathbb{R}^n), g = Rf$ and $h = Xf$. Then, for any $\alpha < n$, we have*

$$f = \frac{1}{2}(2\pi)^{1-n}\mathbb{I}^{-\alpha}R^\sharp\mathbb{I}^{\alpha-n+1}g \tag{2.33}$$

$$f = \frac{1}{|\mathbb{S}^{n-2}|}(2\pi)^{-1}\mathbb{I}^{-\alpha}X^\sharp\mathbb{I}^{\alpha-1}h. \tag{2.34}$$

Proof Employing the Fourier inversion formula (2.3) gives

$$\mathbb{I}^\alpha f(x) = (2\pi)^{-\frac{n}{2}} \int_{\mathbb{R}^n} e^{\mathrm{i}x\cdot\rho}|\rho|^{-\alpha}\hat{f}(\rho)\, d\rho. \tag{2.35}$$

Introducing polar coordinates $\rho = \sigma\xi$ gives (see Appendix A.1)

$$\mathbb{I}^\alpha f(x) = (2\pi)^{-\frac{n}{2}} \int_{\mathbb{S}^{n-1}} \int_0^\infty e^{\mathrm{i}\sigma x\cdot\xi}\sigma^{n-1-\alpha}\hat{f}(\sigma\xi)\, d\sigma\, d\xi$$

$$= (2\pi)^{-n+\frac{1}{2}} \int_{\mathbb{S}^{n-1}} \int_0^\infty e^{\mathrm{i}\sigma x\cdot\xi}|\sigma|^{n-1-\alpha}\widehat{Rf}(\xi,\sigma)\, d\sigma\, d\xi,$$

by expressing $\hat{f}$ with $\widehat{Rf}(\xi,\sigma)$ by the use of Theorem 2.2. Moreover exploiting the evenness of the Radon transform gives the integral over $(-\infty, 0)$ which added to the one above leads to

$$\mathbb{I}^\alpha f(x) = \frac{1}{2}(2\pi)^{-n+\frac{1}{2}} \int_{\mathbb{S}^{n-1}} \int_{-\infty}^\infty e^{\mathrm{i}\sigma x\cdot\xi}|\sigma|^{n-1-\alpha}\widehat{Rf}(\xi,\sigma)\, d\sigma\, d\xi.$$

Using the definition of the Riesz potential (2.9), the above can be written as

$$\mathbb{I}^{\alpha} f(x) = \frac{1}{2}(2\pi)^{-n+1} \int_{\mathbb{S}^{n-1}} \mathbb{I}^{\alpha+1-n} Rf(\xi, x\cdot\xi)\ d\xi = \frac{1}{2}(2\pi)^{-n+1} R^{\sharp}\mathbb{I}^{\alpha+1-n} Rf(x).$$

If we apply $\mathbb{I}^{-\alpha}$ to the above we yield the inversion formula

$$f(x) = \frac{1}{2}(2\pi)^{-n+1}\mathbb{I}^{-\alpha} R^{\sharp}\mathbb{I}^{\alpha+1-n} Rf(x).$$

To derive the inversion formula for the x-ray transform we require what Natterer [31] formulates in the Section of *Integration Over Spheres*, stating

$$\int_{\mathbb{R}^n} a(\theta)\ d\theta = \frac{1}{|\mathbb{S}^{n-2}|}\int_{\mathbb{S}^{n-1}}\int_{\xi^{\perp}} |\tau| a(\tau)\ d\tau\ d\xi.$$

Now using the same procedure as in (2.35) we achieve

$$\mathbb{I}^{\alpha} f(x) = (2\pi)^{-\frac{n}{2}} \frac{1}{|\mathbb{S}^{n-2}|}\int_{\mathbb{S}^{n-1}}\int_{\xi^{\perp}} e^{\mathrm{i}x\cdot\tau} |\tau|^{1-\alpha}\hat{f}(\tau)\ d\tau\ d\xi.$$

Again using Theorem 2.2, $\hat{f}$ is replaced by $\widehat{Xf}$, thus

$$\mathbb{I}^{\alpha} f(x) = (2\pi)^{-\frac{n+1}{2}} \frac{1}{|\mathbb{S}^{n-2}|}\int_{\mathbb{S}^{n-1}}\int_{\xi^{\perp}} e^{\mathrm{i}x\cdot\tau} |\tau|^{1-\alpha}\widehat{Xf}(\tau)\ d\tau\ d\xi.$$

The inner integral can be expressed by the Riesz potential, hence

$$\mathbb{I}^{\alpha} f(x) = (2\pi)^{-1}\frac{1}{|\mathbb{S}^{n-2}|}\int_{\mathbb{S}^{n-1}} \mathbb{I}^{\alpha-1} Xf(\xi, \Pi_{\xi} x)\ d\xi = (2\pi)^{-1}\frac{1}{|\mathbb{S}^{n-2}|} X^{\sharp}\mathbb{I}^{\alpha-1} Xf(x),$$

where Π_{ξ} is the orthogonal operator projecting onto the space perpendicular to ξ and the inversion for X follows. $\square$

In essence, Theorem 2.3 gives us R^{-1} and X^{-1}. For two dimensional problems it is common to use $\alpha = 0$ which simplifies (2.33) to $f = \frac{1}{4\pi} R^{\sharp}\mathbb{I}^{-1} Rf$. This is known as *Filtered Backprojection* (FBP) since $\mathbb{I}^{-1}$ acts like a filter on the data before backprojecting to recover the image and it is commonly referred to as a *ramp filter* as mentioned in [21] due to the implementation of the shape in the Fourier domain. On the other hand if $\alpha = 1$, then we have $f = \frac{1}{4\pi}\mathbb{I}^{-1} R^{\sharp} Rf$, known as *Backproject then filter* (BPF). This is possible since the filter can commute with the adjoint operator which shall be discussed later in Section 2.4 where we relate the Helgason-Ludwig condition (2.10) and (2.11) with the SVD of the Radon transform.

In a practical setting the data is noisy so using a ramp filter is not the most sensible thing to do as high frequency components are amplified. Nevertheless, the effect of noise can be somewhat controlled by the use of regularization where we limit the high frequency amplification. One specific way is to use a Hamming window and the effect of using one is illustrated in Figure 2.6b. To numerically implement a ramp filter we perform a one dimensional Fourier transform of the data using the Fast Fourier Transform (FFT). Thereafter frequency domain filtering occurs along the p direction before it is passed to spatial domain via the Inverse Fast Fourier transform (IFFT). If a Hamming window is to be implemented, the frequency domain ramp filter is convoluted with $w(n)$ defined below.

Definition 2.10 *For a discrete signal of length N, labelled by $n = 0, 1, ..., N-1$, the* ***Hamming window*** *$w(n)$ is given by*

$$w(n) = 0.54 - 0.46 \cos\left(\frac{2\pi n}{N-1}\right). \tag{2.36}$$

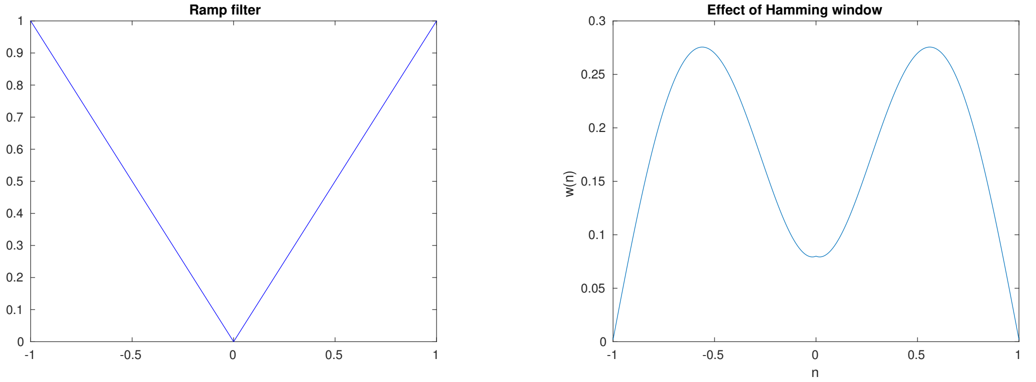

(a) The effect of a ramp filter.

(b) The effect of the Hamming window.

Figure 2.6: The different effects of both filters.

The effect of the ramp filter and Hamming window can be seen by reconstructing the sinogram from Figure 2.4a. To avoid inverse crimes the sinogram was binned by a factor of three after which 5% noise was added to the data. Finally backprojection was performed to reconstruct the image on a 90 × 90 pixel grid size. We define the **relative 2-norm error** as

$$\epsilon = \frac{\| f_{\text{rec}} - f \|_2}{\| f \|_2}, \tag{2.37}$$

which is used to calculate $\epsilon_{\text{hamming}} = 0.4501$ and $\epsilon_{\text{ramp}} = 0.4814$. Thus quantitatively apparent when noise is present, the hamming filter performs better.

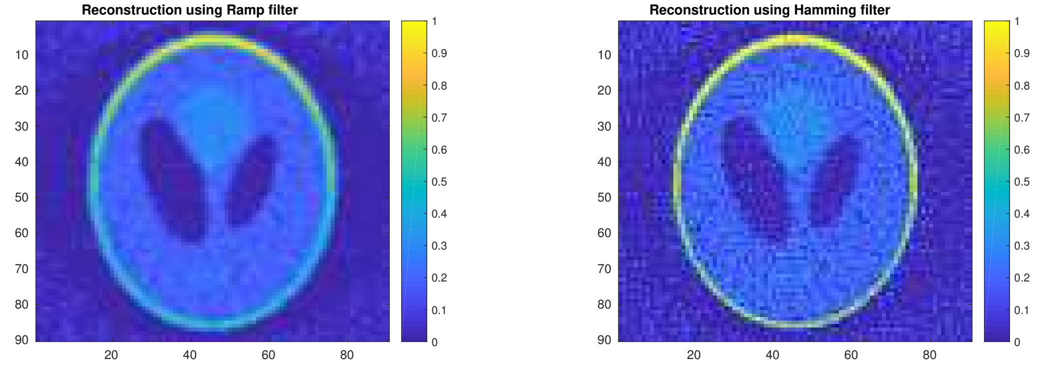

(a) Ramp filter reconstruction.

(b) Hamming filter reconstruction.

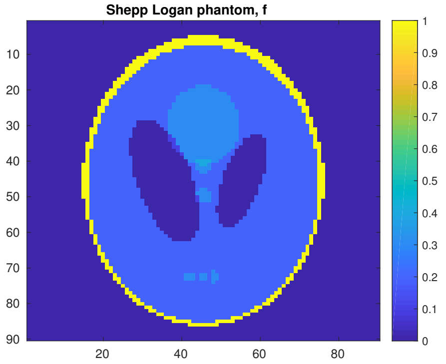

(c) Original phantom.

Figure 2.7: Reconstruction using both filters.

2.3.2 Conjugate Gradient Least Squares

A typical linear inverse problem can be formulated as an over determined system $Ax = b$ as we have more equations than the number of unknowns. So A is a rectangular matrix which is a discrete representation of the linear operator in question, x is the unknown and b is some sort of observed data. We can use the Conjugate Gradient algorithm to solve systems where such an A is not symmetric nor square. In order to solve the linear system $Ax = b$, we can solve the equivalent system

$$A^T Ax = A^T b, \tag{2.38}$$

which is symmetric positive definite. Alternatively this system is known as the normal equations associated with the *least squares* problem, formulated as

$$\min_x \; \|Ax - b\|_2^2. \tag{2.39}$$

However it is highly recommended not to solve (2.38) in this manner. Indeed the 2-norm condition number is given by $\text{Cond}_2(A^TA) = \|A^TA\|_2 \; \|(A^TA)^{-1}\|_2$. Consider $\|A^TA\|_2 = \sigma^2_{\max}(A)$ where $\sigma_{\max}(A)$ is the largest singular value of A. Note also that $\|A\|_2 = \sigma_{\max}$. Hence a similar argument for $\|(A^TA)^{-1}\|_2$ yields $\text{Cond}_2(A^TA) = \|A\|_2^2 \; \|A^{-1}\|_2^2 = \text{Cond}_2^2(A)$ suggesting that standard iterative procedures will fail miserably if the matrix is ill-conditioned as often is the case for inverse problems. If the approach used in Section 2.2 is utilised then we can store the matrix A to give intersection lengths for a ray path integral as well as simulating sinogram data which can be reshaped in the form b. To reconstruct the Shepp Logan phantom the Conjugate Gradient Least Squares CGLS algorithm (2.1) has to be implemented which is done with the aid of Hansen's Regularization toolbox [17, 16].

```
Algorithm 2.1 CGLS Let $x_0 = 0$; $d_0 = b$; $r_0 = A^Tb$; $p_0 = r_0$; $t_0 = Ap_0$;
for k = 1,2,.... until stopping criterion is reached
    $\alpha_k = \frac{\|r_{k-1}\|^2}{\|t_{k-1}\|^2}$;
    $x_k = x_{k-1} + \alpha_k p_{k-1}$;
    $d_k = d_{k-1} + \alpha_k t_{k-1}$;
    $r_k = A^T d_k$;
    $\beta_k = \frac{\|r_k\|^2}{\|r_{k-1}\|^2}$;
    $p_k = r_k + \beta_k p_{k-1}$;
    $t_k = Ap_k$;
end
```

The CGLS reconstruction of the Shepp Logan phantom is shown in Figure 2.8a where $\text{Cond}_2(A^TA) = 3.2097 \times 10^6$, which suggests a need to apply some regularization. Indeed one such method is called *Tikhonov* regularization which leads to the minimization problem

$$\min_x \; \|Ax - b\|_2^2 + \alpha^2 \| \; Lx\|_2^2. \tag{2.40}$$

The regularization parameter α controls the weight given to minimization of the regularization term relative to the minimization of the residual term. In many cases the matrix L is chosen to be the identity matrix I. The Tikhonov problem can be formulated alternatively as

$$(A^T A + \alpha^2 L^T L)x = A^T b \quad \text{and} \quad \min_x \left\| \begin{pmatrix} A \\ \alpha L \end{pmatrix} x - \begin{pmatrix} b \\ 0 \end{pmatrix} \right\|_2 . \tag{2.41}$$

There are several methods by which α can be chosen including the L curve method. These are exemplified in [16, Chapter 7]. However the method we adopt takes a small fraction of the largest singular value, $\sigma_{\max}$, of the discrete operator in question. The reconstruction present in Figure 2.8a did not converge even after 100 steps whereas the reconstruction present in Figure 2.8b converged in 32 steps. Note we have binned the simulated sinogram from Figure 2.4b by a factor of 3. Thereafter 20% noise was added before the CGLS algorithm was applied. The relative error was calculated as $\epsilon_{\text{CGLS}} = 0.4413$ and $\sigma_{\max} = 101.6476$, hence $\alpha = 0.1 \times \sigma_{\max}$.

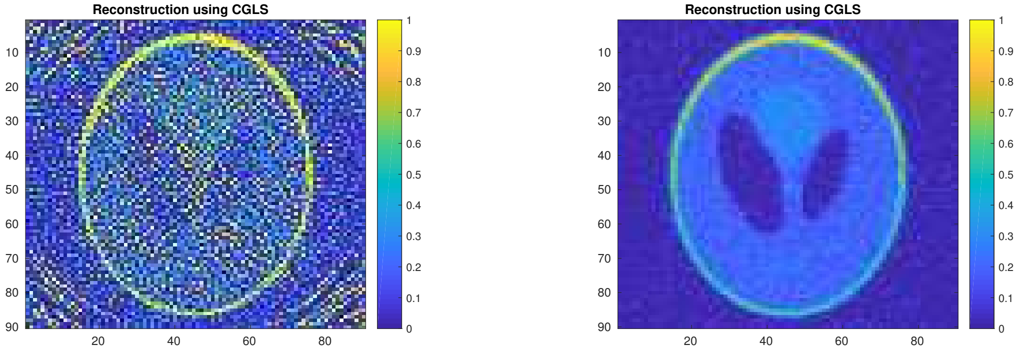

(a) CGLS with no regularization.

(b) CGLS with regularization.

Figure 2.8: Iterative reconstruction method.

2.3.3 Plane by plane reconstruction

Many algorithms are known to invert the Radon transform, including iterative reconstruction procedures using Conjugate Gradient Least Squares, for example, described earlier in Section 2.3.2. Here we want to restrict our attention to a property that follows from (2.33). Consider the case when $\alpha = 0$ and since $\mathbb{I}^{1-n}$ is a one dimensional filter, it acts on functions in $\mathbb{R}$. Now for $a \in \mathcal{S}(\mathbb{R})$,

$$\widehat{\mathbb{I}^{1-n} a}(\sigma) = |\sigma|^{n-1} \hat{a}(\sigma),$$

using the definition of the Riesz potential (2.9). Further simplification using the sign function shows

$$\widehat{\mathbb{I}^{1-n}a}(\sigma) = (\text{sgn}(\sigma))^{n-1}\sigma^{n-1}\hat{a}(\sigma) = H^{n-1}a^{n-1},$$

where H is the **Hilbert** transform defined by $\widehat{Ha}(\sigma) = -\mathrm{i}\ \text{sgn}(\sigma)\hat{a}(\sigma)$ and a^{n-1} is understood to be the $(n-1)$-th derivative with respect to the variable p. This allows us to rewrite the explicit inversion formula for the Radon transform (2.33) as

$$f = \frac{1}{2}(2\pi)^{1-n}R^{\sharp}H^{n-1}g^{n-1} \tag{2.42}$$

Suppose $n = 2$, then (2.42) is understood as

$$f = \frac{1}{4\pi}R^{\sharp}\left(-\mathrm{i}\ \text{sgn}(p)\widehat{\frac{\partial g}{\partial p}}\right)^{\vee}. \tag{2.43}$$

If this is implemented numerically, then similar results to Figures 2.7b and 2.7a can be achieved.

Let us return to the discussion on the x-ray transform. In a typical application situation (e.g. CT) where one wants to image a three dimensional volume, experimentalists would rotate the specimen (or equivalently the source and detector) about a family of planes normal to the rotation axis. For the remainder of this subsection, let $(n = 1, 2, 3)$. The x-ray transform can also be defined on a plane in $\mathbb{R}^3$ and we have a coordinate frame of reference in mind illustrated in Figure 2.9. For $\eta \in \mathbb{S}^2$, let $\eta^{\perp} = \{\xi \in \mathbb{R}^3 \mid \xi \cdot \eta = 0\}$, $\mathbb{R}\eta = \{s\eta \mid s \in \mathbb{R}\}$ and $\mathbb{S}^1_{\eta} = \{\xi \in \eta^{\perp} \mid |\xi| = 1\}$ be the unit circle in $\eta^{\perp}$. Given $s \in \mathbb{R}$, let $s\eta + \eta^{\perp}$ be the plane through $s\eta$ parallel to $\eta^{\perp}$ and $\iota_{s,\eta} : s\eta + \eta^{\perp} \hookrightarrow \mathbb{R}^3$ be the identical embedding.

The family of oriented lines in the plane $s\eta + \eta^{\perp}$ is parameterized by points of the manifold $T\mathbb{S}^1_{\eta} = \{(\xi, x) \mid \xi \in \mathbb{S}^1_{\eta}, x \in \eta^{\perp}, \xi \cdot x = 0\}$ such that a point $(\xi, x) \in T\mathbb{S}^1_{\eta}$ corresponds to the line $\{s\eta + x + t\xi \mid t \in \mathbb{R}\}$. We define the x-ray transform $X_{\eta,s}f(\xi, x)$ on the plane $s\eta + \eta^{\perp}$ as

$$X_{\eta,s} : \mathcal{S}(s\eta + \eta^{\perp}, \mathbb{R}^2) \to \mathcal{S}(T\mathbb{S}^1_{\eta}), \tag{2.44}$$

by the following formula

$$X_{\eta,s}f(\xi, x) = \int_{-\infty}^{\infty} f(s\eta + x + t\xi)\ \mathrm{d}t. \tag{2.45}$$

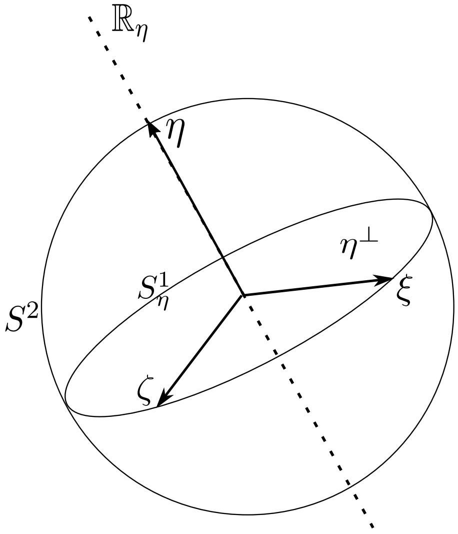

Figure 2.9: Geometrical Interpretation.

Consider the plane case $n = 2$ in which X is identical to the Radon transform. In this case the formal adjoint $B = X^\sharp : \mathcal{S}(T\mathbb{S}^1) \to C^\infty(\mathbb{R}^2)$, the backprojection operator, is well defined and given by

$$Bh(x) = \frac{1}{2\pi} \int_{\mathbb{S}^1} h(\xi, \xi \cdot x)\ d\xi \tag{2.46}$$

for $h \in \mathcal{S}(T\mathbb{S}^1)$. Readers must note that the function $Bh(x)$ is C^∞-smooth and bounded on $\mathbb{R}^2$ but does not decay fast enough to be in the Schwartz class. Thus we understand the Fourier transform in the distribution sense.

We then have an inversion formula in frequency domain due to Natterer [31] for data $h(\xi, x) = X_{\eta,s} f(\xi, x)$ in the range of X

$$\hat{f}(y) = |y|\widehat{Bh(x)}, \tag{2.47}$$

which means that inversion is performed by a *ramp filter* applied to the backprojected data. This operation can be performed *slice by slice* to invert the x-ray transform for $n = 3$, in which case data is needed only for $\xi \in \eta^\perp$ for some fixed *rotation axis* $\eta \in \mathbb{S}^2$. In this case the slice by slice backprojection operator $B_\eta : \mathcal{S}(\mathbb{R} \times T\mathbb{S}^1_\eta) \to C^\infty(\mathbb{R}^3)$, defined by

$$B_\eta h(x) = \frac{1}{2\pi} \int_0^{2\pi} h(\xi(\phi), \xi(\phi) \cdot x) \mathrm{d}\phi, \quad \text{for} \quad x \in \eta^\perp, \tag{2.48}$$

where $\xi(\phi) = \cos\phi e_1 + \sin\phi e_2$ and $\xi^\perp(\phi) = \cos\phi e_2 - \sin\phi e_1$ with respect to an orthonormal basis (e_1, e_2) of $\eta^\perp$. The value of $B_\eta h$ at a point $x \in \mathbb{R}^3$ is just the average of the function h over all lines passing through x and orthogonal to η. The reconstruction formula (2.47) becomes

$$F_{\eta^\perp}[f(s,y)] = |\Pi_\eta y|\widehat{B_\eta h(x)}, \tag{2.49}$$

where $s = x \cdot \eta$ and $\Pi_\eta = I - \frac{\eta\eta^\perp}{|\eta|}$. To implement this strategy of plane by plane inversion we simulate data using our forward projector described in Section 2.2. For the reconstruction aspect we will employ formula (2.43) where one would presume we are asking for trouble; differentiation is an ill-posed problem. The question we ask ourselves is how do we develop an algorithm which would handle the ill-posedness of $\frac{\partial g}{\partial p}$ and be easy to implement. To overcome this scenario we perform a regularised derivative, carried out in the Fourier domain using the Hamming window to regularise. Firstly we carry out a one-dimensional Discrete Fourier transform using the FFT, finishing off with multiplication by $-\mathrm{i}\sigma w(n)$. This strategy will be of importance in Section 5.5. Upon completion of this process we pass the differentiated data into frequency space multiplying by $-\mathrm{i}$ before sending everything back to spatial domain. Lastly backprojection is performed in the manner described in the previous sections.

In Section 5.4, we define several phantoms for tensor fields of which we utilize just a single component of the sharp (discontinuous) tensor field, f_{11}, to illustrate the procedure mentioned above. The phantom used to simulate data is defined on a $256 \times 256 \times 256$ voxel grid. The number of views (or projections) are 180 and the total number of rays fired are 135. So the data is a $256 \times 135 \times 180$ array which is binned by a factor of 3 and we reduce the number of slices to 90 to give an array of size $90 \times 45 \times 60$ before adding 5% pseudo-random noise. The relative error for the reconstruction present in 2.10a is $\epsilon_{3D} = 0.3219$. We generate the phantom for comparison purposes again on a $90 \times 90 \times 90$ voxel grid since this is the voxel grid size on which we reconstruct.

2.4 Singular Value Decomposition

Let A be a rectangular (or even square) matrix of size $M \times N$ and assuming that $M \geq N$ as we generally have more equations than the number of unknowns in practical inverse problems. Then the Singlar Value Decomposition (SVD) of A is of the form

$$A = U\Sigma V^T = \sum_{i=1}^{N} u_i \sigma_i v_i^T, \tag{2.50}$$

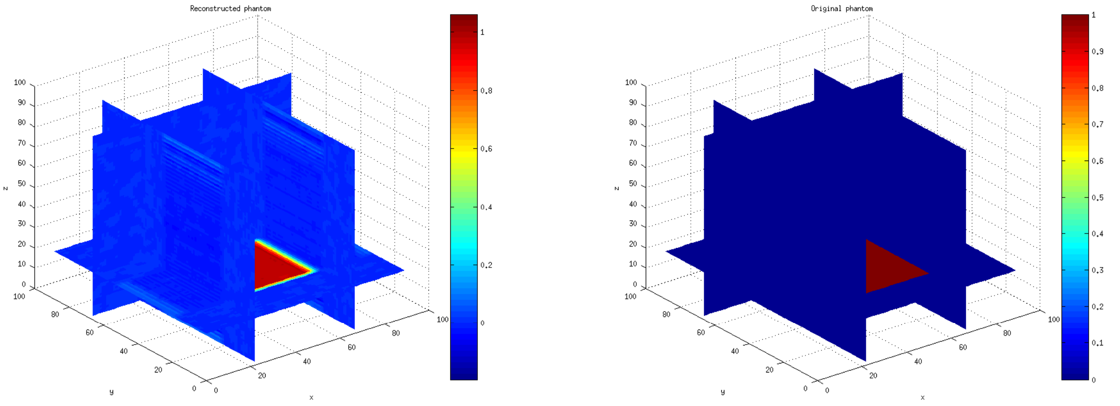

(a) Slice by slice reconstruction. (b) The original phantom.

Figure 2.10: Three dimensional reconstruction.

where $U = (u_1, ..., u_N)$, a matrix of size $M \times N, V = (v_1, ..., v_N)$, a matrix of size $N \times N$. The columns of these matrices are orthonormal such that $U^T U = V^T V = I_N$. The diagonal matrix $\Sigma = \text{diag}(\sigma_1, ..., \sigma_N)$ has non-negative diagonal elements called *singular values* such that $\sigma_1 \geq \sigma_2 \geq .... \geq \sigma_N \geq 0$. The vectors u_i, and v_i are called the left and right *singular vectors* of A, respectively. Generally two characteristic features are present in the SVD of a discretized operator, namely

- The singular values σ_i decay gradually to zero with no particular gap in the spectrum.
- The left and right singular vectors u_i and v_i tend to have rapid oscillations in the sign of their elements as the index i increases.

These properties give an insight into classifying the nature of ill-posedness of the problem. To illustrate this we take the approach of Bertero and Boccacci [5] to identify the SVD of the Radon transform in two dimension. Alternatively [31] specifies a different approach deriving the SVD in arbitrary dimension. Moreover [28] suggests a SVD for the x-ray transform.

We would like to derive the SVD of the Radon transform as an operator from $L^2(\Omega)$ into $L^2(Z, w^{-1})$, where $w(p) = (1 - p^2)^{\frac{1}{2}}$ and Ω being the unit ball (disk), i.e. $\mathbb{S}^1 \subset \mathbb{R}$. Thus

$$\|f\|^2_{L^2(\Omega)} = \int_\Omega |f(x)|^2 \, dx \tag{2.51}$$

Note that $w(p)$ is the half length of the chord obtained by intersecting the disk with a straight line having signed distance p from the origin. Hence the Radon transform which is zero outside Ω is

$$Rf(\xi, p) = \int_{-w(p)}^{w(p)} f(p\xi + y)\ dy, \quad |p| \leq 1. \tag{2.52}$$

First we need to check to see if R and $R^\sharp$ are both bounded on $L^2(\Omega)$ and $L^2(Z, w^{-1})$. which Natterer [31] does show. Consider the integrand in the RHS of (2.52) as the scalar product of the function f and the function equal to one over the interval $[-w(p), w(p)]$. Applying Cauchy-Schwartz inequality (see Appendix A) to this yields

$$|Rf(\xi, p)|^2 \leq 2w(p) \int_{-w(p)}^{w(p)} |f(p\xi + y)|^2\ dy. \tag{2.53}$$

Integrating across the diameter of the disc in (2.53) gives

$$\int_{-1}^{1} w^{-1}(p)|Rf(\xi, p)|^2\ dp \leq 2 \int_{-1}^{1} dp \int_{-w(p)}^{w(p)} |f(p\xi + y)|^2\ dy = 2 \int_{\Omega} |f(x)|^2\ dx. \tag{2.54}$$

This suggests the codomain of the Radon transform for functions on the cylinder, $g(\xi, p)$, will need a certain weighted norm, defined as

$$\|g\|_{L^2(Z, w^{-1}(p))} = \int_0^{2\pi} d\phi \int_{-1}^{1} \frac{|g(\xi, p)|^2}{w(p)}\ dp. \tag{2.55}$$

Now if we integrate inequality (2.54) with respect to ϕ, it is sufficient to show R is a bounded operator and the following bound is obtained

$$\|Rf\|_{L^2(Z, w^{-1}(p))} \leq \sqrt{4\pi}\|f\|_{L^2(\Omega)}, \tag{2.56}$$

suggesting that the largest singular value of R is $\sqrt{4\pi}$ and $\|R\|_2 = \sqrt{4\pi}$. Since R is bounded, this suggests that we can classify R as an integral operator of the *Hilbert-Schmidt* class.

The singular system of R can be obtained by representing a function $g(\xi, p) \in L^2(Z, w^{-1}(p))$, for fixed ξ, as a series of *Chebyshev polynomials of the second kind*, which are orthogonal to the weight function $w(p)$ and noted earlier in Definition 2.6. Consider the change of variable $p = \cos\theta, 0 \leq \theta \leq \pi$, in (2.13), giving

$$U_l(\cos\theta) = \frac{\sin(l+1)\theta}{\sin\theta}. \tag{2.57}$$

Therefore utilizing (2.57) we see that

$$\int_{-1}^{1} w(p)U_l(p)U_{l'}(p)\ dp = \int_0^{\pi} \frac{\sin[(l+1)\theta]\sin[(l'+1)\theta]}{\sqrt{1-\cos^2\theta}} \sin\theta\ d\theta$$

$$= \int_0^\pi \sin[(l+1)\theta]\sin[(l'+1)\theta]\ d\theta = \frac{\pi}{2}\delta_{l,l'}. \tag{2.58}$$

Observe that $g(\cos\theta) \in L^2$ since

$$\int_{-1}^{1} |g(p)|^2 \frac{dp}{w(p)} = \int_0^\pi |g(\cos\theta)|^2\ d\theta,$$

which means $g(\cos\theta)$ can be represented by the trigonometric series

$$g(\cos\theta) = \sum_{l=0}^{\infty} c_l \sin[(l+1)\theta], \quad \text{with}$$

$$c_l = \frac{2}{\pi}\int_0^\pi g(\cos\theta)\sin[(l+1)\theta]\ d\theta. \tag{2.59}$$

Thus $g(\xi, p)$ can be represented as a series expansion in $u_l(p) = w(p)U_l(p)$ for fixed ξ, which leads us to consider subspaces of $L^2(Z, w^{-1}(p))$ denoted as $L_l^2(Z, w^{-1}(p))$. These subspaces contain the functions of the form

$$g_l(\xi, p) = \sqrt{\frac{2}{\pi}} w(p)U_l(p)u(\xi), \quad l = 0, 1, ... \tag{2.60}$$

where $u(\xi)$ is an arbitrary square integrable function of ξ. With the aid of (2.55) and (2.58) we realise that

$$\|g_l\|^2_{L^2(Z,w^{-1}(p))} = \int_0^{2\pi} d\phi\ \frac{2}{\pi}\int_{-1}^{1}\frac{dp}{w(p)}|w(p)U_l(p)u(\xi)|^2$$

$$= \frac{2}{\pi}\int_0^{2\pi} d\phi \int_{-1}^{1} |w(p)U_l^2(p)u^2(\xi)|\ dp = \int_0^{2\pi} |u(\xi)|^2\ d\phi. \tag{2.61}$$

Consider $L^2(Z, w^{-1}(p)) = L_0^2(Z, w^{-1}(p)) \oplus L_1^2(Z, w^{-1}(p)) \oplus L_2^2(Z, w^{-1}(p)) \oplus ......$ and it is quite apparent due to the orthogonality of the Chebyshev polynomials that the subspaces $(L_l^2(Z, w^{-1}(p))$ are orthogonal. The strategy we employ is to find eigenfunctions and eigenvalues of RR^*. In order to achieve our goal it is necessary to show that RR^* transforms a function of $(L_l^2(Z, w^{-1}(p))$ into another function of $(L_l^2(Z, w^{-1}(p))$. The adjoint operator, R^*, is defined below

$$R^*g(x) = \int_{\mathbb{S}^1} g(\xi, \xi\cdot x)(w(\xi\cdot x))^{-1}\ d\xi. \tag{2.62}$$

Note R^* is not exactly backprojection as we are utilizing the $L^2(Z, w^{-1}(p))$ norm and one can check quite easily that $\langle Rf(\xi,p), g(\xi,p)\rangle_{L^2(Z,w^{-1}(p))} = \langle f(x), R^*g(x)\rangle_{L^2(\Omega)}$. Of course by exhanging the order of integration via Fubini's theorem and a change of variables, we have

$$\langle Rf(\xi,p), g(\xi,p)\rangle_{L^2(Z,w^{-1}(p))} = \int_{-1}^{1}\frac{dp}{w(p)}\int_0^{2\pi} d\phi \left(\int_{-w(p)}^{w(p)} dy f(p\xi + y)\right) g^*(\xi, p)$$

$$= \int_0^{2\pi} \left(\int_{-1}^{1} dp \int_{-w(p)}^{w(p)} dy f(p\xi + y) \frac{g^*(\xi, p)}{w(p)} \right) d\phi$$

$$= \int_\Omega f(x)\, dx \left(\int_0^{2\pi} \frac{g^*(\xi, \xi \cdot x)}{w(\xi \cdot x)}\, d\phi \right) = \langle f, R^* g \rangle_{L^2(\Omega)} \tag{2.63}$$

Since g_l is a function of $L^2_l(Z, w^{-1}(p))$ defined in (2.60), we obtain using (2.52) and (2.62), the result

$$RR^* g_l(\xi, p) = \sqrt{\frac{2}{\pi}} \int_{-w(p)}^{w(p)} dy \int_0^{2\pi} d\phi'\; U_l[\xi' \cdot (p\xi + y)] u(\xi'). \tag{2.64}$$

By exchanging the integration order in (2.64), let us consider the integral

$$E(\xi, \xi'; p) = \int_{-w(p)}^{w(p)} U_l[\xi' \cdot (p\xi + y)]\, dy. \tag{2.65}$$

Explicitly $\xi = (\cos\phi, \sin\phi)$ and $\xi^{'} = (\cos\phi', \sin\phi')$, thus $\xi \cdot \xi' = \cos(\phi - \phi')$ and $\xi^\perp \cdot \xi' = -\sin(\phi - \phi')$. Furthermore, say, $y = t\xi^\perp$ and suppose $p = \cos\theta$ and $\psi = \phi - \phi'$, allowing us to transform (2.65) into

$$E(\xi, \xi'; \cos\theta) = \int_{-\sin\theta}^{\sin\theta} U_l(\cos\theta\cos\psi - t\sin\psi)\, dt. \tag{2.66}$$

Using the substitution $u = \cos\theta\cos\psi - t\sin\psi$, (2.66) becomes

$$E(\xi, \xi'; \cos\theta) = \int_{\cos(\theta-\psi)}^{\cos(\theta+\psi)} \frac{U_l(u)}{\sin\psi}\, du. \tag{2.67}$$

Yet again introducing a new variable $u = \cos\eta$ in (2.67) and using (2.57) gives

$$E(\xi, \xi'; \cos\theta) = \frac{1}{\sin\psi} \int_{\theta-\psi}^{\theta+\psi} \sin[(l+1)\eta]\, d\eta$$

$$= \frac{1}{\sin\psi} \left[-\frac{1}{l+1} \left[\cos\{(l+1)\eta\}\right]_{\theta-\psi}^{\theta+\psi} \right] = \frac{2}{l+1} \frac{\sin[(l+1)\psi]}{\sin\psi} \sin[(l+1)\theta]. \tag{2.68}$$

The above expression (2.68) for $E(\xi, \xi^\perp; \cos\theta)$ should be substituted into (2.64) by reversing the change of variables $\psi = \phi - \phi'$ and $\theta = \arccos p \Rightarrow \sin[(l+1)\arccos p] = \sin[(l+1)\theta] = \sin\theta U_l(\cos\theta) = \sqrt{1-p^2}U_l(\cos\theta) = w(p)U_l(p)$. In this manner we achieve

$$RR^* g_l(\xi, p) = \sqrt{\frac{2}{\pi}}\, 2\pi\, \frac{2}{l+1}\, w(p) U_l(p) \left(\frac{1}{2\pi} \int_0^{2\pi} \frac{\sin[(l+1)(\phi - \phi')]}{\sin(\phi - \phi')} u(\xi')\, d\phi' \right), \tag{2.69}$$

which can be written as

$$RR^* g_l(\xi, p) = \frac{4\pi}{l+1} \sqrt{\frac{2}{\pi}}\; w(p) U_l(p) \bar{u}(\xi), \quad \text{where}$$

$$\bar{u}(\xi) = \frac{1}{2\pi} \int_0^{2\pi} \frac{\sin[(l+1)(\phi - \phi')]}{\sin(\phi - \phi')} u(\xi')\ d\phi'. \tag{2.70}$$

The integral operator in (2.70) is usually seen in the theory for Fourier series. This operator is called the *Fejér* kernel which takes u to its truncated Fourier series. In essence (2.70) actually shows that $RR^*(L_l^2(Z, w^{-1}(p))) \subseteq L_l^2(Z, w^{-1}(p))$. This restriction of the operator RR^* to the subspace $L_l^2(Z, w^{-1}(p))$ is equivalent to the Fejér kernel defined in (2.70). Hence it is possible to diagonalize RR^* by diagonalizing its restrictions to the subspaces $L_l^2(Z, w^{-1}(p))$. Due to the completeness of the Chebyshev polynomials we can find all eigenfunctions and eigenvalues of RR^*. Note that the integral operator given in (2.70) is a *finite rank* integral operator as can be seen by the following identity

$$\frac{1}{2\pi} \frac{\sin[(l+1)(\phi - \phi')]}{\sin(\phi - \phi')} = \sum_{k=0}^{l} Y_{l-2k}(\xi) Y_{l-2k}^*(\xi'), \tag{2.71}$$

where $Y_l(\xi) = \frac{1}{\sqrt{2\pi}} e^{-il\phi}$ are known as the *Spherical Harmonics* of degree l. These functions are orthonormal on $[0, 2\pi]$ owing to which $Y_{l-2k}(\xi)$ are the eigenfunctions of the integral operator (2.70). With this in mind let us define

$$u_{l,k}(\xi, p) = \sqrt{\frac{2}{\pi}} w(p) U_l(p) Y_{l-k}(\xi), \quad k = 0, 1, 2, ...l \tag{2.72}$$

which are orthonormal functions in $L^2(Z, w^{-1}(p))$. From (2.70) and (2.71) we realise that

$$RR^* u_{l,k} = \sigma_l^2 u_{l,k}, \quad k = 0, 1, 2, ..., m, \tag{2.73}$$

where

$$\sigma_l = \sqrt{\frac{4\pi}{l+1}} \tag{2.74}$$

It can also be shown that

$$v_{l,k}(x) = \frac{1}{\sigma_l} R^* u_{l,k} = \sqrt{2l+2} Q_{l,|l-2k|}(|x|) Y_{l-2k}\left(\frac{x}{|x|}\right), \tag{2.75}$$

where

$$Q_{l,m}(r) = r^m P_{\frac{1}{2}(m+l)}^{(0,m)}(2r^2 - 1) \tag{2.76}$$

and $P_n^{(\alpha,\beta)}(t)$ denote the *Jacobi* polynomials.

The singular values σ_l decay more slowly than $\frac{1}{\sqrt{l+1}}$ suggesting the Radon transform is only mildly ill posed. If we discretize the Radon transform in a similar fashion to Section 2.2 and calculate the SVD of the forward projection matrix A, we are able to confirm this result numerically as shown in Figure 2.11. Here a log log plot is used to visualize the decay to zero. Note the sudden drop of singular values near the end of the graph. Usually such an occurence happens when dealing with singular values of numerically rank deficient matrices. A detailed explanation can be found in Chapter 3 of [16].

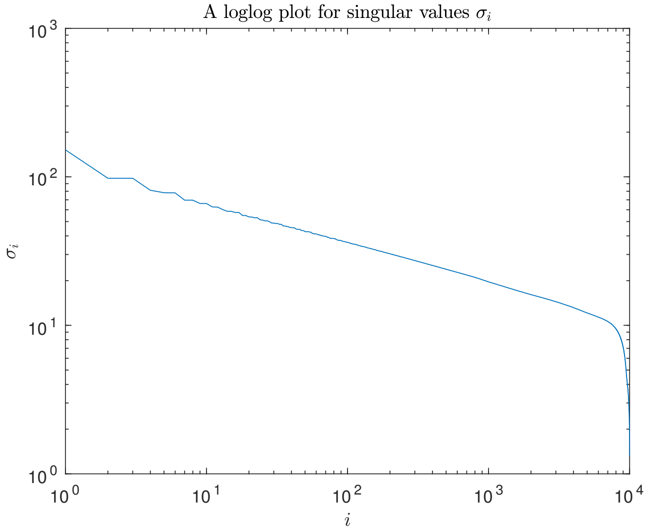

Figure 2.11: Singular values, σ_i, decay gradually to 0.

2.5 Stability Estimates

To deduce stability results for the Radon and x-ray transforms we need to consider them as operators between suitable Sobolev spaces. In particular the inverses are not continuous between L^2 spaces. Prior to this we state the definition of a Sobolev space.

Definition 2.11 *The Sobolev space $H^\alpha(\mathbb{R}^n)$ or H^α of real order α is defined by*

$$H^\alpha = \{f \in \mathcal{S}'(\mathbb{R}^n) \ : \ (1+|\xi|^2)^{\frac{\alpha}{2}}\hat{f} \in L^2(\mathbb{R}^n)\}. \tag{2.77}$$

So H^α is a Hilbert space with the following norm and inner product

$$\|f\|_{H^\alpha} = \left(\int_{\mathbb{R}^n} (1+|\xi|^2)^\alpha |\hat{f}(\xi)|^2 \, d\xi\right)^{\frac{1}{2}}, \tag{2.78}$$

If $\alpha = 0$ above in (2.78) we have the usual L^2 inner product

$$\langle f, g\rangle = \int_{\mathbb{R}^n} \hat{f}(\xi)\bar{\hat{g}}(\xi) \, d\xi. \tag{2.79}$$

Consider $\Omega \subset \mathbb{R}^n$, then we define

$$H_0^\alpha(\Omega) = \{f \in H^\alpha(\mathbb{R}^n) \ : \ \operatorname{supp}(f) \subseteq \bar{\Omega}\} \tag{2.80}$$

where the support of $f \in \mathcal{S}'$ is the complement of the points having a neighbourhood in which f vanishes (i.e. f vanishes for all C^∞-functions with support in the neighbourhood). This is a closed subspace. The Sobolev spaces on $Z = \mathbb{S}^{n-1} \times \mathbb{R}$ and $T\mathbb{S}^{n-1}$ are defined as follows

$$\|g\|^2_{H^\alpha(Z)} = \int_{\mathbb{S}^{n-1}} \int_{\mathbb{R}^1} (1+\sigma^2)^\alpha |\hat{g}(\xi,\sigma)|^2 \, d\sigma \, d\xi, \tag{2.81}$$

$$\|g\|^2_{H^\alpha(T\mathbb{S}^{n-1})} = \int_{\mathbb{S}^{n-1}} \int_{\xi^\perp} (1+\eta^2)^\alpha |\hat{g}(\xi,\eta)|^2 \, d\eta \, d\xi, \tag{2.82}$$

Theorem 2.4 *Consider $f \in H_0^\alpha(\Omega)$ with Ω being a bounded set. Then there exists positive constants $c(\alpha,n)$ and $C(\alpha,n)$ such that*

$$c(\alpha,n)\|f\|_{H_0^\alpha(\Omega)} \leq \|Rf\|_{H^{\alpha+\frac{n-1}{2}}(Z)} \leq C(\alpha,n)\|f\|_{H_0^\alpha(\Omega)}, \tag{2.83}$$

$$c(\alpha,n)\|f\|_{H_0^\alpha(\Omega)} \leq \|Rf\|_{H^{\alpha+\frac{1}{2}}(T\mathbb{S}^{n-1})} \leq C(\alpha,n)\|f\|_{H_0^\alpha(\Omega)}, \tag{2.84}$$

Proof. See [31, Chapter 2.5], Theorem 5.1. □

Theorem 2.4 shows that the Radon and x-ray transforms can be both considered as functions from $H_0^\alpha(\Omega) \to H^{\alpha+\frac{n-1}{2}}(Z)$ and $H_0^\alpha(\Omega) \to H^{\alpha+\frac{1}{2}}(T\mathbb{S}^{n-1})$ which suggests they have continuous inverses. Note that the Radon transform increases smoothness by $\frac{n-1}{2}$ derivatives whereas the x-ray transform increases smoothness by $\frac{1}{2}$ derivatives.

This completes the discussion on well known results within the literature that are to be used throughout this thesis. Our goal and aim is to introduce examples of rich tomography and use the results within this chapter to derive novel reconstruction algorithms, ideally implementing them numerically in an innovative manner. Hence we start our journey by introducing several transforms in the next chapter.

Chapter 3

Ray Transforms on Euclidean Space

Conventional tomography reconstructs an image from a single measurement per ray. However many applications as we shall see in due course make several measurements for each ray. Our aim is to reconstruct higher dimensional objects which can be generalised as tensors of type (n, m). Throughout this thesis, our attention is restricted to orthonormal bases (e_1, e_2, e_3) of $\mathbb{R}^3$ for several modalities, thus we do not distinguish between co- and contravariant tensors. The design of reconstruction algorithms are hugely affected by this subtle difference in measurements which can be seen by the formulation of the model for x-ray tomography. For a monochromatic x-ray beam (one energy) the initial intensity, $u(p = -\infty)$, is known to us at the source as well as the final intensity, $u(p = \infty)$, of the beam at the detector. One important result, the **Beer-Lambert** law [4], states that a beam of electromagnetic radiation is attenuated exponentially as it travels through an object which implies that absorption is $-\log\left(\frac{u(\infty)}{u(-\infty)}\right)$.

The derivation for this is as follows. Consider the transport equation, a first order hyperbolic PDE,

$$\xi \cdot \nabla\ u(x, \xi) = -f(x)\ u(x, \xi), \tag{3.1}$$

where $f(x)$ is the attenuation coefficient. Fixing one direction ξ (for one specific beam) and integrating gives

$$\int_{p=-\infty}^{\infty} \frac{du}{u} = \int_{p=-\infty}^{\infty} -f(x + p\xi)\ dp \Rightarrow \frac{u(p = \infty)}{u(p = -\infty)} = \exp\left(\int_{p=-\infty}^{\infty} -f(x + p\xi)\ dp\right)$$

$$\Rightarrow u(p = \infty) = u(p = -\infty) \exp\left(\int_{p=-\infty}^{\infty} -f(x + p\xi)\ dp\right).$$

Now observe the effect on the formulation when u is a rank one (vector) or a rank two tensor (3×3 matrix). If we examine the transport equation for one ray, we have an ODE

$$\frac{d}{dp}\, u = -f(p)u(p),$$

which causes issues when $f(p)$ is non-scalar since this does not have a general solution $u(p) = \exp(-\int f(p)\ dp)u(0)$. One may ponder using the matrix exponential in such a circumstance where $\exp(-\int f(p)\ \mathrm{d}p) = \sum_{k=0}^{\infty} \frac{(-\int f(p)\ \mathrm{d}p)^k}{k!}$. However, this does not satisfy $\frac{d}{dp}\ \exp(-\int f(p)\ \mathrm{d}p) = -f(p)\exp(-\int f\ \mathrm{d}p)$ implying that $\int f(p)$ has to commute with its derivative for a solution. This motivates our discussion to define several ray transforms in Euclidean space that can potentially be utilised in many applications. In Section 3.1 we introduce the Non-Abelian Ray Transform (NART) and in Section 3.2 we introduce tensor ray transforms with complete inversion formulae. Furthermore, we briefly indicate current work in this field about range and stability. In Section 3.3 we relate the transforms together which will be of importance in Section 5.1.2 of Chapter 5.

3.1 Non-Abelian Ray Transform

For certain applications, the order in which the ray traverses the object of interest matters unlike x-ray CT where the ray travelling in one direction gives the same attenuation coefficient as the ray travelling in the reverse direction. For example, SPECT (Single-Photon Emission Computed Tomography), a nuclear medicine imaging technique using gamma rays, is found to have differences in data depending on the direction of travel, ξ. Thus these types of problems are classed as non-abelian problems. Other examples include Electromagnetic Polarization Tomography (EPT) and applications involving weighted Radon transforms usually have such a property.

We will now introduce the notation used for Non-Abelian Ray Transform (NART) problems, following [12], and the references therein. For reasons that will become apparent we need only the planar case. For $0 \leq j \leq 2$, let $A_j(t)$ be C^∞ $n \times n$ matrix valued functions on $\mathbb{R}^2$, with compact support contained in the ball Ω_R, where R is some radius. We denote by $\xi = (\xi_1, \xi_2)$ a vector in $\mathbb{S}^1$ and let $\Sigma(x, \xi)$ be the matrix solution of the partial differential equation

$$\xi \cdot \nabla\Sigma(x,\xi) = (A_1(x)\xi_1 + A_2(x)\xi_2 + A_0(x))\Sigma(x,\xi), \tag{3.2}$$

such that $\Sigma(x+t\xi,\xi) \to I_n$, as $t \to -\infty$. We then define the limit of $\Sigma(x+t\xi,\xi)$ as $t \to \infty$ to be the NART of $A(x,\xi) = (A_1(x)\xi_1 + A_2(x)\xi_2 + A_0(x))$, which we denote by $S(A)$.

This formulation is analogous to the transport equation in x-ray tomography described earlier. Note we have allowed a first order dependence of the right hand side on the direction ξ. This case does not include polarized light tomography (with phase measurements) in which there is a quadratic dependence on direction [32]. Moreover we elaborate the usage of $A(x,\xi)$ in Chapter 4 where this dependence on direction is discussed.

Definition 3.1 *The matrices $A_j^{(1)}(x)$, $0 \le j \le 2$ and $A_j^{(2)}(x)$,$0 \le j \le 2$ are said to be* gauge equivalent *if there exists a nonsingular $n \times n$ C^∞ matrix $g(x)$ such that $g(x) = I_n$ for $|x| \ge R$ and*

$$\begin{aligned} A_j^{(2)} &= gA_j^{(1)}g^{-1} + \frac{\partial g}{\partial x_j}g^{-1}, j = 1,2, && (3.3)\\ A_0^{(2)} &= gA_0^{(1)}g^{-1}. && (3.4)\end{aligned}$$

The significance of this is that gauge equivalent $A^{(1)}(x,\xi)$ and $A^{(2)}(x,\xi)$ have the same NART, so we can can hope at best that the inverse problem has a unique solution up to gauge equivalence. Indeed [12] proves the following theorem which depends on advanced complex analysis techniques.

Theorem 3.1 *(Eskin) Suppose $A_j^{(1)}(x)$ and $A_j^{(2)}(x)$, $0 \le j \le 2$, are C^∞ compactly supported matrices with the same NART. Then $A_j^{(1)}(x)$, $0 \le j \le 2$ and $A_j^{(2)}(x)$, $0 \le j \le 2$ are gauge equivalent.*

3.2 Tensor Ray Transforms

In order to describe ray transforms of tensor fields we fix some notation. In a similar manner to our introduction of the family of lines in Section 2.3.3, we define the family of oriented lines in $\mathbb{R}^n$ to be points on the manifold $T\mathbb{S}^{n-1}$. For example, in three dimensions an oriented line $l \subset \mathbb{R}^3$ is uniquely represented as $l = \{x + t\xi \mid t \in \mathbb{R}\}$ with $(\xi, x) \in T\mathbb{S}^2$.

Definition 3.2 *Let us denote the complex vector space of symmetric* $\mathbb{R}$*-bilinear maps* $\mathbb{R}^n \times \mathbb{R}^n \to \mathbb{C}$ *by* $S^2\mathbb{C}^n$ *. The elements of this space are (complex-valued) symmetric tensors of second rank on* $\mathbb{R}^n$*.*

We identify a complex symmetric tensor $f \in S^2\mathbb{C}^n$ with the $\mathbb{C}$-linear operator, $f : \mathbb{C}^n \to \mathbb{C}^n$. For two tensors $f, g \in S^2\mathbb{C}^n$, we denote by $f \cdot g$ the contraction of the product of two tensors and $f \cdot \eta$, where $\eta \in \mathbb{R}^n$, the contraction of a tensor with a vector. This coincides with matrix multiplication of components. Thus $(f \cdot \xi) \cdot \eta = (f \cdot \eta) \cdot \xi$ where $\eta, \xi \in \mathbb{R}^n$. Here we would like to draw the difference between a local contraction and the usual definition for an inner product $\langle \circ, \circ \rangle$, which represents integration over space. For example, given an orthonormal basis (e_1, e_2, e_3) of $\mathbb{R}^3$, a tensor $f \in S^2\mathbb{C}^3$ can be represented by the symmetric 3×3 matrix (f_{jk}), $f_{jk} = (f \cdot e_j) \cdot e_k$. The Hermitian scalar product on $S^2\mathbb{C}^n$ can be written as $f \cdot g = \sum_{j,k=1}^{3} f_{jk}\bar{g}_{jk}$ independently of the choice of an orthonormal basis. Although the discussion can continue in arbitrary dimension n, we will restrict our attention to $n = 2, 3$.

3.2.1 The Longitudinal Ray Transform

The Longitudinal Ray Transform (LRT),

$$I : \mathcal{S}(\mathbb{R}^3; \mathbb{C}^3) \to \mathcal{S}(T\mathbb{S}^2), \quad I : \mathcal{S}(\mathbb{R}^3; S^2\mathbb{C}^3) \to \mathcal{S}(T\mathbb{S}^2),$$

defined on vector and tensor fields respectively by

$$If(\xi, x) = \int_{-\infty}^{\infty} f(x + t\xi) \cdot \xi \, \mathrm{d}t, \tag{3.5}$$

$$If(\xi, x) = \int_{-\infty}^{\infty} (f(x + t\xi) \cdot \xi) \cdot \xi \, \mathrm{d}t. \tag{3.6}$$

The LRT can also be defined on a plane in $\mathbb{R}^3$. Let $\eta_{\mathbb{C}}^{\perp}$ be the complexification of $\eta^{\perp}$ and we follow the notation introduced in Section 2.3.3. We define the LRT on the plane $s\eta + \eta^{\perp}$

$$I_{\eta,s} : \quad \mathcal{S}(s\eta + \eta^{\perp}; \eta_{\mathbb{C}}^{\perp}) \to \mathcal{S}(T\mathbb{S}_{\eta}^{1}) \tag{3.7}$$

$$I_{\eta,s} : \quad \mathcal{S}(s\eta + \eta^{\perp}; S^2\eta_{\mathbb{C}}^{\perp}) \to \mathcal{S}(T\mathbb{S}_{\eta}^{1}) \tag{3.8}$$

by the following formulae

$$I_{\eta,s}f(\xi,x) \quad = \textstyle\int_{-\infty}^{\infty} f(s\eta + x + t\xi)\cdot\xi \ \mathrm{d}t, \tag{3.9}$$

$$I_{\eta,s}f(\xi,x) \ = \textstyle\int_{-\infty}^{\infty}(f(s\eta + x + t\xi)\cdot\xi)\cdot\xi \,\mathrm{d}t \tag{3.10}$$

respectively. One can see that operators (3.6) and (3.10) are related. Indeed, if $f\in\mathcal{S}(\mathbb{R}^3; S^2\mathbb{C}^3)$ and $\iota^*_{\eta,s}f$ is the slice of f by the plane $s\eta+\eta^\perp$, then $I_{\eta,s}(\iota^*_{\eta,s}f)(\xi,x) = If(\xi, s\eta+x),$ for $(\xi,x)\in T\mathbb{S}^1_\eta$. Suppose we have a vector field $f\in\mathcal{S}(\mathbb{R}^3,\mathbb{C}^3)$ which can be uniquely represented as

$$f = {}^s f + \nabla v, \tag{3.11}$$

where ${}^s f\in C^\infty(\mathbb{R}^3,\mathbb{C}^3)$ such that

$$\nabla\cdot{}^s f = \sum_{j=1}^{3}\frac{\partial^s f_j}{\partial x_j} = 0 \tag{3.12}$$

and a scalar function $v\in C^\infty(\mathbb{R}^3)$ satisfying $v(x)\to 0$ as $|x|\to\infty$. The field ${}^s f$ is called the *solenoidal part* of the vector field f, whilst ∇v is known as the *potential part* of f. The LRT of a potential field is identically equal to zero: $I(\nabla v) = 0$, for any $v\in C^1(\mathbb{R}^3)$ satisfying $v(x)\to 0$ as $|x|\to\infty$. Thus we can only hope to recover the solenoidal part. Similarly consider a tensor field $g\in\mathcal{S}(\mathbb{R}^3, S^2\mathbb{C}^3)$ which can also be uniquely represented as

$$g_{jk} = {}^s g_{jk} + \frac{1}{2}\left(\frac{\partial u_j}{\partial x_k} + \frac{\partial u_k}{\partial x_j}\right), \tag{3.13}$$

with ${}^s g\in C^\infty(\mathbb{R}^3, S^2\mathbb{C}^3)$ satisfying

$$\sum_{k=1}^{3}\frac{\partial^s g_{jk}}{\partial x_k} = 0, \qquad (1\le j\le 3), \tag{3.14}$$

and a vector field $u\in C^\infty(\mathbb{R}^3;\mathbb{C}^3)$ satisfying $u(x)\to 0$ as $|x|\to\infty$. The field ${}^s g$ is called the *solenoidal part* of the tensor field g, whilst the term involving the partial derivatives in (3.13) is the *potential part* of g. The LRT of a potential field is identically equal to zero, i.e. $Ig = I^s g$. Sharafutdinov in [39] generalizes this unique splitting for rank m tensors of the form $h\in\mathcal{S}(\mathbb{R}^3; S^m\mathbb{C}^3)$.

Complete Inversion of LRT

In Section 2.3.1 we derive the inversion formula for the Radon transform which can be stated in terms of the Laplacian as follows

$$f = c_n(-\Delta)^{\frac{n-1}{2}} R^\sharp Rf, \tag{3.15}$$

where $c_n = (4\pi)^{\left(\frac{n-1}{2}\right)} \frac{\Gamma\left(\frac{n}{2}\right)}{\Gamma\left(\frac{1}{2}\right)}$ and the Laplacian operator denoted as Δ acts on components and it's inverse Δ^{-1} is defined by convolution with the fundamental solution. This should motivate us to ask ourselves if such an inversion procedure exists for the LRT. We closely follow the notation of Sharafutdinov [39] for the next few sections and indeed this is possible by Theorem 2.12.2 of [39, Chapter 2], which requires some definitions.

Definition 3.3 *The backprojection operator* $\mathcal{B} \; : \; \mathcal{S}(\mathbb{R}^3 \times \mathbb{R}^3_0; S^2\mathbb{R}^3) \to \mathcal{S}(\mathbb{R}^3; S^2\mathbb{R}^3)$ *is given by*

$$\mathcal{B}\phi(x) = \frac{1}{4\pi} \int_\Omega \phi(x, \xi) \; d\omega(\xi), \tag{3.16}$$

where $\Omega \subseteq \mathbb{R}^3$ *is the unit sphere and* ω *is its standard measure.*

Definition 3.4 *On* $\mathcal{S}(\mathbb{R}^3; S^k\mathbb{R}^3)$, *the space of smooth symmetric rank* k *tensor fields, we define the generalization of divergence* $\delta \; : \; \mathcal{S}(\mathbb{R}^3; S^k\mathbb{R}^3) \to \mathcal{S}(\mathbb{R}^3; S^{k-1}\mathbb{R}^3)$ *by*

$$(\delta f)_{i_1.....i_{k-1}} = \frac{\partial}{\partial x_j} f_{i_1.....i_{k-1}j}. \tag{3.17}$$

We will repeatedly use Einstein summation convention from now. Furthermore, the negative of its formal adjoint is explained hereunder.

Definition 3.5 *The symmetric derivative* $d \; : \; \mathcal{S}(\mathbb{R}^3; S^k\mathbb{R}^3) \to \mathcal{S}(\mathbb{R}^3; S^{k+1}\mathbb{R}^3)$ *is given by*

$$(df)_{i_1.....i_{k+1}} = \sigma\left(\frac{\partial}{\partial x_{i_{k+1}}} f_{i_1.....i_k}\right), \tag{3.18}$$

where σ *is the symmetrization operator on tensors.*

We are now ready to state the theorem.

Theorem 3.2 *Let $n = 3$ and $m = 0, 1$ and 2. For every tensor field $f \in \mathcal{S}(\mathbb{R}^3; S^2\mathbb{R}^3)$, the solenoidal part of f can be recovered from the LRT, If, according to the formula*

$$^s f = (-\Delta)^{1/2} \left[\sum_{k=0}^{[m/2]} c_k (i - \Delta^{-1} d^2)^k j^k \right] \Phi^m I f, \tag{3.19}$$

where $\Phi^m : \mathcal{S}(\mathbb{R}^3; S^m\mathbb{R}^3) \to \mathcal{S}(\mathbb{R}^3; S^m\mathbb{R}^3)$ is the operator sending a function $\psi(x, \xi)$ to the set of its integral moments with respect to its second argument. Specifically this is

$$(\Phi^m \psi)_{i_1 \ldots . i_m}(x) = \frac{1}{4\pi} \int_\Omega \xi_{i_1} \ldots \xi_{i_m} \psi(\xi, x)\ d\omega(\xi). \tag{3.20}$$

In Theorem 3.2 i and j are the operators defined by the equalities $iu = \mathbf{I}u$, $ju = \text{tr}\ u$. Here i is the operator of symmetric multiplication by the Kronecker tensor, δ_{ij} and j is the operator of convolution with δ_{ij}. Note that $j : (\mathbb{C}^3; S^{m+2}\mathbb{C}^3) \to (\mathbb{C}^3; S^m\mathbb{C}^3)$ (i.e. lowers the rank of the tensor by 2). The coefficients c_k are given by the formula

$$c_k = (-1)^k \frac{1}{\pi} \frac{(2m - 2k)!!}{2^k k!(m - 2k)!} \tag{3.21}$$

and $[m/2]$ is the integer part of $m/2$.

Proof. See [39, Chapter 2] $\square$.

Now we derive some formulae for the Fourier transforms of the integral moment operator in (3.20) for $m = 0, 1$ and 2. Using the substitution $x' = x + t\xi$ and the symmetry in t we achieve

$$(\Phi^m I f)_{i_1 i_2} = \frac{1}{2\pi} \int_\Omega \xi_{i_1} \xi_{i_2} \int_0^\infty f_{j_1 j_2}(x + t\xi) \xi_{j_1} \xi_{j_2}\ dt\ d\omega(\xi) \tag{3.22}$$

$$= \frac{1}{2\pi} \int_\Omega \int_0^\infty \frac{(x' - x)_{i_1} (x' - x)_{i_2}}{|x' - x|^m} f_{j_1 j_2}(x') \frac{(x' - x)_{j_1} (x' - x)_{j_2}}{|x' - x|^{m+2}} t^2\ dt\ d\omega(\xi). \tag{3.23}$$

By the use of Appendix A we know integrals over $\mathbb{R}^n$ can be expressed as integrals over spheres. Thus we recognise (3.23) as

$$(\Phi^m I f)_{i_1 i_2} = \frac{1}{2\pi} \int_{\mathbb{R}^3} \frac{(x' - x)_{i_1} (x' - x)_{i_2}}{|x' - x|^m} f_{j_1 j_2}(x') \frac{(x' - x)_{j_1} (x' - x)_{j_2}}{|x' - x|^{m+2}}\ dx'. \tag{3.24}$$

Hence by the definition of convolution (3.24) can be rewritten as

$$(\Phi^m I f)_{i_1 i_2} = \frac{1}{2\pi} f_{j_1 j_2} * \frac{x_{i_1} x_{i_2} x_{j_1} x_{j_2}}{|x|^{2m+2}}. \tag{3.25}$$

To apply the Fourier transform to (3.25), we require some justification. Note that $f_{j_1 j_m} \in \mathcal{S}$ and the fraction can be regarded as an element of the space of tempered distributions, $\mathcal{S}'$. As convolution is just multiplication in Fourier space, i.e. $\widehat{(f * g)} = (2\pi)^{n/2}\hat{f}\hat{g}$. This suggests

$$F[(\Phi^m If)_{i_1 i_2}] = \sqrt{2\pi}\hat{f}_{j_1 j_2} F\left[\frac{x_{i_1} x_{i_2} x_{j_1} x_{j_2}}{|x|^{2m+2}}\right], \tag{3.26}$$

which is the result giving the inversion for the x-ray transfrom in three dimensions (2.34), with $\alpha = 1$. In terms of the Laplacian this is just $f = (-\Delta)^{1/2} X^{\sharp} X f$. In accordance with the usual rules of treating the Fourier transform like those present in [18], we can write (3.26) as

$$F[(\Phi^m If)_{i_1 i_2}] = (-1)^m \frac{\sqrt{\pi}}{2^{2m}} \frac{\Gamma\left(-m + \frac{1}{2}\right)}{\Gamma\left(m+1\right)} \hat{f}_{j_1 j_2} \partial_{i_1 i_2 j_1 j_2} |y|^{2m-1}, \tag{3.27}$$

where $\partial_{i_1 \dots i_k} = \frac{\partial^k}{\partial y_{i_1} \dots \partial y_{i_k}} (k = 0, 1, \text{ or } 2)$. Now we state the following lemma from [39, Lemma 2.11.1].

Lemma 3.1 *For an integer $m \geq 0$,*

$$\partial^{2m} |y|^{2m-1} = ((2m-1)!!)^2 |y|^{-1} \Pi_y^m,$$

where Π_y^m is the m'th power of the function $\left(\delta_{ij}(y) - \frac{y_i y_j}{|y|^2}\right)$ and $k!! = k(k-2)(k-4)...$ noting that $(-1)!! = 1$. Equivalently one can understand the above as

$$\partial_{i_1 \dots i_{2m}} |y|^{2m-1} = ((2m-1)!!)^2 |y|^{-1} \sigma(\Pi_{i_1 i_2 \dots i_{2m-1} i_{2m}})$$

where σ has been defined earlier in (3.18) as the symmetrization operator.

Upon using Lemma 3.1 we can show that (3.27) can be written as

$$\widehat{\Phi^m If}(y) = b(m,3) |y|^{-1} \Pi_y^m \hat{f}(y), \quad \text{where} \tag{3.28}$$

$$b(m,3) = (-1)^m \sqrt{\pi} \frac{((2m-1)!!)^2}{2^{2m}} \frac{\Gamma\left(-m + \frac{1}{2}\right)}{\Gamma\left(m+1\right)} \tag{3.29}$$

is just a constant and Φ^m can be thought of as the integral moment backprojection operator. Now for different values of $m = 0, 1$ or 2, we immediately have

$$\widehat{\Phi^0 If}(y) = \hat{f}(y) \frac{\pi}{|y|} \tag{3.30}$$

and for a vector field, f, when $m = 1$,

$$\widehat{\Phi^1 If}(y) = \Pi_y \hat{f}(y) \frac{\pi}{2|y|}. \tag{3.31}$$

Using the calculated value $b(2,3) = \frac{3\pi}{8|y|}$, we see

$$\widehat{\Phi^2 If}(y) = \widetilde{\Pi}_y(\hat{f}(y)) \frac{3\pi}{8|y|}. \tag{3.32}$$

In (3.32) above, $\widetilde{\Pi}_y = \Pi_y^2$. Specifically this operator can be calculated as

$$\widetilde{\Pi}_y(\hat{f}(y)) = \frac{2}{3} \Pi_y \hat{f}(y) \Pi_y + \frac{1}{3} \mathrm{tr}(\Pi_y \hat{f}(y)) \Pi_y. \tag{3.33}$$

Now consider from (3.21) that $c_{0,m=0} = \frac{1}{\pi}, c_{0,m=1} = \frac{2}{\pi}, c_{0,m=2} = \frac{4}{\pi}$ and $c_{1,m=2} = -\frac{1}{\pi}$. Hence substituting these values into (3.19) of Theorem 3.2 gives

$$f = \frac{4}{\pi} \left[\frac{7}{4} \mathbf{I} - \frac{1}{4} \mathbf{I} \ \mathrm{tr} + \frac{1}{4} \Delta^{-1} d^2 \ \mathrm{tr} \right] (-\Delta)^{1/2} \mathcal{B} If. \tag{3.34}$$

3.2.2 The Transverse Ray Transform

For the LRT we integrate along the ray direction, ξ. Suppose we integrate normal to the ray direction, ξ, in which case we define the Transverse Ray Transform (TRT) of symmetric rank two tensor fields

$$J : \mathcal{S}(\mathbb{R}^3; S^2\mathbb{C}^3) \to \mathcal{S}(T\mathbb{S}^2; S^2\mathbb{C}^3),$$

which is defined by

$$Jf(\xi, x) = \int_{-\infty}^{\infty} P_\xi f(x + t\xi) \, \mathrm{d}t, \tag{3.35}$$

where

$$P_\xi f = \Pi_\xi f \Pi_\xi, \quad \text{and} \quad \Pi_\xi = \delta - \frac{1}{|\xi|^2} \xi \otimes \xi,$$

is the projection of f onto the subspace orthogonal to ξ, that is to the set $\{f \in S^2\mathbb{C}^3 \mid f \cdot \xi = 0\}$ and δ is the Kronecker tensor. Note that here $P_\xi : S^2\mathbb{C}^3 \to S^2\mathbb{C}^3$. For example, for an orthonormal basis of the form $(e_1, e_2, e_3 = \xi)$, the projection $P_\xi f$ is expressed in components as

$$\begin{pmatrix} f_{11} & f_{12} & 0 \\ f_{12} & f_{22} & 0 \\ 0 & 0 & 0 \end{pmatrix}. \tag{3.36}$$

Moreover the TRT is defined for vector fields

$$J : \mathcal{S}(\mathbb{R}^3; \mathbb{C}^3) \to \mathcal{S}(T\mathbb{S}^2, \mathbb{C}^3),$$

by

$$Jf(\xi, x) = \int_{-\infty}^{\infty} \Pi_\xi f(x + t\xi)\, \mathrm{d}t. \tag{3.37}$$

Complete Inversion of TRT

Indeed an explicit inversion formula using complete data for the ray transform exists and is present in [27, Thm 8.1] using the ideas present in [39]. We reiterate the sketch of the proof here. By expanding $P_\xi f$ in (3.35) we see

$$P_\xi f = f - \frac{\xi\xi^T f + f\xi\xi^T}{|\xi|^2} + \frac{(\xi^T f \xi)\xi\xi^T}{|\xi|^4}. \tag{3.38}$$

Consider the expansion

$$\mathcal{B}Jf = G_1 f + G_2 f + G_3 f, \tag{3.39}$$

where the terms correspond to the three terms in (3.38). Quite simply using (3.25), G_1 is just $\mathcal{B}X$, implying

$$G_1 f = \frac{1}{2\pi} f * |x|^{-2} \tag{3.40}$$

and the third term is exactly $\Phi^2 f$, hence

$$(G_3 f)_{ij} = \frac{1}{2\pi} f_{kl} * \frac{x_i x_j x_k x_l}{|x|^6}. \tag{3.41}$$

If one looks at (3.24) for $m = 1$, applying this to $f_{ip}\xi_p$, gives

$$(G_2 f)_{ij} = -\frac{1}{2\pi}\left(f_{ik} * \frac{x_j x_k}{|x|^4} + f_{jk} * \frac{x_i x_k}{|x|^4} \right). \tag{3.42}$$

Finally if we take the Fourier transforms of these expression we yield Lemma 3.2, stated below.

Lemma 3.2 *Let* $g = \frac{2}{\pi}\mathcal{B}Jf$, *then*

$$|y|\hat{g} = \hat{f} - \frac{1}{2}(\Pi_y \hat{f} + \hat{f}\Pi_y) + \frac{3}{8}\widetilde{\Pi}_y(\hat{f}). \tag{3.43}$$

Now let $z = \frac{y}{|y|}$ which makes $\Pi_y = \mathbf{I} - zz^T$. Our first job is to transform $\widetilde{\Pi}_y$ in terms of Π_y. Thus consider

$$\widetilde{\Pi}_y \hat{f} = \frac{2}{3}\Pi_y \hat{f}(y)\Pi_y + \frac{1}{3}\mathrm{tr}(\Pi_y \hat{f})\Pi_y$$

$$= \frac{2}{3}[\mathbf{I} - zz^T]\hat{f}[\mathbf{I} - zz^T] + \frac{1}{3}\mathrm{tr}[(\mathbf{I} - zz^T)\hat{f}](\mathbf{I} - zz^T)$$

$$= \frac{2}{3}\hat{f} - \frac{2}{3}(\hat{f}zz^T + zz^T\hat{f}) + \frac{2}{3}(z^T\hat{f}z)zz^T - \frac{1}{3}\mathrm{tr}(zz^T\hat{f})\mathbf{I} + \frac{1}{3}\mathrm{tr}(zz^T\hat{f})zz^T$$

$$+\frac{1}{3}\mathrm{tr}(\hat{f})\mathbf{I} - \frac{1}{3}\mathrm{tr}(\hat{f})zz^T. \tag{3.44}$$

Using the result $\mathrm{tr}(AB) = \mathrm{tr}(BA)$, we can simplify (3.44) to

$$\widetilde{\Pi}_y \hat{f} = \frac{2}{3}\hat{f} + \frac{1}{3}\mathrm{tr}(\hat{f})\mathbf{I} - \frac{2}{3}(\hat{f}zz^T + zz^T\hat{f}) + (z^T\hat{f}z)zz^T - \frac{1}{3}\mathrm{tr}(\hat{f})zz^T - \frac{1}{3}(z^T\hat{f}z)\mathbf{I}. \tag{3.45}$$

Upon substitution of (3.45) in (3.43) we achieve

$$|y|\hat{g} = \frac{1}{4}\hat{f} + \frac{1}{4}(zz^T\hat{f} + \hat{f}zz^T) + \frac{3}{8}(z^T\hat{f}z)zz^T + \frac{1}{8}\mathbf{I}\mathrm{tr}\hat{f} - \frac{1}{8}zz^T\mathrm{tr}\hat{f} - \frac{1}{8}z^T\hat{f}z\mathbf{I}. \tag{3.46}$$

By direct substitution we get

$$\hat{f} = \frac{1}{|y|}\left(4\hat{g} - 2(zz^T\hat{g} + \hat{g}zz^T) - \mathbf{I}\mathrm{tr}\hat{g} - zz^T\mathrm{tr}\hat{g} + (z^T\hat{g}z)\mathbf{I}\right). \tag{3.47}$$

To check that (3.47) is correct we can substitute it into (3.46). Now using the definition of d and δ leads us to Theorem 3.3

Theorem 3.3 *Let $f \in \mathcal{S}(\mathbb{R}^3; S^2\mathbb{C}^3)$ be a rank two symmetric tensor field, then*

$$f = \frac{4}{\pi}\left(4\mathbf{I} - \mathbf{I}\mathrm{tr} + 4\Delta^{-1}d\delta - \Delta^{-1}d^2\mathrm{tr} - \Delta^{-1}\mathbf{I}\delta^2\right)(-\Delta)^{1/2}\mathcal{B}Jf. \tag{3.48}$$

3.2.3 The Truncated Transverse Ray Transform

The Truncated Transverse Ray Transform (TTRT) is defined to be the linear operator

$$K : \mathcal{S}(\mathbb{R}^3; S^2\mathbb{C}^3) \to \mathcal{S}(T\mathbb{S}^2; S^2\mathbb{C}^3) \quad \text{such that}$$

$$Kf(\xi, x) = \int_{-\infty}^{\infty} Q_\xi f(x + t\xi)\, dt. \tag{3.49}$$

For a unit vector ξ, we define $Q_\xi : S^2\mathbb{C}^3 \to S^2\mathbb{C}^3$ to be the orthogonal projection onto the subspace $\{f \in S^2\mathbb{C}^3 \mid f \cdot \xi = 0, \mathrm{tr} f = \sum_{j=1}^3 f_{jj} = 0\}$. To illustrate this, let us take the orthonormal basis $(e_1, e_2, e_3 = \xi)$ and the projection can be expressed by

$$Q_\xi f = \frac{1}{2}\begin{pmatrix} f_{11} - f_{22} & 2f_{12} & 0 \\ 2f_{12} & f_{22} - f_{11} & 0 \\ 0 & 0 & 0 \end{pmatrix}. \tag{3.50}$$

One may think of Q_ξ as

$$Q_\xi f = P_\xi f - \frac{1}{2}\mathrm{tr}(P_\xi f)\Pi_\xi. \tag{3.51}$$

This is precisely the projection of f onto $\xi^\perp$ followed by the projection onto the kernel of the trace operator on $\xi^\perp$.

Complete Inversion of TTRT

Expanding (3.51) gives

$$Q_\xi f = f - \frac{1}{2}\mathrm{tr} f\mathbf{I} - \frac{1}{|\xi|^2}(\xi\xi^T f + f\xi\xi^T) + \frac{1}{2|\xi|^4}(\xi^T f\xi)\mathbf{I} + \mathrm{tr} f\frac{1}{2|\xi|^2}\xi\xi^T. \tag{3.52}$$

If we follow the procedure for the TRT, then suppose the backprojection operator for the TTRT is

$$\mathcal{B}Kf = G_1 f + G_2 f + \frac{1}{2}G_3 f + G_4 f,$$

where G_1, G_2, G_3 have been identified earlier in Section 3.2.2. For $G_4 f$ consider

$$(G_4 f)_{ij} = \frac{1}{4\pi} f_{kl} * \frac{x_k x_l}{|x|^4}\delta_{ij}. \tag{3.53}$$

Once again taking the Fourier transform of each of the now four terms gives us Lemma 3.3.

Lemma 3.3 *Let* $h = \frac{2}{\pi}\mathcal{B}Kf$ *then*

$$|y|\hat{h} = \hat{f} - \frac{1}{2}\left(\Pi_y \hat{f} + \hat{f}\Pi_y\right) + \frac{3}{16}\widetilde{\Pi}_y(\hat{f}) + \frac{1}{4}\mathrm{tr}(\Pi_y \hat{f})\mathbf{I}. \tag{3.54}$$

Now substituting (3.45) into (3.54) assuming $\mathrm{tr} f = 0$ gives

$$|y|\hat{h} = \frac{1}{8}\hat{f} + \frac{3}{8}(zz^T\hat{f} + \hat{f}zz^T) + \frac{3}{16}(z^T\hat{f}z)zz^T - \frac{5}{16}(z^T\hat{f}z)\mathbf{I}. \tag{3.55}$$

By direct substitution we show that

$$\hat{f} = \frac{2}{|y|}\left(4\hat{h} - 3(zz^T\hat{h} + \hat{h}zz^T) + (z^T\hat{h}z)zz^T + \frac{5}{3}(z^T\hat{h}z)\mathbf{I}\right). \tag{3.56}$$

From the definition of d and δ we can invert the TTRT using complete data which is stated in Theorem 3.4.

Theorem 3.4 *Suppose* $f, \tilde{f} \in \mathcal{S}(\mathbb{R}^3; S^2\mathbb{C}^3)$. *Here* $f = \tilde{f} + a\mathbf{I}$ *where* $a \in \mathcal{S}(\mathbb{R}^3)$ *and* $\mathrm{tr}\tilde{f} = 0$, *then*

$$\tilde{f} = \frac{4}{\pi}\left(4\mathbf{I} - 6\Delta^{-1}d\delta + \Delta^2 d^2\delta^2 + \frac{5}{3}\mathbf{I}\Delta^{-1}\delta^2\right)(-\Delta)^{1/2}\mathcal{B}Kf. \tag{3.57}$$

It is important to note that the operator K vanishes on scalar multiples of the Kronecker tensor.

3.2.4 SVD and stability estimates

Just to state ongoing work in this area as far as range conditions and stability is concerned, the author wants to outline the work of Sharafutdinov, [40] and [38]. Here it is attempted to derive some stability estimates in a similar method to Natterer in [31] which are stated in Section 2.5. As plane-by-plane data is written in terms of scalar, vector and tensor longitudinal ray transforms, the ranges of these operators can be determined in the plane case as a singular function expansion in a suitable Hilbert space. A similar technique was employed to calculate the singular value decomposition for the Radon transform in Section 2.4. In fan beam coordinates the singular value decomposition of the ray transform is given by [23]. Moreover [8] and [9] consider a parallel beam formulation.

The Helgason-Ludwig range conditions mentioned in Theorem 2.1, for the scalar Radon transform in the plane simply states that the kth moment of the data

$$\int_{-\infty}^{\infty} p^k Xf(\xi, p\xi^\perp)\,\mathrm{d}p,$$

is a polynomial of degree $\leq k$ in ξ. For the LRT of a rank m tensor the condition is simply degree $\leq k + m$. A deeper connection between these conditions and the singular function expansion is given by [30]. Such consistency conditions, characterizing the range of the forward operator are of great assistance in diagnosing errors and unaccounted physical effects in experimental data. These were studied in order to recognise the issues outlined in Section 5.6.

3.3 Relations Between Transforms

The discussion for TRT and TTRT will be combined together from this point onwards unless it is stated specifically. For a given rotation axis η and direction $\xi \in \eta^\perp$, there are two types of components that need considering. Generally $\tilde{f}$ denotes a trace free symmetric rank two tensor field. The 'axial' component for the TRT and TTRT is $[\eta \cdot (Jf(\xi, x) \cdot \eta)]$ and $[\eta \cdot (K\tilde{f}(\xi, x) \cdot \eta)]$. On the other hand the 'non-axial' components are given by $[\zeta \cdot (Jf(\xi, x) \cdot \eta)]$ and $[\zeta \cdot (K\tilde{f}(\xi, x) \cdot \eta)]$ where $\zeta = \xi \times \eta$ ($\times$ is the vector product). Moreover we have the components $[\zeta \cdot (Jf(\xi, x) \cdot \zeta)]$ and $[\zeta \cdot (K\tilde{f}(\xi, x) \cdot \zeta)]$. Note that $[\zeta \cdot (K\tilde{f}(\xi, x) \cdot \zeta)]$ will give us no new information since the operator Q_ξ acts on trace free tensor fields in this study. Hence we omit the discussion for this.

We require the non-axial components of $Jf(\xi, x)$, in terms of LRT's on transaxial planes. The 'off diagonal' components can be expressed as

$$((Jf)(\xi, x) \cdot \eta) \cdot (\xi \times \eta) = \int_{-\infty}^{\infty} (\Pi_\xi f(x + t\xi) \Pi_\xi \cdot \eta) \cdot (\xi \times \eta) \, \mathrm{d}t$$

$$= \int_{-\infty}^{\infty} (f(x + t\xi) \cdot \eta) \cdot (\xi \times \eta) \, \mathrm{d}t = \int_{-\infty}^{\infty} [\eta \times (f(x + t\xi) \cdot \eta)] \cdot \xi \, \mathrm{d}t.$$

Note that the projections $P_\xi \tilde{f}$ and $Q_\xi \tilde{f}$ are related by

$$Q_\xi \tilde{f}(x) = P_\xi \tilde{f}(x) + \frac{1}{2}[(\tilde{f}(x) \cdot \xi) \cdot \xi] \cdot \Pi_\xi, \tag{3.58}$$

Now setting $x := x + t\xi$ and integrating the result over t gives

$$K\tilde{f}(\xi, x) = J\tilde{f}(\xi, x) + \frac{1}{2}[(I\tilde{f})(\xi, x)] \cdot \Pi_\xi. \tag{3.59}$$

Next consider $\Pi_\xi \cdot \eta = \eta$ and the scalar product of (3.59) is taken with η, we achieve

$$K\tilde{f}(\xi, x) \cdot \eta = J\tilde{f}(\xi, x) \cdot \eta + \frac{1}{2}(I\tilde{f})(\xi, x)\eta. \tag{3.60}$$

Now taking the scalar product with ζ gives

$$((K\tilde{f})(\xi, x) \cdot \eta) \cdot \zeta = [((J\tilde{f})(\xi, x) \cdot \eta) \cdot \zeta] + \frac{1}{2}[((I\tilde{f})(\xi, x)\eta) \cdot \zeta]$$

$$= ((J\tilde{f})(\xi, x) \cdot \eta) \cdot \zeta, \tag{3.61}$$

since $\eta \times (\xi \times \eta) = 0$. Since the vector field $\eta \times (f \cdot \eta)$ is orthogonal to η, its restriction to every plane $s\eta + \eta^{\perp}$ can be considered as a vector field on the plane, i.e. $(\eta \times (f \cdot \eta))|_{s\eta+\eta^{\perp}} \in \mathcal{S}(s\eta + \eta^{\perp}; \eta^{\perp}_{\mathbb{C}})$ where $\eta^{\perp}_{\mathbb{C}}$ is the complexification of η. As this is then contracted with the ray direction, ξ, we have

$$I_{\eta,s}((\eta \times (f \cdot \eta))|_{s\eta+\eta^{\perp}})(\xi, x) = ((Jf)(\xi, x) \cdot \eta) \cdot (\xi \times \eta) \quad \text{for} \quad (\xi, x) \in T\mathbb{S}^1_{\eta}. \tag{3.62}$$

On the other hand we consider the axial component of the TTRT by taking the scalar product of (3.60) with η giving

$$((K\tilde{f})(\xi, x) \cdot \eta) \cdot \eta = [((J\tilde{f})(\xi, x) \cdot \eta) \cdot \eta] + \frac{1}{2}[((I\tilde{f})(\xi, x)\eta) \cdot \eta]. \tag{3.63}$$

Now by defining the function ϕ on the plane $s\eta + \eta^{\perp}$ by $\phi(x) = (f(x) \cdot \eta) \cdot \eta$ it can be shown that

$$I_{\eta,s}(\iota^*_{\eta,s}\tilde{f} + 2\phi\delta)(\xi, x) = 2((K\tilde{f})(\xi, s\eta + x) \cdot \eta) \cdot \eta, \tag{3.64}$$

where δ is the kronecker tensor on $\xi^{\perp}$ and $\iota^*_{\eta,s}\tilde{f}$ is the slice of $\tilde{f}$ by the plane $s\eta + \eta^{\perp}$. Now let (ξ, ζ, η) be an orthonormal basis of $\mathbb{R}^3$ and using the fact that

$$0 = \mathrm{tr}\tilde{f}(x) = [(\tilde{f}(x) \cdot \xi) \cdot \xi] + [(\tilde{f}(x) \cdot \zeta) \cdot \zeta] + [(\tilde{f}(x) \cdot \eta) \cdot \eta]$$

$$\text{and} \quad \mathrm{tr}\iota^*_{\eta,s}\tilde{f}(x) = [(\tilde{f}(x) \cdot \xi) \cdot \xi] + [(\tilde{f}(x) \cdot \zeta) \cdot \zeta] \quad \text{for} \quad x \in s\eta + \eta^{\perp}.$$

Hence we have an equality for $\phi(x)$ which is precisely

$$\phi(x) = -\mathrm{tr}\iota^*_{\eta,s}\tilde{f}(x). \tag{3.65}$$

Substituting this value into (3.64), we obtain

$$I_{\eta,s}(\iota^*_{\eta,s}\tilde{f} - 2(\mathrm{tr}\iota^*_{\eta,s}\tilde{f})\delta)(\xi, x) = 2((K\tilde{f})(\xi, s\eta + x) \cdot \eta) \cdot \eta. \tag{3.66}$$

As we have seen in (3.36), the TRT depends only on the projection normal to the direction of the ray. Without loss of generality, take $e_3 = \eta = (0, 0, 1)$ and parameterize ξ in the usual sense as

$$\xi = \begin{pmatrix} \cos\theta \\ \sin\theta \\ 0 \end{pmatrix}, \quad \text{so,} \quad \zeta = \begin{pmatrix} -\sin\theta \\ \cos\theta \\ 0 \end{pmatrix}.$$

Since $\zeta \in \xi^\perp$ we can calculate

$$\begin{aligned}
\zeta \cdot (f \cdot \zeta) &= (-\sin\theta, \cos\theta, 0)\begin{pmatrix} f_{11} & f_{12} & 0 \\ f_{12} & f_{22} & 0 \\ 0 & 0 & 0 \end{pmatrix}\begin{pmatrix} -\sin\theta \\ \cos\theta \\ 0 \end{pmatrix} \\
&= f_{22}\cos^2\theta - 2f_{12}\cos\theta\sin\theta + f_{11}\sin^2\theta \\
&= (\cos\theta, \sin\theta, 0)\begin{pmatrix} f_{22} & -f_{12} & 0 \\ -f_{12} & f_{11} & 0 \\ 0 & 0 & 0 \end{pmatrix}\begin{pmatrix} \cos\theta \\ \sin\theta \\ 0 \end{pmatrix} \\
&= \xi \mathrm{Adj}_{e_3^\perp}(f)\xi,
\end{aligned}$$

where $\mathrm{Adj}_{e_3^\perp}(f)$ denotes the adjugate matrix of the slice of f restricted to the plane; of course this is nothing other than the conjugation of $P_{e_3}f$ with a right angle rotation about the e_3 axis. Hence using the above, we see that for $\xi \in \eta^\perp$

$$(Jf(\xi, x) \cdot \zeta) \cdot \zeta = \int_{-\infty}^{\infty} (f(x + t\xi) \cdot \zeta) \cdot \zeta \ \mathrm{d}t \tag{3.67}$$

and

$$= \int_{-\infty}^{\infty} (\mathrm{Adj}_{\eta^\perp}(f)(x + t\xi) \cdot \xi) \cdot \xi = (I\mathrm{Adj}_{\eta^\perp}(f)(\xi, x) \cdot \xi) \cdot \xi, \tag{3.68}$$

which is the LRT transform of the two dimensional adjugate of the slice of f, restricted to the plane. We notice that this is exactly the transverse ray transform in the planar case. The results of this section can be summarized in the following Lemma:

Lemma 3.4 *Let $f, \tilde{f} \in \mathcal{S}(\mathbb{R}^3; S^2\mathbb{C}^3)$ where f is a symmetric tensor field and $\tilde{f}$ is a trace free symmetric tensor field. The equations*

$$I_{\eta,s}((\eta \times f\eta)|_{s\eta+\eta^\perp}) = (J^1_{\eta,s}f) = (K^1_{\eta,s}\tilde{f}), \tag{3.69}$$

$$I_{\eta,s}\left(\mathrm{Adj}_{\eta^\perp}(\iota^*_{\eta,s}f)\right) = (J^2_{\eta,s}f) \quad \textit{and} \tag{3.70}$$

$$I_{\eta,s}(\iota^*_{\eta,s}\tilde{f} - 2\mathrm{tr}(\iota^*_{\eta,s}\tilde{f})\delta) = 2K^2_{\eta,s}\tilde{f} \tag{3.71}$$

hold for every $s \in \mathbb{R}$ and $\eta \in \mathbb{S}^2$, where

$$(J^1_{\eta,s}f) = ((Jf)(\xi, s\eta + x) \cdot \eta) \cdot (\xi \times \eta), \quad (K^1_{\eta,s}\tilde{f}) = ((K\tilde{f})(\xi, s\eta + x) \cdot \eta) \cdot (\xi \times \eta)$$

$$(J^2_{\eta,s}f) = ((Jf)(\xi, s\eta + x) \cdot \zeta) \cdot \zeta \quad \textit{and} \quad (K^2_{\eta,s}\tilde{f}) = ((K\tilde{f})(\xi, s\eta + x) \cdot \eta) \cdot \eta.$$

Now that we have introduced several transforms and derived relations between them, we are ready to discuss certain applications associating the relevant transforms.

Chapter 4

Applications of Ray Transforms

The requirements of a postmodern society demands that we can visualize the inside of objects in a more sophisticated manner. Hence the design of experiments by scientists are producing exotic types of data giving rise to rich tomography problems. In this chapter we restrict our attention to three imaging modalities relating to the four transforms introduced in Chapter 3. In essence many ray transforms can be related to different types of rich tomography problems, continuously arising due to the needs of civilisation. For example, Sharafutdinov [39] introduces two ray transforms that are not mentioned here; Exponential and Mixed ray transforms. As is mentioned in his book, these arise in many important practical problems.

In Section 4.1 we introduce the PNMFT problem and describe the data acquisition process. Furthermore the linearized inverse problem is identified in Section 4.2 where we simulate and reconstruct PNMFT data. To finish off we derive the novel result which is contained in [37]. In Section 4.3 we introduce diffraction strain tomography [27], wherein it is illustrated that a certain moment of the data corresponds to the TRT. Currently, it is known how to reconstruct data from rotations about six axes [39, Sec 5.1.6] or complete data shown in Section 3.2.2. In Section 4.4, we give an outline of Photoelastic tomography and mention the advancements made to the code running on the apparatus now at Sheffield.

4.1 Polarimetric Neutron Magnetic Field Tomography

Despite being electrically neutral, neutrons carry a magnetic moment, which is coupled to their spin vector. For an ensemble of polarised neutrons in a magnetic field it can be shown that they behave like a particle with a classical magnetic moment. Therefore the spin vector, σ, satisfies

$$\frac{d}{dt}\sigma(t) = \gamma_N \sigma(t) \times B(t), \tag{4.1}$$

where $\gamma_N = -1.8324 \times 10^8 \text{ s}^{-1}\text{T}^{-1}$ is the gyro-magnetic ratio of the neutron.

Experimentally we assume a polarised neutron beam with uniform velocity set up at a spallation source. The beam size is approximately 4×4 cm^2. In this thesis we only consider monochromatic beams (single wavelength) and disregard beams with several velocities. Usually the range of velocities span in the region of 1.5 Å to 7 Å for which polarisations well beyond 90% and close to 100% can be achieved with spin filters like super mirror devices illustrated in [22, 7]. Throughout we assume spin precession is wavelength dependent, specifically 5 Å. A neutron spin filter only transmits neutrons with spin parallel to the magnetization of the device. Assuming the beam is not depolarized locally within the setup, a well defined final Larmor precession angle with respect to the analyzer's direction can be extracted modulo 2π.

One can understand the data acquisition process from Figure 4.1. Firstly, neutrons are polarised in the η-direction by the polariser and the two $\pi/2$ spin rotators downstream can be used to rotate the neutron spins to the ζ- or ξ-directions. The sample is rotated along a vertical axis for different tomographic projections, and the two following $\pi/2$ spin rotators choose the direction of analysis before the analyser, which transmits neutrons with spins along η. At the end, the signal is recorded by a position sensitive detector. Note that initial polarization and conservation in the setup without the sample is negligible. Between the polarising and analysing spin filter, including the sample position, the neutron beam has to be well guided throughout the magnetic field in order to maintain polarisation. Such a setup is already in place at JPARC (Tokai, Japan) [41]. Currently within Europe we do not have one although the ESS (Lund, Sweden) should have the apparatus by 2020. Naturally the trend will follow across the globe and we should see an increase in equipment capable of taking such recordings.

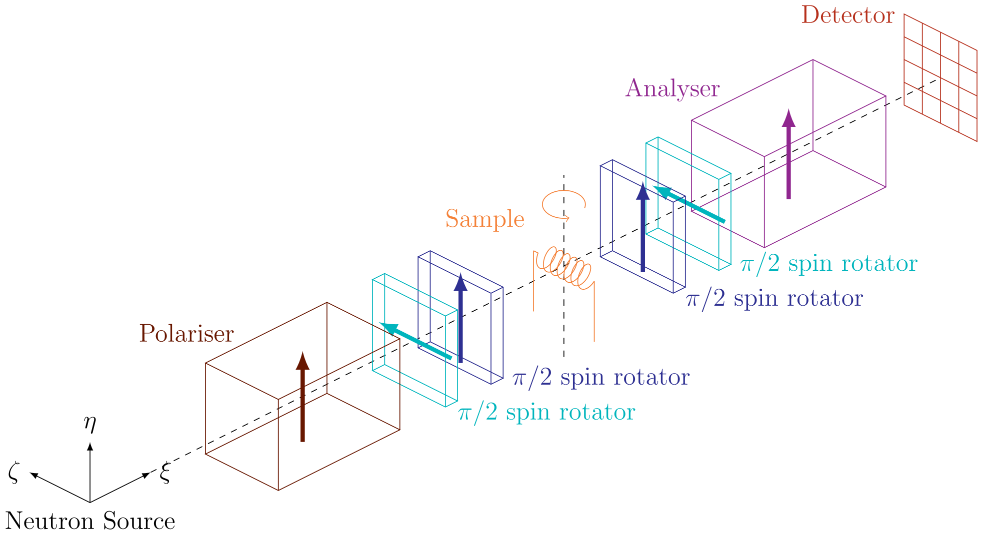

Figure 4.1: Experimental setup for data acquisition, credit to Morten Sales, [37].

In essence nine sinograms (3×3 matrix) are measured which represent three perpendicular incoming polarisation directions with all three directions for analysis which is explained thoroughly in [37]. Such measurements can only be recorded by the use of spin turners. Two flat coils situated before and after the sample turn the spin utilising Larmor precession by 90° in two perpendicular directions. By activating none, one or both spin flippers on either side of the sample will allow the measurement of the entire matrix. The recorded spin matrix is $SO(3)$ which generally puzzles mathematicians and physicists since the spin of neutrons is associated with $SU(2)$. In quantum mechanics, each Pauli matrix is related to an angular momentum operator that corresponds to an observable describing the spin of a spin $\frac{1}{2}$ particle, in each of the three spatial directions. The three Pauli matrices $\frac{\mathrm{i}}{2}\tau_1, \frac{\mathrm{i}}{2}\tau 2$ and $\frac{\mathrm{i}}{2}\tau 3$ form a basis for $\mathfrak{su}(2)$ which exponentiates to $SU(2)$, a double cover for $SO(3)$. Now $\frac{\mathrm{i}}{2}\tau_j$ are the generators of a projective representation (spin representation) of the rotation group $SO(3)$ acting on non-relativistic particles with spin $\frac{1}{2}$, like neutrons which are fermions.

An intriguing property of spin $\frac{1}{2}$ particles is that they must be rotated by an angle of 4π in order to return to their original configuration. This is due to the two-to-one correspondence between $SU(2)$ and $SO(3)$ and the way that, albeit one imagines spin up or down as the north or south pole on the 2-sphere S^2, they are actually represented by orthogonal vectors in the two dimensional complex Hilbert space. Hence, the states of the particles can be represented as two-component spinors or by 3×3 measurement matrices whose entries include the polarisation measurement in each direction. For an in-depth discussion, one can consult Section 1.4 of [15] or [13].

4.2 Linear Inverse Problem

A neutron is assumed to travel at uniform speed v in direction θ with position $x(t) = x(0) + t\xi$, $|\xi| = 1$ under the influence of an applied magnetic field, $B(x(t))$. The position-dependent behaviour of the spin vector described completely in [7] by

$$\frac{d\sigma(t)}{dt} = \gamma_N \sigma(t) \times B(x(t)), \tag{4.2}$$

where γ_N is the gyro-magnetic ratio of the neutron (-1.832×10^8 rad s^{-1} T^{-1}). Since our attention is on a single slice, we have in mind $x(t) = (\zeta, \eta, \xi)^T$ and $B(x(t)) = (B_1(x(t)), B_2(x(t)), B_3(x(t)))^T$ and $\sigma(t) = (\sigma_1(t), \sigma_2(t), \sigma_3(t))^T$. In contrast to many other vector and tensor tomography methods, the direction of travel ξ of the particle plays no role in its interaction with the quantity being imaged, here the magnetic field. Examples of tensor tomography where the direction of travel ξ does interact with the quantity being imaged will be seen later in Sections 4.3 and 4.4. The vector product $\sigma(t) \times B(x(t))$ is linear in $\sigma(t)$ and the matrix of this linear map is skew-symmetric; specifically we define

$$M(B(x(t))) = \gamma_N \begin{pmatrix} 0 & B_3(x(t)) & -B_2(x(t)) \\ -B_3(x(t)) & 0 & B_1(x(t)) \\ B_2(x(t)) & -B_1(x(t)) & 0 \end{pmatrix}.$$

Thus we can rewrite (4.2) as

$$\frac{d\sigma(t)}{dt} = M(B(x(t)))\sigma(t), \tag{4.3}$$

Along the path of this neutron we have a system of ordinary differential equations (4.3) which is linear but with variable coefficients. It plays a similar role to the Rytov-Sharafutdinov law in polarized light tomography [39]. Of course the differential equation cannot be solved simply using the integrating factor method that we would use for a scalar problem as in general the matrix $M(B(x(t)))$ does not commute with its derivative with respect to t. Our physical model assumes that there is no interaction between the direction of travel ξ and the effect of the magnetic field on the neutron. Hence armed with machinery from Section 3.1 in Chapter 3 we consider the case when $A_1 = A_2 = 0$ and let $A_0(x) = M(B(x))$. Our transport equation is then

$$\xi \cdot \nabla\Sigma(x, \xi) = M(B(x))\Sigma(x(t), \xi), \tag{4.4}$$

which is a reformulation of (4.3), but considers all straight line paths in the plane. Here $\Sigma = [\sigma_1(t)|\sigma_2(t)|\sigma_3(t)]$ is a matrix whose columns consist of three individual spin vectors, σ. We denote $S(M(B))$ to be the limit of $\Sigma(x + t\xi, \xi)$ when $t \to \infty$, for $t \in \mathbb{R}$. Note that $S(M(B))$ depends on $\Pi_\xi x$, where $\Pi_\xi x = x - (x \cdot \xi)\xi$. The matrix $S(M(B))(x, \xi)$ is our non-Abelian Radon transform of $M(B(x))$.

Gauge equivalence for $A_1 = A_2 = 0$ implies that $\partial g/\partial x_j = 0$ for $j = 1, 2$, which means that g must be constant and hence the identity. This means that for $A(x, \xi) = M(B(x))$ gauge equivalence is equality. We note that for ξ limited to the plane normal to some unit vector η, we can consider each plane $\mathit{\Pi}(\eta, s) = \{x : x \cdot \eta = s\}$ separately, where the reader should distinguish $\mathit{\Pi}$ as a plane and Π as the projection operator. Now Theorem 3.1 yields the following

Theorem 4.1 *Given a C^∞ vector field B with compact support in $\mathbb{R}^3$ for each plane $\mathit{\Pi}(\eta, p)$, the data $S(M(B))(x, \xi)$ for $x \in \mathit{\Pi}(\eta, s)$, $\eta \cdot \xi = 0$ uniquely determines $B_{\mathit{\Pi}(\eta,s)}$.*

Note that Eskin's proof of Theorem 3.1 reduces the reconstruction problem to a Riemann-Hilbert problem but currently this is not known to result in an explicit reconstruction algorithm.

We use compact support and assume that outside some ball Ω_R, the magnetic field B is zero. In reality the magnetic field only decays relatively close to zero as we always have a negligible field. Suppose the line $x + t\xi$ intersects Ω_R first at $t = t_-(x, \xi)$ and leaves for $t = t_+(x, \xi)$. Furthermore, let $C_c^\infty(\mathbb{R}^3 \times \mathbb{S}^2, \mathcal{M}_n(\mathbb{R}))$ be the space of functions on the unit sphere bundle in $\mathbb{R}^3$ into $n \times n$ matrices with real entries. Thus we realize $M(B) \in C_c^\infty(\mathbb{R}^3 \times \mathbb{S}^2, \mathcal{M}_3(\mathbb{R}))$ to be a smoothly compactly supported $\mathcal{M}_3(\mathbb{R})$ valued function on $\mathbb{R}^3 \times \mathbb{S}^2$. We also remind ourselves that oriented lines in $\mathbb{R}^2$ are points on the manifold $T\mathbb{S}^1$. Thus the forward map of PNMFT is then a mapping

$$\mathcal{F} : C_c^\infty(S\mathbb{R}^3, \mathcal{M}_3(\mathbb{R})) \to C^\infty(T\mathbb{S}^1)$$

defined by the unique solution $\Sigma \in C^\infty(\mathbb{R}^3 \times \mathbb{S}^2, \mathcal{M}_3(\mathbb{R}))$ of the transport equation

$$\xi \cdot \nabla \Sigma(x,\xi) = M(B(x))\Sigma(x(t),\xi), \qquad \lim_{t\to-\infty} \Sigma(x+t\xi,\xi) = I_3 \tag{4.5}$$

We understand this as

$$\mathcal{F}(M(B(x)) = \lim_{t\to\infty} \Sigma(x+t\xi,\xi) = S(M(B))(x,\xi)$$

and we require the linearization of this. Hence let us fix $x \in \mathbb{R}^3, \xi \in \mathbb{S}^2$, then by writing $\Sigma(t) = \Sigma(x+t\xi)$ and similarly for $M(B(x))$ which gives us the following

$$\frac{\mathrm{d}\Sigma}{\mathrm{d}t}(t) = M(B(t))\Sigma(t), \qquad \lim_{t\to-\infty} \Sigma(t) = I_3. \tag{4.6}$$

The Fréchet derivative $D\mathcal{F}(M(B^0))$ applied to a perturbation $M(\delta B) \in C_c^\infty(\mathbb{R}^3 \times \mathbb{S}^2, \mathcal{M}_3(\mathbb{R}))$ can be calculated in the following way. First suppose that Σ_0 is the solution of (4.5) with $M(B^0)$ and we let $\delta\Sigma \in C^\infty(\mathbb{R}^3 \times \mathbb{S}^2, \mathcal{M}_3(\mathbb{R}))$ be the solution of the following transport equation

$$\begin{gathered}\xi \cdot \nabla \delta\Sigma(x,\xi) - M(B^0(x))\delta\Sigma(x,\xi) = M(\delta B(x))\Sigma_0(x,\xi), \\ \lim_{t\to-\infty} \delta\Sigma(x+t\xi,\xi) = 0.\end{gathered} \tag{4.7}$$

Then

$$D\mathcal{F}(M(B^0))M(\delta B) = \lim_{t\to\infty} \delta\Sigma(x+t\xi,\xi).$$

Again if we fix x and ξ, then (4.7) can be written as

$$\frac{\mathrm{d}\delta\Sigma}{\mathrm{d}t}(t) - M(B^0(t))\delta\Sigma(t) = M(\delta B(t))\Sigma_0(t), \qquad \lim_{t\to-\infty} \delta\Sigma(t) = 0. \tag{4.8}$$

To solve (4.7) we introduce the integrating factor $S_0 \in C^\infty(\mathbb{R}^3 \times \mathbb{S}^2, \mathcal{M}_3(\mathbb{R}))$ which satisfies

$$\xi \cdot \nabla S_0(x,\xi) = S_0(x,\xi)M(B^0(x)), \qquad \lim_{t\to\infty} S_0(x+t\xi,\xi) = I_3. \tag{4.9}$$

By employing the integrating factor we can rewrite (4.8) as

$$\frac{\mathrm{d}}{\mathrm{d}t}(S_0(t)\delta\Sigma(t)) = S_0(t)M(\delta B(t))\Sigma_0(t).$$

Integrating the above and using the condition $\lim_{t\to\infty} S_0(x+t\xi,\xi) = I_3$ we can state that

$$D\mathcal{F}(M(B^0))M(\delta B) = \lim_{t\to\infty} \delta\Sigma(x+t\xi,\xi) = \int_{-\infty}^{\infty} S_0(t)M(\delta B(t))\Sigma_0(t)\ \mathrm{d}t. \tag{4.10}$$

Now from the above if we consider the case for $B^0 = 0$, we have

$$D\mathcal{F}(M(B^0=0))M(\delta B) = \lim_{t\to\infty} \delta\Sigma(x+t\xi,\xi) = \int_{-\infty}^{\infty} M(\delta B(t))\ \mathrm{d}t, \tag{4.11}$$

since $S_0 = \Sigma_0 = I_3$. Now relating this to our $S(M(B))(x,\xi)$ notation this implies that specifically in the plane normal to η we can solve the linear approximation for small B simply by solving the two dimensional ray transform

$$e_1 \cdot S(M(B))(x,\xi)e_2 = X(B_3)(x,\xi). \tag{4.12}$$

With cyclic permutations we can retrieve the magnetic field. This can be done using any two-dimensional Radon inversion method outlined in Chapter 2. Moreover this result is already known by experimentalists such as [22].

To test our formulation we need to simulate a magnetic field which is small enough (weak) yet strong enough to measure and can be utilized to generate data. Therefore, the Biot-Savart law, [43], is employed. The central slice of a simulated solenoid is shown in Figure 4.2.

Biot-Savart law

The Biot-Savart law describes the magnetic field, B, at a point, r, generated by a steady flow of charges along the path of the current, I. It is commonly stated as

$$B = \frac{\mu_0}{4\pi} I \int \frac{\mathrm{d}L \times r'}{|r'|^3}, \tag{4.13}$$

where r' is the distance from the infinitesimal wire segment, $\mathrm{d}L$, to the point r. Here $\mu_0 = 4\pi \times 10^{-7}\ \mathrm{NA}^{-2}$ is the permeability of free space. The magnetic field is calculated for each point in a point cloud surrounding a solenoid constructed of straight wire segments. The procedure uses (4.13) to calculate the sum over the contributions from each wire segment of sufficiently small length (1 mm).

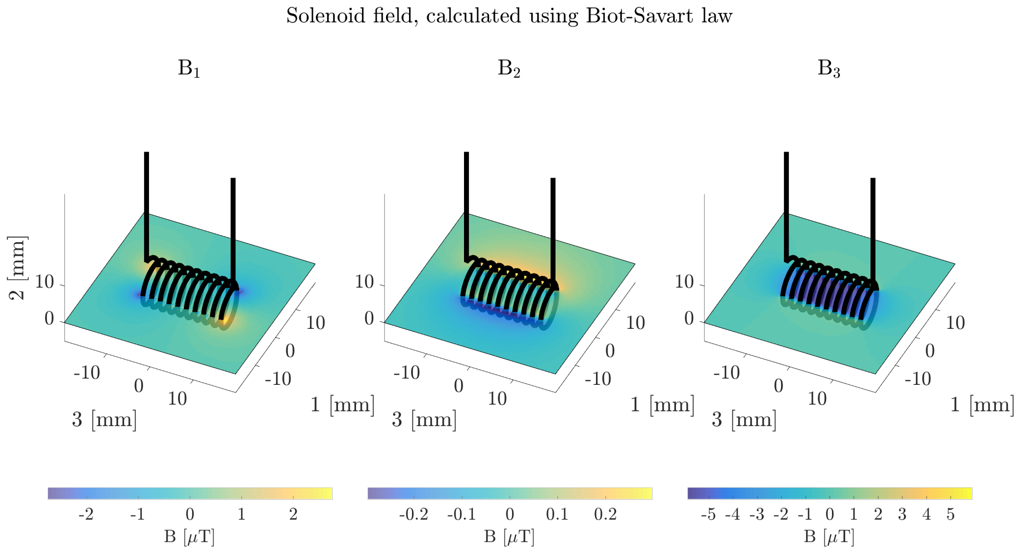

Figure 4.2: Central slice of a simulated solenoid

4.2.1 Forward model

Let us look at how PNMFT data is generated. Detail of how the forward solver operates can be explained by taking a single neutron at a time. Consider a neutron fired from point (ζ_1, η, ξ_1) and detected at (ζ_2, η, ξ_2), since a parallel beam setup is emulated. Initially the spin of the neutron is aligned using three unit vectors e_1, e_2 and e_3 which form the initial spin matrix, $\Sigma(t = 0) = I_3$. Thereafter the spin, $\Sigma(t_{\text{entry}})$ is altered as the neutron passes a polariser before entering the magnetic (solenoid) field of interest. With the aid of Section 2.2, the ray tracing algorithm calculates the intersection lengths the neutron makes with the voxel grid. These specific voxels are referenced and utilized for solving the spin differential equation (4.3) assuming the magnetic field is piecewise constant.

Analytic solution of ODE system

There are several methods to solve the forward problem stated. One such method is to analytically solve the system of ODEs using the matrix exponential. Consider the eigenvalues of the matrix stated prior to (4.3), which are

$$\lambda_1 = 0, \ \lambda_2 = -i|B|, \ \lambda_3 = i|B|, \tag{4.14}$$

where $|B| = \sqrt{B_1^2 + B_2^2 + B_3^2}$ and the corresponding eigenvectors are

$$\mu_1 = \begin{pmatrix} \frac{B_1}{B_3} \\ \frac{B_2}{B_3} \\ 1 \end{pmatrix},$$

$$\mu_2 = \begin{pmatrix} \frac{(-B_3 B_1^3 - B_3^3 B_1) + (-B_2|B|B_1^2 - B_2 B_3^2|B|)i}{|B|^2 B_1^2 + B_2 2^2 B_{xi}^2} \\ \frac{(-B_2 B_3^3 - B_1^2 B_2 B_3) + (|B|B_1^3 + B_1 B_\xi^2|B|)i}{|B|^2 B_1^2 + B_2^2 B_3^2} \\ 1 \end{pmatrix}, \quad \text{and}$$

$$\mu_3 = \begin{pmatrix} \frac{(-B_3 B_1^3 - B_3^3 B_1) + (B_2|B|B_1^2 + B_2 B_3^2|B|)i}{|B|^2 B_1^2 + B_2^2 B_3^2} \\ \frac{(-B_1^2 B_2 B_3 - B_2 B_3^3) + (-B_1^3|B| - B_1 B_3^2|B|)i}{|B|^2 B_1^2 + B_2^2 B_3^2} \\ 1 \end{pmatrix}. \tag{4.15}$$

The real eigenvalue ($\lambda = 0$ and μ_1) will contribute to one solution of the form $e^{\lambda_1}\mu_1 = \mu_1$. The other two eigenvalues are purely imaginary and we have the property that $\mu_3 = \bar{\mu_2}$. Hence another solution will be of the form

$$e^{\lambda_2 t}\mu_2 = (\cos(|B|t) - i\sin(|B|t))\,\mu_2. \tag{4.16}$$

If we separate (4.16) into real and imaginary parts we yield

$$u(t) + iv(t) =$$

$$\frac{1}{B_2^2 B_3^2 + B_1^2|B|^2} \begin{pmatrix} (-B_1^3 B_3 - B_1 B_3^3)\cos(|B|t) - (B_1^2 B_2|B| - B_2 B_3^2)\sin(|B|t) \\ (-B_1^2 B_2 B_3 - B_2 B_3^3)\cos(|B|t) + (B_1^3|B| + B_1 B_3^2|B|)\sin(|B|t) \\ \cos(|B|t) \end{pmatrix}$$

$$+\frac{1}{B_2^2 B_3^2 + B_1^2|B|^2} \begin{pmatrix} (-B_1^2 B_2|B| - B_2 B_3^2|B|)\cos(|B|t) + (B_1^3 B_3 + B_1 B_3^3)\sin(|B|t) \\ (B_1^3|B| + B_1 B_3^2|B|)\cos(|B|t) + (B_1^2 B_2 B_3 + B_2 B_3^3)\sin(|B|t) \\ -\sin(|B|t) \end{pmatrix} i. \tag{4.17}$$

By the principle of superposition our solution to (4.3) when $M(B)$ is a constant matrix, is

$$\sigma(t) = c_1\mu_1 + c_2 u(t) + c_3 v(t), \text{ for } c_1, c_2, c_3 \in \mathbb{R}. \tag{4.18}$$

The drawback of utilising such a method is that for certain values many degenerate solutions will arise, as can be seen by the eigenvectors (4.15) and the expression for

$u(t)+\mathrm{i}v(t)$ in (4.17). One may ponder why go through such difficulty and not employ a numerical matrix exponential code to solve the spin differential equation (4.3). Precisely, we do not always know what type of algorithm is being used to calculate it. The author did experiment with the matrix exponential code in MATLAB and was not convinced with the result.

The initial condition for each pixel is $\Sigma(t_{\text{entry}})$ and in practice the spin matrix, when the neutron leaves the referenced voxel, $\Sigma(t_{\text{exit}})$, is calculated by *Rodrigues' rotation formula* [36], an efficient algorithm to compute the exponential map $\mathfrak{so}(3)$, the Lie algebra of $SO(3)$, to $SO(3)$ without actually computing the full matrix exponential. In order to use this result, a unit vector describing the axis of rotation (direction of the field) and the precession angle, ϕ, which the neutron rotates by within the referenced voxel is needed. This is determined by $\phi=\gamma\frac{L}{v}|B|$, where L is the neutron path length within the voxel, v is the velocity of the neutron and $|B|$ is the strength of the magnetic field in the current voxel.

Rodrigues' Rotation Formula

If v is a vector in $\mathbb{R}^3$ and k is a unit vector describing an axis of rotation about which v rotates by an angle ϕ according to the right hand rule, the **Rodrigues' rotation formula** is

$$v_{\text{rot}}=v\cos\phi+(k\times v)\sin\phi+k(k\cdot v)(1-\cos\phi). \tag{4.19}$$

Note if we denote H as the cross product matrix, then

$$Hv=k\times v=\begin{pmatrix}0 & -k_3 & k_2\\ k_3 & 0 & -k_1\\ -k_2 & k_1 & 0\end{pmatrix}\begin{pmatrix}v_1\\ v_2\\ v_3\end{pmatrix}$$

One important property worth noting is that iterating the cross product on the right is equivalent to multiplying by H on the left, i.e. $H(Hv)=k\times(k\times v)$. Formula (4.19) above can be rewritten as $v_{\text{rot}}=v+(\sin\phi)Hv+(1-\cos\phi)H^2v$. Factorising the v allows us to write this in compact form. Specifically, $v_{\text{rot}}=Rv$, where

$$R=I+(\sin\phi)H+(1-\cos\phi)H^2, \tag{4.20}$$

is the rotation matrix through an angle ϕ anticlockwise about the axis k. Rodrigues' rotation formula is applied thrice to the columns of matrix $\Sigma(t_{\text{entry}})$ to give us $\Sigma(t_{\text{exit}})$

which is the spin when the neutron leaves the current voxel to the next referenced voxel. The initial spin matrix is changed to $\Sigma(t_{\text{entry}}) = \Sigma(t_{\text{exit}})$ so that (4.3) can be solved again with the new initial condition. This process is repeated until the neutron passes through the entire magnetic field. Finally the neutron passes through an analyser changing $\Sigma(t_{\text{exit}})$ before the final spin is recorded by the detector as

$$\Sigma\left(t_{\text{end}}\right) = \begin{pmatrix} \Sigma_{\zeta\zeta} & \Sigma_{\zeta\eta} & \Sigma_{\zeta\xi} \\ \Sigma_{\eta\zeta} & \Sigma_{\eta\eta} & \Sigma_{\eta\xi} \\ \Sigma_{\xi\zeta} & \Sigma_{\xi\eta} & \Sigma_{\xi\xi} \end{pmatrix}. \tag{4.21}$$

This is repeated according to the number of neutrons fired at every angular increment in the usual tomographic data acquisition process. Hence the size of the data array is $9 \times \omega \times \theta$, where ω is the total number of neutrons and θ is the total number of angles. Nevertheless, for the linearized inverse problem it has been shown that only 3 out of 9 possible values are required as data, namely $\Sigma_{\zeta\eta}, \Sigma_{\eta\xi}$ and $\Sigma_{\xi\zeta}$, due to (4.12). The simulated data from our forward model has been validated. Initially simple calculations were made to see if realistic data was simulated. Moreover the simulated data has been validated experimentally which is shown in Figure 2 of [37] where experimental PNMFT data matches our simulated data.

4.2.2 Reconstructing PNMFT Data

The central slice of the solenoid (magnetic field) simulated by the use of the Biot-Savart law in Figure 4.2, is utilized in the forward model by the process described above to generate data. Initially the solenoid was simulated on a 180×180 pixel grid. To simulate the data 270 rays of neutrons (uniform velocity with wavelength = 5 Å) were fired for every angular increment (1 degree in this case) of the usual tomographic data acquisition process. The data is binned by a factor of three to give the data which is three sets of 90×120 arrays for each of the three components from the spin matrix. Furthermore, 5% pseudo-random noise was added before employing the inverse radon transform to reconstruct the components of the magnetic field. In order to do this, primarily the data has to be transformed to a sample reference frame (ζ', η, ξ'). As each measurement consists of a 3×3 matrix, the measured matrices need to be transformed. Since the sample was rotated around the vertical axis, η, the rotation matrix is given by

$$R(-\phi) = \begin{pmatrix} \cos(-\phi) & 0 & \sin(-\phi) \\ 0 & 1 & 0 \\ -\sin(-\phi) & 0 & \cos(-\phi) \end{pmatrix}.$$

The rotation matrix which describes the rotation of the neutron as it traverses the magnetic field is denoted as Σ' and is specifically calculated as

$$\Sigma' = R(-\phi)\Sigma(\phi)R^T(-\phi).$$

Thereafter the data is filtered which is done in the Fourier domain with a Hamming filter. Once complete we backproject the filtered data to achieve the reconstructed components of the magnetic field. This process has been explained in Section 2.3.1 in Chapter 2. Note that reconstruction was performed on a grid which does not evenly divide the grid used for simulation, i.e. 67×67.

The relative errors from top to bottom in Figure 4.3 corresponding to B_1, B_2, B_3 and $|B(x(t))|$ (magnetic field strength) are $20\%, 16\%, 11\%$ and 9% respectively. Since reconstruction is of the central slice of a solenoid, with strength approximately 5.8 μT, the maximum a single neutron precesses as it passes through the domain is 2 degrees. This is well within the range for the linearized problem to work. When the strength of the magnetic field increases to the extent that a single neutron precesses more than $14°$ approximately, this specific method fails. This is when the small angle approximation breaks, i.e. when $\sin\phi \neq \phi$. One such illustration is present in Figure 4.4 where one notices the artefacts coming through. The relative error for the B_2 component is 1.5183. How can one reconstruct strong enough magnetic fields which make the neutron precess more than $14°$? Indeed the answer lies in some recent work [37].

Inverse Rodrigues' Rotation Formula

The exponential map, $\exp : \mathfrak{so}(3) \to SO(3)$ is essentially what the Rodrigues' rotation formula is doing. Since we want the opposite to occur, consider the logarithmic map, $\log : SO(3) \to \mathfrak{so}(3)$. We continue to let H denote the 3×3 matrix that calculates the cross product with a rotation axis k for all vectors v. The angle of rotation ϕ is easily retrieved by the trace (tr) of the rotation matrix, Σ'. Thus $\phi = \arccos\left(\frac{\mathrm{tr}(\Sigma')-1}{2}\right) =$

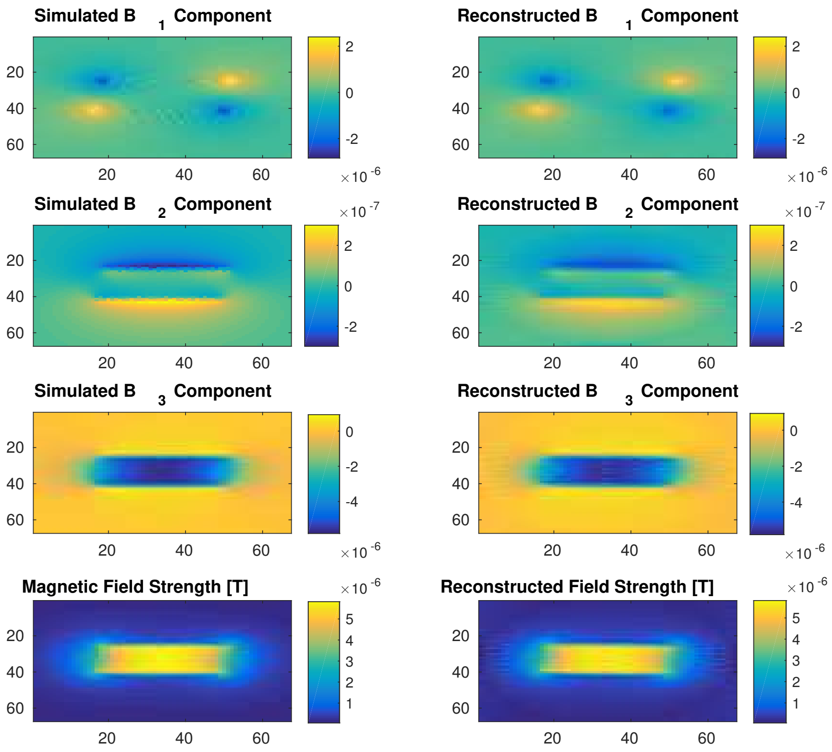

Figure 4.3: Central slice reconstruction of a solenoid.

$\arccos\left(\frac{\mathrm{tr}(\Sigma)-1}{2}\right)$, which is used to find the normalized axis

$$k = \frac{1}{2\sin\phi}\begin{pmatrix} \Sigma'_{\xi\eta} - \Sigma'_{\eta\xi} \\ \Sigma'_{\zeta\xi} - \Sigma'_{\xi\zeta} \\ \Sigma'_{\eta\zeta} - \Sigma'_{\zeta\eta} \end{pmatrix}.$$

In terms of matrices this is just $H = \frac{(\Sigma' - \Sigma'^T)}{2\sin\phi}$. Finally we can recover the magnetic field by the Radon transform since $\frac{-\phi}{c\lambda L}(e_i \cdot H \cdot e_j) = X(B_k)$, where $\{i,j,k\} \in \{1,2,3\}$, λ is the wavelength of the neutron and $c = 4.632 \times 10^{14}\ \mathrm{T}^{-1}\mathrm{m}^{-2}$, known as the Larmor constant. In essence we are still using the linearization in this technique. Consider the fact that the effect of the magnetic field is cumulative along the ray which is apparent as this is governed by the system of ODEs in (4.3). This implies that the forward problem mapping the magnetic field to the measurements (PNMFT data) is not linear. Hence we can not simply use an inverse Radon transform and to overcome this issue we first apply a transformation on the data and then linearize the problem about $B = 0$. An important advantage of using the logarithmic chart is that $\mathfrak{so}(3)$

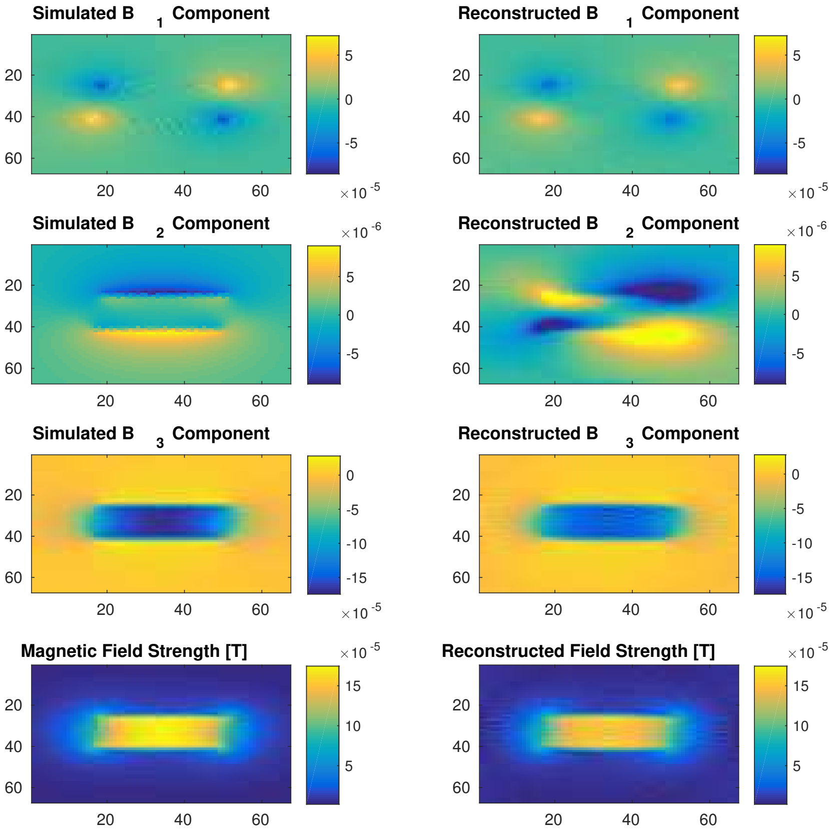

Figure 4.4: Failed reconstruction by known experimentalist method (4.12).

forms a vector space which allows the use of standard filtered backprojection methods to reconstruct the data.

To test this approach, data is simulated on a 180×180 pixel grid in the manner explained in Section 4.2.1 with a magnetic field of strength, $580\mu T$. To simulate the data 270 rays of neutrons (uniform velocity with wavelength = 5 Å) were fired for every angular increment (1 degree in this case) of the usual tomographic data acquisition process. The data is binned by a factor of three to give the data which is an array of size $90 \times 120 \times 9$. Unlike the method described earlier, we need all the data and not just three components of the spin matrix. Furthermore, 5% pseudo-random noise was added before employing the inverse Radon transform to reconstruct the components of the magnetic field. For this specific magnetic field the maximum a single neutron will precess is 176° and the reconstructed results are shown in Figure 4.5. The relative errors for the reconstructed components B_1, B_2, B_3 and $|B(x(t))|$

(magnetic field strength) are 0.3245, 0.219 , 0.111 and 0.235 respectively. However

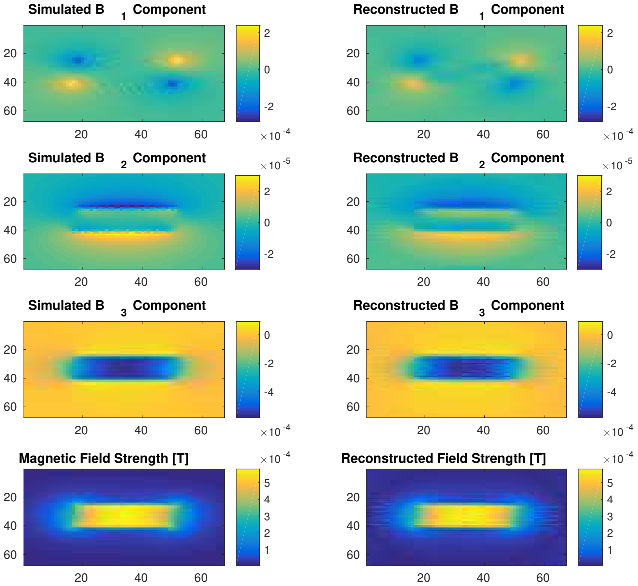
Simulated B_1 Component
Reconstructed B_1 Component
Simulated B_2 Component
Reconstructed B_2 Component
Simulated B_3 Component
Reconstructed B_3 Component
Magnetic Field Strength [T]
Reconstructed Field Strength [T]

Figure 4.5: Logarithmic approach for magnetic field of strength $580\mu T$.

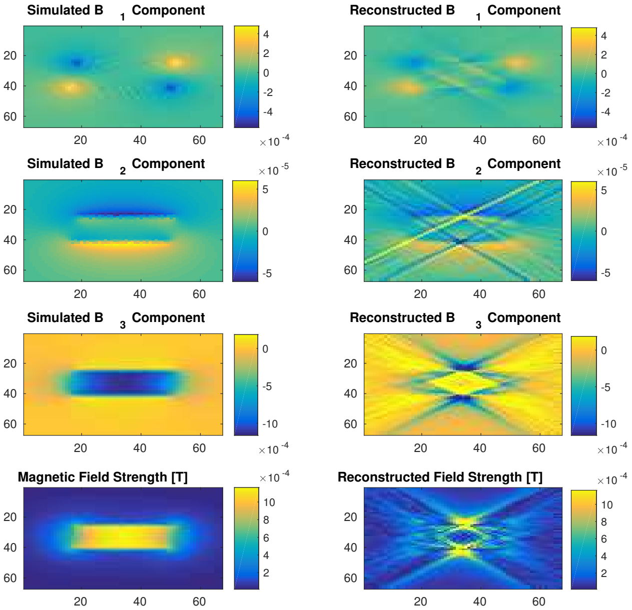
Simulated B_1 Component
Reconstructed B_1 Component
Simulated B_2 Component
Reconstructed B_2 Component
Simulated B_3 Component
Reconstructed B_3 Component
Magnetic Field Strength [T]
Reconstructed Field Strength [T]

Figure 4.6: Logarithmic approach fails for magnetic field of strength $1160\mu T$.

if we choose a magnetic field of strength $1160\mu T$, the logarithmic approach fails, as shown in Figure 4.6 where the maximum a neutron will precess is 351°. At this point we delay our discussion on PNMFT to Chapter 6 where we introduce techniques for nonlinear inverse problems. It is apparent from the exploration of methods for linear inverse problems that these are unsuccessful.

4.3 Diffraction Strain Tomography

We briefly discuss an overview of [27] in this section. Firstly, consider both x-rays and neutrons are diffracted by crystals and this is the fundamental idea used in crystallography. Technically the manner in which we perceive a crystal is that they consist of a periodic spatial arrangement of atoms, taken to be located at points. For our purpose the important feature is that there is a family of planes normal to a set of one or more vectors unit k_i, separated by distances d_i. It is usual to call each family of parallel planes, a *crystallographic plane*. When a parallel beam of monochromatic x-rays (or neutrons), with wavelength λ, in the direction ξ, are incident on the crystal such that $\theta = \cos^{-1} \xi \cdot k_i$ satisfies Bragg's law,

$$2d_i \sin\theta = n\lambda, \tag{4.22}$$

for some $n \in \mathbb{N}$, part of the beam is *diffracted* and continues in the direction η in the plane defined by k and ξ at an angle 2θ to ξ. The integer n is called the *order of diffraction*. Bragg Edge diffraction is thought of as *elastic scattering* in that the diffracted x-rays (or neutrons) have the same wavelength (and hence energy) as the incident x-rays. We will ignore any attenuation of the diffracted x-rays by the material.

Metals are polycrystalline materials, that is they consist of small randomly oriented crystals. The assumption that x-rays (or neutrons) incident on some polycrystalline material, like metals, form a narrow beam (for example cylindrical) centred on some ray. This is possible by using a synchrotron source. Consider, a beam along a given ray $x + t\xi$, the diffracted rays when observed at a distance L on a plane normal to the ray lie on a circle centred on the projection of x onto this plane with a radius $L \sin 2\theta_{i,n}$, where i the crystallographic plane and n is the order of diffraction. An important remark is that for polycrystalline materials, the diffraction pattern is averaged over the group of rotations in three space.

Essentially, circles that arise in the diffraction pattern of the unstrained case are known as *Debye-Scherrer rings*. However, when the metal (polycrystalline material) is subjected to linear elastic strain the crystals are deformed changing their diffraction pattern. Often for high energy, small λ, x-rays (called *hard x-rays*) and for low orders of diffraction n, the Bragg angles 2θ are small, perhaps two or three degrees. On the other hand it is possible in a synchrotron beam to have the detector screen many tens of meters away. This means that while the Debye-Scherrer rings can still be measured normal to the plane k_i, the diffraction can be considered approximately parallel to the screen giving rise to deformed Debye-Scherrer rings, which are simply ellipses.

We restrict our attention to the case for small θ, in which the diffraction pattern contains only information about the strain transverse to the direction of travel, ξ. We might consider this a case of *rich tomography* in that for each ray we have not a scalar or a vector value but a function of two variables. One approach would be simply to solve the linear equations relating the strains in a grid of voxels to the intensities measured on the screens. Even for only one rotation axis, for similar pixel and voxel dimensions, we would have far more equations than variables, whereby solving such a system would be inefficient. Our aim therefore is to reduce the redundancy of the data whilst retaining sufficient information for a unique reconstruction.

Given the wealth of data in a diffraction pattern, it might be supposed that we could at least reconstruct the distribution of stresses along the beam. A typical diffraction pattern consists of a series of concentric ellipses for different diffraction orders, and we might suspect that it would be possible to fit a weighted sum of ellipses to this pattern. Hence interpreting the weights of the proportion of each strain tensor present along the ray. Nevertheless, this is not the case as different distributions of ellipses can produce the same image but [27] shows that a certain moment of the diffraction pattern in the required direction is the correct choice. For a specific density, χ, stated in [27], we have

$$\int\limits_{-\infty}^{\infty} a_{ij}(p)\mathrm{d}p = \int\limits_{S^2\mathbb{R}^2} a_{ij}\chi(A)\mathrm{d}A, \tag{4.23}$$

resulting in three moment calculations along radial directions of the diffraction pattern, namely the TRT $Jf(x,\xi)$.

Notice that the component $(\eta \cdot Jf(\xi,x)\cdot\eta) = X[\eta\cdot(f\cdot\eta)](x,\xi)$, for $\xi \in \eta^\perp$ is simply the scalar x-ray transform in the plane through x normal to η. As observed in [39, Sec 5.1.6] this component can be reconstructed using any inversion formula for the planar Radon transform inversion plane by plane, including the examples given in Chapter 2. Choosing six rotation axes η_i so that the outer products $\eta\otimes\eta$ are linearly independent in $S^2\mathbb{R}^3$ recovers f everywhere.

The authors of [27] mention "*One suspects that a reconstruction would be possible* *with less than six rotation axes. Indeed for each ray the above algorithm uses a moment of the diffraction pattern only in the direction of the rotation, a single measurement of a one-dimensional section of the diffraction pattern. It would be desirable for practical purposes to have an explicit reconstruction algorithm that uses rotation about fewer axes, but makes better use of the data for each ray.*" Fortunately such a novel method, anticipated by both Professor William Lionheart and Professor Phil Withers, has been developed and will be mentioned in Section 5.2.

4.4 Photoelastic Tomography

Photoelasticity is the effect whereby the introduction of stress in certain transparent materials causes anisotropy in the otherwise isotropic permittivity, giving rise to birefringence, an optical property of a material having a refractive index that depends on the polarization and propagation direction of light. The optical anisotropy, which depends on the stress distribution within the material, may be measured using polarimetry [49, 2]. With the assumption that stress is fairly weak, the ordinary and extraordinary rays can be considered to be straight lines and the relationship between the anisotropic permittivity tensor and the stress can be assumed to be linear. This allows us to use tomographic techniques to recover the internal stress pattern of an object.

Polarized light is used for Photoelasticity and to model light propagation through a photoelastic medium, an approximation to Maxwell's equations is usually utilized, the Rytov-Sharafutdinov law. If [39] is consulted, a full derivation to such a law may be found. Thus for a complex electric field, E, the Rytov-Sharafutdinov law states

$$\frac{\mathrm{d}E}{\mathrm{d}t} = \frac{\mathrm{i}}{2\epsilon_0} P_\xi(f)E, \tag{4.24}$$

where ϵ_0 is treated as a constant. Now backtracking to Section 3.1 allows us to relate (4.24) as $A(\xi, x) = P_\xi f(x)$. Interestingly, unlike PNMFT the direction of the ray, ξ, has a significant influence on the data. Consider $P_\xi f$ is a fourth order homogeneous polynomial in ξ, as described by (3.38). This fundamental difference make inverse problems corresponding to forward problems like (4.24) difficult to solve. Let us pose a solution to the initial value problem as $E(t) = U(t)E(t_0)$ and expand it as a (formal)

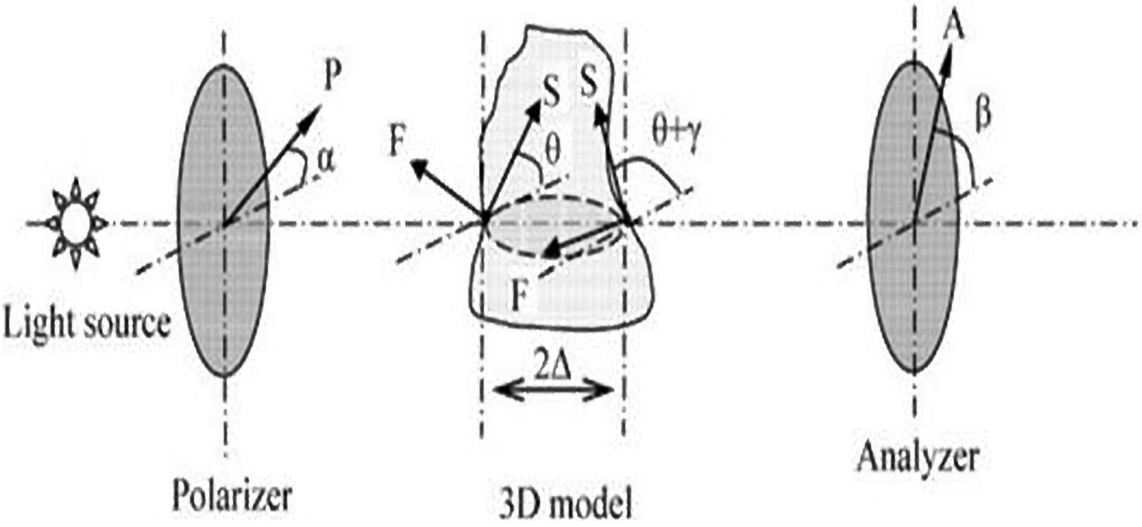

Figure 4.7: Configuration of a plane polariscope, described in [49].

Neumann series. Thus

$$U(t) = I + \int_{t_0}^{t} \frac{\mathrm{i}}{2\epsilon_0} P_\xi f(t_1)\, \mathrm{d}t_1 + \int_{t_0}^{t} \mathrm{d}t_1 \frac{\mathrm{i}}{2\epsilon_0} P_\xi f(t_1) \int_{t_0}^{t_1} \mathrm{d}t_2 \frac{\mathrm{i}}{2\epsilon_0} P_\xi f(t_2) + ..., \tag{4.25}$$

which is truncated to first order and this is actually what Sharafutdinov [39] refers to as the TRT of f along the ray $x + t\xi$. However in the context of polarized light it is very difficult to measure the absolute phase change, so actually for weak strains, the TTRT is used. Even though the operator Q_ξ is used, this does not alter the order of the polynomial for the direction, ξ, which is shown in (3.51).

As mentioned, determination of stress can be carried out using the method of Fourier polarimetry. The experimental setup is based upon that of a plane polariscope - the sample to be investigated is positioned between a rotating polariser and analyser. The polariser and analyser are set up so that the angles through which each is rotated are directly proportional. Light from a source (a laser) is passed through the polariser, sample and analyser. The intensity of transmitted light at different polarisations is measured by a suitable detector, such as a CMOS or CCD camera. A simple plane polariscope can be seen in Figure 4.7. Fourier polarimetry relies on the principle that a photoelastic medium can be treated as a linear retarder and a rotator; both systems would have the same effect upon transmitted light. The characteristic retardation, 2Δ, and the characteristic direction, θ are associated with the linear retarder whereas the characteristic angle, γ, describes the operation of the rotator. These three parameters are regarded as the characteristic parameters. The intensity of transmitted light at each position of the polariser and analyser is recorded by the detector. By performing the Fourier transform of the output intensity, the characteristic parameters of the system can be calculated. Determination of the characteristic parameters gives rise to the determination of the stress tensor and hence the internal stress pattern can be deduced by the algorithm developed in Section 5.2.

The apparatus and procedure was first conceptually designed by Rachel Tomlinson, William Lionheart and David Szotten. The instrumental setup was initially located at the PSI where several students have worked to get stress pattern reconstruction of experimental data, each of them failing. This tempted us to look at the code and reconstruction algorithm to see whether an error is present in the code or the algorithm. Indeed, the author has worked for some time now on this issue and has successfully implemented correct versions of the code that was reconstructing the stress pattern. In particular there is an issue with formula (5.26), (5.27) and (5.28) in [46]. Furthermore, the question of stability for the reconstruction algorithm is dealt with in Section 5.6. Sharafutdinov calls it an unstable reconstruction algorithm for three axes data.

Chapter 5

Reconstruction Algorithms and Numerical Results

Throughout Chapter 4 an outline to the background of imaging modalities has been mentioned. Along with introducing the application of PNMFT, the reconstruction algorithm was outlined and numerics were shown in Section 4.1. The tensor ray transforms stated in Chapter 3 have inversion procedures but these are for complete data. These are impracticable for experimentalists and imaging techniques such as x-ray/neutron diffraction tomography and polarized light tomography (Photoelasticity). With limited data can we reconstruct data arising from such modalities. The answer in the affirmative can be seen as a result of the derivation of an explicit plane-by-plane procedure which only uses backprojection in the plane, applying one-dimensional filters and Fourier inversion techniques all of which have been illustrated by numerical examples through the use of the Radon transform in Chapter 2. In Section 5.6 we illustrate the reconstruction of simulated data by specifying a few test phantoms.

Given that, in the proposed application, each projection is acquired laboriously using a raster scan, it is advantageous to perform the reconstruction using data from a minimum number of axes, making the most out of the data collected from each projection. Thus the derived algorithm, both for the TRT and TTRT, only require data from three axes. Furthermore, we go on to show that data from only two rotation axes are insufficient in the general case. For the potential case we give an explicit reconstruction technique using two axis data and show that data from one axis is insufficent. We present for the first time, some numerical results for our three axis reconstruction algorithm using simulated data.

5.1 Main algebraic equations

We transform equations (3.69), (3.70) and (3.71) to algebraic equations by applying the Fourier transform to backprojected data. Before we can do this we pay attention to several results which are a follow on from [40].

5.1.1 Curl components of tensor and vector fields

We require what [39] refers to as the tangential component $\tau g \in C^\infty(\mathbb{R}^2)$ of a vector field $g \in C^\infty(\mathbb{R}^2;\mathbb{C}^2)$, which is defined by

$$(\tau g)(y) = (g(y) \cdot y^\perp). \tag{5.1}$$

Here the vector $y^\perp$ is the result of rotating y by $\pi/2$ in the positive direction. Of course, one can understand (5.1) as the two-dimensional curl of a vector field in Fourier (frequency) space. The manifold $T\mathbb{S}^1$ can be identified with $\mathbb{R}\times\mathbb{S}^1$ by the diffeomorphism $(p,\xi) \mapsto (\xi, p\xi^\perp)$ for $(p,\xi) \in \mathbb{R}\times\mathbb{S}^1$. Therefore the derivative $\frac{\partial}{\partial p} : \mathcal{S}(T\mathbb{S}^1) \to \mathcal{S}(T\mathbb{S}^1)$ is well defined. For a vector field $f \in \mathcal{S}(\mathbb{R}^2;\mathbb{C}^2)$, the tangential component of the Fourier Transform $F[f]$ is recovered by the LRT, If, by the formula

$$\tau F[f] = \frac{\mathrm{i}}{2}|y| F\left[B\left(\frac{\partial(If)}{\partial p}\right)\right]. \tag{5.2}$$

We see in [26] and [40], the tangential component, $\tau g \in C^\infty(\mathbb{R}^2)$, of a tensor field $g \in C^\infty(\mathbb{R}^2; S^2\mathbb{C}^2)$ is defined by

$$(\tau g)(y) = |y|^2 \operatorname{tr} g - [(g(y)\cdot y)\cdot y]. \tag{5.3}$$

This is exactly the Fourier transform of the single unique non-zero component of the compatibility tensor of Barré de Saint-Venant in the plane

$$W(g) = \frac{\partial^2 g_{11}}{\partial x_2^2} - 2\frac{\partial^2 g_{12}}{\partial x_1 \partial x_2} + \frac{\partial^2 g_{22}}{\partial x_1^2}, \tag{5.4}$$

which is also sometimes described as the curl-curl of a symmetric tensor field. For $f \in \mathcal{S}(\mathbb{R}^2; S^2\mathbb{C}^2)$, the tangential component of the Fourier transform $F[f]$ is recovered from the LRT, If, as

$$\tau F[f] = \frac{1}{2}|y|^3 F[B(If)]. \tag{5.5}$$

For $\phi \in \mathcal{S}(T\mathbb{S}^1)$, the function $B\phi(x)$ is C^∞-smooth and bounded on $\mathbb{R}^2$ but does not decay fast enough to be in the Schwartz class. Thus we understand the Fourier transform in the distribution sense in (5.2) and (5.5).

5.1.2 Derivation of the system of equations

Let $f \in \mathcal{S}(\mathbb{R}^3; S^2\mathbb{C}^3)$ be a symmetric tensor field and denote by $f' = F_{\eta^\perp}[f] \in \mathcal{S}(\mathbb{R}^3; S^2\mathbb{C}^3)$, the partial Fourier transform of f. For any $s \in \mathbb{R}$, the restriction of the vector field $\eta \times (f' \cdot \eta)$ to the plane $s\eta + \eta^\perp$ coincides with the two-dimensional Fourier transform of $(\eta \times (f \cdot \eta))|_{s\eta+\eta^\perp}$. This is $(\eta \times (f' \cdot \eta))|_{s\eta+\eta^\perp} = F_{\eta^\perp}[(\eta \times (f \cdot \eta))|_{s\eta+\eta^\perp}]$.

We then apply formula (5.2) to the vector field $(\eta \times (f \cdot \eta))|_{s\eta+\eta^\perp}$, giving

$$\tau((\eta\times(f'\cdot\eta))|_{s\eta+\eta^\perp})(s\eta+y) = \frac{\mathrm{i}}{2}|y|F_{\eta^\perp}\left[B_\eta\left(\frac{\partial(I_{\eta,s}((\eta\times(f\cdot\eta))|_{s\eta+\eta^\perp}))}{\partial p}\right)\right] \quad \text{for} \quad y \in \eta^\perp, \tag{5.6}$$

Using (3.69), we can transform (5.6) giving

$$\tau((\eta\times(f'\cdot\eta))|_{s\eta+\eta^\perp})(s\eta+y) = \frac{\mathrm{i}}{2}|y|F_{\eta^\perp}\left[\left(B_\eta\frac{\partial(J^1_\eta f)}{\partial p}\right)(s\eta+x)\right], \tag{5.7}$$

Note that (5.1) gives

$$\tau((\eta\times(f'\cdot\eta))|_{s\eta+\eta^\perp})(s\eta+y) = [\eta\times(f'(s\eta+y)\cdot\eta)]\cdot(\eta\times y) = (f'(s\eta+y)\cdot\eta)\cdot y. \tag{5.8}$$

Upon substitution of (5.8) into the LHS of (5.7) and applying the one-dimensional Fourier transform $F_{\mathbb{R}\eta}$ taking s to σ gives

$$(\hat{f}(\sigma\eta+y')\cdot\eta)\cdot y' = \frac{\mathrm{i}}{2}|y'|F\left[\left(B_\eta\frac{\partial(J^1_\eta f)}{\partial p}\right)(s\eta+x')\right] \quad \text{for} \quad y' \in \eta^\perp, \tag{5.9}$$

where $\hat{f}$ is the three-dimensional Fourier transform $F[f]$. Since $y' \in \eta^\perp$ and $\sigma \in \mathbb{R}$, we let $y = \sigma\eta + y'$, where $y' = \Pi_\eta y$. Hence the previous formula (5.9) can be written as

$$[(\hat{f}(y)\cdot\eta)\cdot(\Pi_\eta y)] = \frac{\mathrm{i}}{2}|\Pi_\eta y|F\left[\left(B_\eta\frac{\partial(J^1_\eta f)}{\partial p}\right)(x)\right], \tag{5.10}$$

Note that (5.10) is identical to the off-diagonals for the TTRT operator case so we don't repeat the derivation here. Moreover this will just reconstruct the solenoidal part of the off-diagonals since the Fourier transform interweaves with the solenoidal part.

For any $s \in \mathbb{R}$, the slice $\iota^*_{\eta,s} f'$ coincides with the two-dimensional Fourier transform of the slice $\iota^*_{\eta,s} f$, i.e., $\iota^*_{\eta,s} f' = F_{\eta^\perp}[\iota^*_{\eta,s} f]$, where the Fourier transform on the plane $s\eta + \eta^\perp$. Henceforth, we refer to the adjugate of the slice of f' restricted to the plane as $\mathrm{Adj}_{\eta^\perp}(\iota^*_{\eta,s} f') = h'$. Upon application of formula (5.5) to h', we see

$$[\tau(h')](s\eta + y) = \frac{1}{2}|y|^3 F_{\eta^\perp}[B_\eta(I_{\eta,s}(\mathrm{Adj}_{\eta^\perp}(\iota^*_{\eta,s} f)))] \quad \text{for} \quad y \in \eta^\perp. \tag{5.11}$$

Using Lemma 3.4 we can rewrite the above as

$$[\tau(h')](s\eta + y) = \frac{1}{2}|y|^3 F_{\eta^\perp}[B_\eta(J^2_\eta f)(s\eta + x)] \quad \text{for} \quad y \in \eta^\perp, \tag{5.12}$$

Now, we apply formula (5.3) to the field $g = h' \in \mathcal{S}(s\eta + \eta^\perp; S^2\eta^\perp_{\mathbb{C}})$ to give

$$[\tau(h')](s\eta + y) = |y|^2 \mathrm{tr}\, h'(s\eta + y) - [(h'(s\eta + y)\cdot y)\cdot y] \quad \text{for} \quad y \in \eta^\perp. \tag{5.13}$$

Substitution of (5.13) into (5.12) gives

$$|y|^2 \mathrm{tr}\, h'(s\eta + y) - [(h'(s\eta + y)\cdot y)\cdot y] = \frac{1}{2}|y|^3 F_{\eta^\perp}[B_\eta(J^2_\eta f)(s\eta + x)] \quad \text{for} \quad y \in \eta^\perp. \tag{5.14}$$

By applying the one-dimensional Fourier transform on $\mathbb{R}\eta$ to the above, we obtain

$$|y'|^2 \mathrm{tr}\, \hat{h}(\sigma\eta + y') - [(\hat{h}(\sigma\eta + y')\cdot y')\cdot y'] = \frac{1}{2}|y'|^3 F[B_\eta(J^2_\eta f)(s\eta + x')], \tag{5.15}$$

for $y \in \eta^\perp$. As before, employing a change of variables, $y = \sigma\eta + y'$, transforms the above to

$$|\Pi_\eta y|^2 \mathrm{tr}\, \hat{h}(y) - [(\hat{h}(y)\cdot \Pi_\eta y)\cdot \Pi_\eta y] = \frac{1}{2}|\Pi_\eta y|^3 F[B_\eta(J^2_\eta f)(x)] \quad \text{for} \quad y \in \mathbb{R}^3. \tag{5.16}$$

Furthermore if we apply (5.5) to the trace free symmetric tensor field $\iota^*_{\eta,s}\tilde{f} - 2\{\mathrm{tr}(\iota^*_{\eta,s}\tilde{f})\cdot\delta\} \in \mathcal{S}(s\eta + \eta^\perp; S^2\eta^\perp_{\mathbb{C}})$, we yield

$$[\tau(\iota^*_{\eta,s}\tilde{f}' - 2\{\mathrm{tr}(\iota^*_{\eta,s}\tilde{f}')\cdot\delta\})](s\eta + y) = \frac{1}{2}|y|^3 F_{\eta^\perp}[B_\eta(I_{\eta,s}(\iota^*_{\eta,s}\tilde{f} - 2\{\mathrm{tr}(\iota^*_{\eta,s}\tilde{f})\cdot\delta\}))] \quad \text{for}\, y \in \eta^\perp. \tag{5.17}$$

Using equation (3.71) of Lemma 3.4 we obtain

$$[\tau(\iota^*_{\eta,s}\tilde{f}' - 2\{\mathrm{tr}(\iota^*_{\eta,s}\tilde{f}')\cdot\delta\})](s\eta + y) = |y|^3 F_{\eta^\perp}[(B_\eta K^2_\eta \tilde{f})(s\eta + x)] \quad \text{for}\, y \in \eta^\perp. \tag{5.18}$$

Remember that $(\tau\delta)(y) = |y|^2 \mathrm{tr}\delta - (\delta(y)\cdot y) = |y|^2$. Hence the LHS of (5.18) becomes

$$[\tau(\iota^*_{\eta,s}\tilde{f}' - 2\{\mathrm{tr}(\iota^*_{\eta,s}\tilde{f}')\cdot\delta\})](s\eta + y) = [\tau(\iota^*_{\eta,s}\tilde{f}') - 2|y|^2 \mathrm{tr}(\iota^*_{\eta,s}\tilde{f}')](s\eta + y) \quad \text{for}\, y \in \eta^\perp. \tag{5.19}$$

Now applying formula (5.3) to the field $\tilde{g} = \iota^*_{\eta,s}\tilde{f} \in \mathcal{S}(s\eta + \eta^\perp; S^2\eta^\perp_{\mathbb{C}})$ gives

$$[\tau(\iota^*_{\eta,s}\tilde{f}')](s\eta + y) = |y|^2\mathrm{tr}(\iota^*_{\eta,s}\tilde{f}') - [\{(\iota^*_{\eta,s}\tilde{f}')(s\eta + y)\cdot y\}\cdot y] \quad \text{for } y \in \eta^\perp. \tag{5.20}$$

It is clear that $((\iota^*_{\eta,s}\tilde{f}')(s\eta + y)\cdot y)\cdot y = (\tilde{f}'(s\eta + y)\cdot y)\cdot y$ by the definition of the slice on the plane. Therefore one may simplify (5.20) to

$$[\tau(\iota^*_{\eta,s}\tilde{f}')](s\eta + y) = |y|^2\mathrm{tr}(\iota^*_{\eta,s}\tilde{f}') - [(\tilde{f}'(s\eta + y)\cdot y)\cdot y] \quad \text{for } y \in \eta^\perp. \tag{5.21}$$

Upon substitution of (5.21) into (5.19) gives

$$[\tau(\iota^*_{\eta,s}\tilde{f}' - 2\{\mathrm{tr}(\iota^*_{\eta,s}\tilde{f}')\cdot\delta\})](s\eta+y) = -|y|^2\mathrm{tr}(\iota^*_{\eta,s}\tilde{f}')](s\eta+y) - [(\tilde{f}'(s\eta+y)\cdot y)\cdot y]. \tag{5.22}$$

We reiterate an argument seen in Section 3.3 where one considers (e_1, e_2), an orthonormal basis of $\eta^\perp$. Of course,

$$0 = \mathrm{tr}\tilde{f}' = [(\tilde{f}'\cdot e_1)\cdot e_1] + [(\tilde{f}'\cdot e_2)\cdot e_2] + [(\tilde{f}'\cdot\eta)\cdot\eta],$$

$$\text{and} \quad \mathrm{tr}(\iota^*_{\eta,s}\tilde{f}') = [(\tilde{f}'\cdot e_1)\cdot e_1] + [(\tilde{f}'\cdot e_2)\cdot e_2]$$

which suggests that $\mathrm{tr}(\iota^*_{\eta,s}\tilde{f}') = -(\tilde{f}'\cdot\eta)\cdot\eta$. In aid of the above we can state the final form of the LHS of (5.18) as

$$[\tau(\iota^*_{\eta,s}\tilde{f}' - 2\{\mathrm{tr}(\iota^*_{\eta,s}\tilde{f}')\cdot\delta\})](s\eta+y) = |y|^2[(\tilde{f}'(s\eta+y)\cdot\eta)\cdot\eta] - [(\tilde{f}'(s\eta+y)\cdot y)\cdot y]. \tag{5.23}$$

This can be substituted into (5.18) giving

$$|y|^2[(\tilde{f}'(s\eta + y)\cdot\eta)\cdot\eta] - [(\tilde{f}'(s\eta + y)\cdot y)\cdot y] = [(B_\eta K^2_\eta\tilde{f})(s\eta + x)] \quad \text{for } y \in \eta^\perp. \tag{5.24}$$

Finally we can follow the steps leading to (5.15) and (5.16) to give

$$|\Pi_\eta y|^2[(\hat{\tilde{f}}(y)\cdot\eta)\cdot\eta] - [(\hat{\tilde{f}}(y)\cdot\Pi_\eta y)\cdot\Pi_\eta y] = |\Pi_\eta y|^3 F[(B_\eta K^2_\eta\tilde{f})(x)] \quad \text{for } y \in \mathbb{R}^3 \tag{5.25}$$

The results of this section are summarized in the following lemma.

Lemma 5.1 *Let* $\widehat{f}, \hat{\tilde{f}}$ *be three-dimensional Fourier transforms of symmetric tensor fields* $f, \hat{\tilde{f}} \in \mathcal{S}(\mathbb{R}^3; S^2\mathbb{C}^3)$ *with the added condition that* $\hat{\tilde{f}}$ *is trace free. For a unit vector* $\eta \in \mathbb{S}^2$*, the following equations hold with the additional condition that* $\widehat{h} \in \mathcal{S}(\mathbb{R}^2; S^2\mathbb{C}^2)$*, is defined to be the two-dimensional adjugate of* f *restricted to the plane*

$$(\widehat{f}(y)\cdot\eta)\cdot\Pi_\eta y = \lambda_\eta(y), \tag{5.26}$$

$$|\pi_\eta y|^2 \operatorname{tr} \hat{h}(y) - [(\hat{h}(y) \cdot \Pi_\eta y) \cdot \Pi_\eta y] = \mu_\eta(y) \quad \textit{and} \tag{5.27}$$

$$|\pi_\eta y|^2 [(\hat{\hat{f}}(y) \cdot \eta) \cdot \eta] - [(\hat{\hat{f}}(y) \cdot \Pi_\eta y) \cdot \Pi_\eta y] = \kappa_\eta(y), \tag{5.28}$$

hold on $\mathbb{R}^3$, *with the right hand sides defined by*

$$\lambda_\eta(y) = \frac{\mathrm{i}}{2} |\Pi_\eta y| F \left[\left(B_\eta \frac{\partial (J^1_\eta f)}{\partial p} \right) (x) \right], \tag{5.29}$$

$$\mu_\eta(y) = \frac{1}{2} |\Pi_\eta y|^3 F[B_\eta (J^2_\eta f)(x)] \quad \textit{and} \tag{5.30}$$

$$\kappa_\eta(y) = |\Pi_\eta y|^3 F[B_\eta (K^2_\eta f)(x)]. \tag{5.31}$$

The partial derivative $\frac{\partial}{\partial p} : \mathcal{S}(\mathbb{R} \times T\mathbb{S}^1_\eta) \to \mathcal{S}(\mathbb{R} \times T\mathbb{S}^1_\eta)$ is defined with the help of the diffeomorphism $\mathbb{R}^2 \times \mathbb{S}^1_\eta \to \mathbb{R} \times \mathbb{R} \times T\mathbb{S}^1_\eta, (s, p, \xi) \mapsto (s, \xi, p\xi \times \eta)$. Given the data $Jf|_{\eta^\perp}$, right-hand sides $\lambda_\eta(y)$ and $\mu_\eta(y)$ of equations (5.26) and (5.27) can be effectively recovered by formulas (5.29) and (5.30). Similarly if we are given the data $Kf|_{\eta^\perp}$, right-hand sides $\lambda_\eta(y)$ and $\kappa_\eta(y)$ of equations (5.26) and (5.28) can be effectively recovered by formulas (5.29) and (5.31).

5.2 Three Axes Explicit Reconstruction Algorithms

Firstly, we derive the reconstruction algorithm for the TRT before moving onto the TTRT. We use the orthonormal basis vectors $\eta_i = e_i$, $i = 1, 2, 3$. Consider the case where $\eta = \eta_1$ for example $\Pi_\eta y = (0, y_2, y_3)$, $\widehat{f} \cdot \eta = (\widehat{f}_{11}, \widehat{f}_{12}, \widehat{f}_{13})$. To abbreviate formulas further, let us denote λ_{η_i} by λ_i and μ_{η_i} as μ_i. With the aid of (5.26) and (5.29), we obtain a system of equations

$$\begin{pmatrix} y_2 & y_3 & 0 \\ y_1 & 0 & y_3 \\ 0 & y_1 & y_2 \end{pmatrix} \begin{pmatrix} \widehat{f}_{12} \\ \widehat{f}_{13} \\ \widehat{f}_{23} \end{pmatrix} = \begin{pmatrix} \lambda_1 \\ \lambda_2 \\ \lambda_3 \end{pmatrix}. \tag{5.32}$$

The system of equations (5.32) can be solved to give

$$\widehat{f}_{12} = \frac{\lambda_1}{2y_2} + \frac{\lambda_2}{2y_1} - \frac{\lambda_3 y_3}{2y_1 y_2}, \tag{5.33}$$

$$\widehat{f}_{13} = \frac{\lambda_1}{2y_3} + \frac{\lambda_3}{2y_1} - \frac{\lambda_2 y_2}{2y_1 y_3} \quad \text{and} \tag{5.34}$$

$$\widehat{f}_{23} = \frac{\lambda_2}{2y_3} + \frac{\lambda_3}{2y_2} - \frac{\lambda_1 y_1}{2y_2 y_3}. \tag{5.35}$$

There is a slight issue with equations (5.33) — (5.35) as they are undefined on coordinate planes giving us $\hat{f}_{ij}|_{\mathbb{R}^3\setminus\Upsilon}(i \neq j)$, where

$$\Upsilon = \{y \in \mathbb{R}^3 \ \mid \ y_1 y_2 y_3 = 0\}.$$

Sharafutdinov calls this an *unstable* reconstruction in [26] due to the division by zero. By continuity, $\hat{f}_{ij}(y)$ can be uniquely determined on the whole of $\mathbb{R}^3$. To implement this numerically requires interpolation by nearby voxels for undefined values. Also we have information outside the boundary since we only consider compactly supported tensor fields. Undoubtedly in the presence of measurement errors in the data, the accuracy in recovering $\hat{f}_{ij}(y)(i \neq j)$ decreases as the point y approaches the surface Υ.

It has been illustrated above that data from three orthogonal axes is sufficient to reconstruct the off-diagonal components of a symmetric rank two tensor field. If we glance back to Section 3.3 of Chapter 3 we note that the axial component is recovered by $(f \cdot \eta_i) \cdot \eta_i$, resulting in the following theorem.

Theorem 5.1 *A symmetric tensor field $f \in \mathcal{S}(\mathbb{R}^3; S^2\mathbb{C}^3)$ is uniquely determined by the data $Jf(\xi, x)$ for $\xi \in \eta_i^{\perp}$, $i = 1, 2, 3$ where (η_1, η_2, η_3) forms an orthogonal basis.*

TTRT Reconstruction Algorithm

Since the recovery of the off-diagonal entries has been shown earlier in Section 5.2, we only require the diagonal components. It can be shown with the aid of (5.28) and (5.31), that

$$\begin{pmatrix} 0 & 2y_2^2 + y_3^2 & y_2^2 + 2y_3^2 \\ 2y_1^2 + y_3^2 & 0 & y_1^2 + 2y_3^2 \\ 2y_1^2 + y_2^2 & y_1^2 + 2y_2^2 & 0 \end{pmatrix} \begin{pmatrix} \hat{\hat{f}}_{11} \\ \hat{\hat{f}}_{22} \\ \hat{\hat{f}}_{33} \end{pmatrix} = \begin{pmatrix} -\kappa_1 - 2y_2 y_3 \hat{\hat{f}}_{23} \\ -\kappa_2 - 2y_1 y_3 \hat{\hat{f}}_{13} \\ -\kappa_3 - 2y_1 y_2 \hat{\hat{f}}_{12} \end{pmatrix}. \tag{5.36}$$

Solving the system of equations (5.36) gives

$$\begin{aligned} \hat{\hat{f}}_{11} = & \frac{y_1^4 \left(\kappa_1 + \lambda_2 y_2 + \lambda_3 y_3\right) + y_1^2 \left(y_2^2 \left(2\kappa_1 - \kappa_2 - 2\kappa_3 + 3\lambda_3 y_3\right)\right)}{6\left(y_1^2 + y_2^2 + y_3^2\right)\left(\left(y_2^2 + y_3^2\right) y_1^2 + y_2^2 y_3^2\right)} \\ & + \frac{y_1^2 \left(+y_3^2 \left(2\kappa_1 - 2\kappa_2 - \kappa_3 + \lambda_3 y_3\right) + \lambda_2 y_2^3 + 3\lambda_2 y_3^2 y_2\right)}{6\left(y_1^2 + y_2^2 + y_3^2\right)\left(\left(y_2^2 + y_3^2\right) y_1^2 + y_2^2 y_3^2\right)} \\ & + \frac{2\left(-y_2^4 \left(\kappa_2 + \lambda_3 y_3\right) + 2y_3^2 y_2^2 \left(\kappa_1 - \kappa_2 - \kappa_3 + \lambda_3 y_3\right) + y_3^4 \left(\lambda_3 y_3 - \kappa_3\right)\right)}{6\left(y_1^2 + y_2^2 + y_3^2\right)\left(\left(y_2^2 + y_3^2\right) y_1^2 + y_2^2 y_3^2\right)} \end{aligned}$$

$$+\frac{2\left(\lambda_2 y_2^5+2\lambda_2 y_3^2 y_2^3-\lambda_2 y_3^4 y_2\right)}{6\left(y_1^2+y_2^2+y_3^2\right)\left(\left(y_2^2+y_3^2\right)y_1^2+y_2^2y_3^2\right)}$$

$$-\frac{5\lambda_1\left(y_2^2+y_3^2\right)y_1^3-2\lambda_1\left(y_2^4+6y_3^2y_2^2+y_3^4\right)y_1-\lambda_1 y_1^5}{6\left(y_1^2+y_2^2+y_3^2\right)\left(\left(y_2^2+y_3^2\right)y_1^2+y_2^2y_3^2\right)}, \tag{5.37}$$

$$\hat{\tilde{f}}_{22}=\frac{-2y_1^4\left(\kappa_1+\lambda_2y_2+\lambda_3y_3\right)-y_1^2\left(y_2^2\left(\kappa_1-2\kappa_2+2\kappa_3-3\lambda_3y_3\right)\right)}{6\left(y_1^2+y_2^2+y_3^2\right)\left(\left(y_2^2+y_3^2\right)y_1^2+y_2^2y_3^2\right)}$$

$$-\frac{y_1^2\left(4y_3^2\left(\kappa_1-\kappa_2+\kappa_3-\lambda_3y_3\right)+5\lambda_2y_2^3+12\lambda_2y_3^2y_2\right)}{6\left(y_1^2+y_2^2+y_3^2\right)\left(\left(y_2^2+y_3^2\right)y_1^2+y_2^2y_3^2\right)}$$

$$+\frac{y_2^4\left(\kappa_2+\lambda_3y_3\right)+2y_3^4\left(\lambda_3y_3-\kappa_3\right)+y_2^2y_3^2\left(-2\kappa_1+2\kappa_2-\kappa_3+\lambda_3y_3\right)}{6\left(y_1^2+y_2^2+y_3^2\right)\left(\left(y_2^2+y_3^2\right)y_1^2+y_2^2y_3^2\right)}$$

$$+\frac{2\lambda_1y_1^5+\lambda_1\left(y_2^2+4y_3^2\right)y_1^3+\lambda_1\left(y_2^4+3y_3^2y_2^2-2y_3^4\right)y_1}{6\left(y_1^2+y_2^2+y_3^2\right)\left(\left(y_2^2+y_3^2\right)y_1^2+y_2^2y_3^2\right)}$$

$$-\frac{\lambda_2y_2^5-2\lambda_2y_2y_3^4-5\lambda_2y_2^3y_3^2}{6\left(y_1^2+y_2^2+y_3^2\right)\left(\left(y_2^2+y_3^2\right)y_1^2+y_2^2y_3^2\right)} \quad \text{and} \tag{5.38}$$

$$\hat{\tilde{f}}_{33}=\frac{-2y_1^4\left(\kappa_1+\lambda_2y_2+\lambda_3y_3\right)+y_1^2\left(-4y_2^2\left(\kappa_1+\kappa_2-\kappa_3+3\lambda_3y_3\right)\right)}{6\left(y_1^2+y_2^2+y_3^2\right)\left(\left(y_2^2+y_3^2\right)y_1^2+y_2^2y_3^2\right)}$$

$$+\frac{y_1^2\left(-y_3^2\left(\kappa_1+2\kappa_2-2\kappa_3+5\lambda_3y_3\right)+4\lambda_2y_2^3+3\lambda_2y_3^2y_2\right)}{6\left(y_1^2+y_2^2+y_3^2\right)\left(\left(y_2^2+y_3^2\right)y_1^2+y_2^2y_3^2\right)}$$

$$-\frac{2y_2^4\left(\kappa_2+\lambda_3y_3\right)-y_2^2y_3^2\left(2\kappa_1+\kappa_2-2\kappa_3+5\lambda_3y_3\right)}{6\left(y_1^2+y_2^2+y_3^2\right)\left(\left(y_2^2+y_3^2\right)y_1^2+y_2^2y_3^2\right)}$$

$$+\frac{y_3^4\left(\kappa_3-\lambda_3y_3\right)+2\lambda_1y_1^5+\lambda_1\left(4y_2^2+y_3^2\right)y_1^3}{6\left(y_1^2+y_2^2+y_3^2\right)\left(\left(y_2^2+y_3^2\right)y_1^2+y_2^2y_3^2\right)}$$

$$+\frac{\lambda_1\left(-2y_2^4+3y_3^2y_2^2+y_3^4\right)y_1+2\lambda_2y_2^5+\lambda_2y_2y_3^4+\lambda_2y_2^3y_3^2}{6\left(y_1^2+y_2^2+y_3^2\right)\left(\left(y_2^2+y_3^2\right)y_1^2+y_2^2y_3^2\right)}. \tag{5.39}$$

Just before Theorem 5.1 we have explained how to deal with such singularities arising in (5.37) — (5.39). Although one may notice that here the condition is $y_1 = y_2 = y_3 = 0$. This gives rise to the following theorem.

Theorem 5.2 *A symmetric trace-free tensor field $\tilde{f} \in \mathcal{S}(\mathbb{R}^3; S^2\mathbb{C}^3)$ is uniquely determined by the data $Kf(\xi, x)$ for $\xi \in \eta_i^\perp$, $i = 1, 2, 3$ where (η_1, η_2, η_3) forms an orthogonal basis.*

5.2.1 Alternative formulae for TRT

While the diagonal components f_{ii} are easily determined as we have seen, there is an alternative more complicated procedure to recover them. As this uses different data it can also be viewed as a compatibility condition on the three axis data.

Consider (5.27) and (5.30). When $\eta = e_1$, we have $\mathrm{tr}\hat{h} = \hat{f}_{22} + \hat{f}_{33}$, and

$$\hat{h} = \begin{pmatrix} 0 & 0 & 0 \\ 0 & \hat{f}_{33} & -\hat{f}_{23} \\ 0 & -\hat{f}_{23} & \hat{f}_{22} \end{pmatrix}.$$

In the same manner as above (λ_i), we achieve a system of equations for μ_i

$$\begin{aligned} (y_2^2 + y_3^2)(\hat{f}_{22} + \hat{f}_{33}) - (y_2^2\hat{f}_{33} - 2y_2y_3\hat{f}_{23} + y_3^2\hat{f}_{22}) &= \mu_1, \\ (y_1^2 + y_3^2)(\hat{f}_{11} + \hat{f}_{33}) - (y_1^2\hat{f}_{33} - 2y_1y_3\hat{f}_{13} + y_3^2\hat{f}_{11}) &= \mu_2, \\ (y_1^2 + y_2^2)(\hat{f}_{11} + \hat{f}_{22}) - (y_1^2\hat{f}_{22} - 2y_1y_2\hat{f}_{12} + y_2^2\hat{f}_{11}) &= \mu_3. \end{aligned} \tag{5.40}$$

Rearranging the above gives the following

$$\begin{pmatrix} 0 & y_2^2 & y_3^2 \\ y_1^2 & 0 & y_3^2 \\ y_1^2 & y_2^2 & 0 \end{pmatrix} \begin{pmatrix} \hat{f}_{11} \\ \hat{f}_{22} \\ \hat{f}_{33} \end{pmatrix} = \begin{pmatrix} \mu_1 - 2y_2y_3\hat{f}_{23} \\ \mu_2 - 2y_1y_3\hat{f}_{13} \\ \mu_3 - 2y_1y_2\hat{f}_{12} \end{pmatrix}. \tag{5.41}$$

Let us relabel the RHS of the above as

$$\begin{pmatrix} \mu_1 - 2y_2y_3\hat{f}_{23} \\ \mu_2 - 2y_1y_3\hat{f}_{13} \\ \mu_3 - 2y_1y_2\hat{f}_{12} \end{pmatrix} = \begin{pmatrix} \nu_1 \\ \nu_2 \\ \nu_3 \end{pmatrix}. \tag{5.42}$$

In this way the solution of (5.41) can be written as

$$\begin{aligned} \hat{f}_{11} &= \frac{1}{2y_1^2}(\nu_2 + \nu_3 - \nu_1), \\ \hat{f}_{22} &= \frac{1}{2y_2^2}(\nu_1 + \nu_3 - \nu_2), \\ \hat{f}_{33} &= \frac{1}{2y_3^2}(\nu_2 + \nu_1 - \nu_3). \end{aligned} \tag{5.43}$$

Upon substitution of the off-diagonals and μ's into (5.43), we obtain

$$\begin{aligned} \hat{f}_{11} &= \frac{1}{2y_1^2}(\mu_2 + \mu_3 - \mu_1 + y_2\lambda_2 + y_3\lambda_3 - 3y_1\lambda_1), \\ \hat{f}_{22} &= \frac{1}{2y_2^2}(\mu_1 + \mu_3 - \mu_2 + y_1\lambda_1 + y_3\lambda_3 - 3y_2\lambda_2), \\ \hat{f}_{33} &= \frac{1}{2y_3^2}(\mu_2 + \mu_1 - \mu_3 + y_2\lambda_2 + y_1\lambda_1 - 3y_3\lambda_3). \end{aligned} \tag{5.44}$$

5.2.2 Two Axes Algorithms

To reduce the data acquisition time, experimentalists would want to rotate the specimen about as few axes as possible. We show that in the general case two orthogonal axes are insufficient by considering components in the null space of the TRT. Thus $J_\eta f = 0$. If we had two orthogonal axes, say $\eta = e_1, e_2$, then $\eta \cdot (J_\eta f \cdot \eta) = 0$. This implies that $f_{11} = f_{22} = 0$. From the definition of $\lambda_\eta(y)$ and $\mu_\eta(y)$, $\lambda_1 = \lambda_2 = 0$ and $\mu_1 = \mu_2 = 0$. The system of equations for the off-diagonals (5.32) gives us

$$y_2\hat{f}_{12} + y_3\hat{f}_{13} = \lambda_1 = 0, \tag{5.45}$$

$$y_1\hat{f}_{12} + y_3\hat{f}_{23} = \lambda_2 = 0. \tag{5.46}$$

Moreover the system of equations corresponding to the other *non-axial* components, (5.42), gives

$$y_2^2\hat{f}_{22} + y_3^2\hat{f}_{33} = \mu_1 - 2y_2y_3\hat{f}_{23}, \tag{5.47}$$

$$y_1^2\hat{f}_{11} + y_3^2\hat{f}_{33} = \mu_2 - 2y_1y_3\hat{f}_{13}. \tag{5.48}$$

We can rearrange (5.48) as

$$y_3^2\hat{f}_{33} = -2y_2y_3\hat{f}_{23}, \tag{5.49}$$

$$y_3^2\hat{f}_{33} = -2y_1y_3\hat{f}_{13}. \tag{5.50}$$

From the above, say $\hat{f}_{33}$ is arbitrary and consequently $\hat{f}_{13}$ and $\hat{f}_{23}$ are determined as

$$\hat{f}_{23} = -\frac{y_3}{2y_2}\hat{f}_{33} \text{ and } \hat{f}_{13} = -\frac{y_3}{2y_1}\hat{f}_{33}. \tag{5.51}$$

Using the values obtained in (5.51) and substituting into (5.46) we can write $\hat{f}_{12}$ as

$$\hat{f}_{12} = \frac{y_3^2}{2y_1y_2}\hat{f}_{33}. \tag{5.52}$$

Thus all the off-diagonal components in the tensor field are determined through $\hat{f}_{33}$ which is arbitrary. Hence two axes are insufficient.

In the potential case $f_{ij} = \partial u_i/\partial x_j + \partial u_j/\partial x_i$ where $u \in \mathcal{S}(\mathbb{R}^3;\mathbb{C}^3)$. This is important for applications in that a linear strain tensor f has this form where u is twice the displacement field. Without loss of generality suppose that data is known only for rotations about $\eta = e_1, e_2$. We have immediately f_{11}, f_{22} and hence by direct integration twice u_1 and u_2. We now also have f_{12} from the partial derivatives of u_1 and u_2. It remains only to find u_3. Multiplying $\hat{f}_{12}$ by $y_1 y_2$ and $\hat{f}_{13}$ by $y_1 y_3$ and adding both of them (5.33) and (5.34) gives

$$y_1 y_2 \hat{f}_{12} + y_1 y_3 \hat{f}_{13} = y_1 \lambda_1. \tag{5.53}$$

This gives us f_{13} in terms of known data and as $\partial u_1/\partial x_3$ is known we have $\partial u_3/\partial x_1$ and hence u_3. We summarise in the theorem

Theorem 5.3 *A potential $f \in \mathcal{S}(\mathbb{R}^3; S^2(\mathbb{C}^3))$ is determined uniquely from $Jf(\xi, x)$ restricted to $\xi \in \eta_1^\perp \cup \eta_2^\perp$ where η_1 and η_2 are orthogonal.*

This result is of considerable practical importance as it means that stain tensors, in a scheme such as that envisaged in [27], can be recovered from rotations about only two axes. We now show that in general a potential f cannot be recovered uniquely from a one-axis rotation by constructing a general element of the null space. Suppose we rotate only about e_1 we have immediately $f_{11} = 0$ and as $\hat{f}_{ij} = y_i \hat{u}_j + y_j \hat{u}_i$ we see $u_1 = 0$. Now as λ_1 and u_1 are zero

$$y_2 \hat{u}_2 + y_3 \hat{u}_3 = \frac{(\lambda_1 - (y_2^2 + y_3^2)\hat{u}_1)}{y_1} = 0. \tag{5.54}$$

and as $\mu_1 = 0$

$$y_2 \hat{u}_2 + y_3 \hat{u}_3 = \frac{\mu_1}{2(y_2^2 + y_3^2)} = 0, \tag{5.55}$$

giving no new information. So u must satisfy $u_1 = 0$ and $\partial u_2/\partial x_2 + \partial u_3/\partial x_3 = 0$. For example if u_2 is arbitrarily specified, then

$$u_3 = -\int\limits_{-\infty} \frac{\partial u_2}{\partial x_2} \, \mathrm{d}x_3. \tag{5.56}$$

For further results of inversion procedures involving the TTRT, one can consult [46]. Now we are in a position to explain how to numerically implement such schemes.

5.3 Forward model

As the process of numerically implementing both algorithms for the TRT and the TTRT is well-nigh, we treat both cases concurrently. In order to simulate data sets, we need to implement a discretized version of the operator J and K described in

(3.35) and (3.49) as a matrix that will approximate integrals of projections and act upon discretized strain fields represented by vectors of values on a grid of voxels. Instead of calculating the whole matrix at once, we generate it one row at a time (*on the fly*) which corresponds to one individual source-detector pair for one of the three components in $P_\xi f$ described by (3.36). On the other hand it can be clearly seen for the case of $Q_\xi f$ that we have only two components shown in (3.50).

5.3.1 Discrete representation of the tensor field

The discretized tensor field is stored as a $6N^3$ vector, containing the 6 distinct values of the symmetric (trace-free) second rank tensor field for each voxel in a $N \times N \times N$ voxel grid. We increment first by the tensor component number, then the position x_1, x_2 and finally x_3. We precisely describe several test phantoms in Section 5.4. Furthermore, the data simulated for the TRT is represented by a $3 \times n_\theta \times h \times w \times 3$ five-dimensional array, where we use three rotation axes ($\eta = e_1, e_2$ and e_3), n_θ angles steps for tomographic acquisition around each axis and a $h \times w$ pixel grid where h is the number of two-dimensional slices which have w detectors. The factor of 3 is the number of independent values of Jf in (3.36) which we integrate along each ray. Obviously due to the constraint imposed by the TTRT, the data simulated is a $3 \times n_\theta \times h \times w \times 2$ five-dimensional array. The factor of 2 is the number of independent values of Kf in (3.50).

5.3.2 Methodology

We simulate an experimental setup with parallel rays passing through a specimen. Sources and detectors consist of arrays in an equally spaced grid, either side of the object being scanned. The source-detector pair is kept fixed and the object is rotated. This is the ideal case both for x-ray/neutron diffraction imaging and for polarized light tomography. We follow the procedure by [42] in a form revised by [20] to calculate the approximate integral along a line through a voxel grid which considers the intersection length of lines with cubical voxels. Such a process has been significantly explained in Section 2.2. This will give us the contribution of each voxel to the total integral for a given ray. For a given tensor we need to calculate the projection on to the plane perpendicular to the ray to emulate P_ξ. Something similar has to be done for Q_ξ also. For the TRT, the axial component $[\eta \cdot (Jf(\xi, x) \cdot \eta)]$ and the non axial component $[(\xi \times \eta) \cdot (Jf(\xi, x) \cdot \eta)]$ are extracted to be used in the approximation of the integral. In this thesis we disregard the reconstruction using the other non-axial component $[\zeta \cdot (Jf(\xi, x) \cdot \zeta)]$. Similarly for the TTRT case we extract $[\eta \cdot (Kf(\xi, x) \cdot \eta)]$ and $[(\xi \times \eta) \cdot (Kf(\xi, x) \cdot \eta)]$.

Now that the contribution of each voxel to the integral is known and by using the length of intersection of the ray with the voxel from ray tracing, we can form the sum of these intersection lengths with the voxel values to form the approximate integral. For our numerical experiments, phantoms were generated inside an $N = 90$ cubic voxel grid and measurements were simulated for a source/detector grid with 90×120 pixels (i.e. $h = 90$ and $w = 120$). We reconstruct on a 90 cubic voxel grid. For each of the three rotation axes, the specimen is rotated through 180° in 1° increments, thus a total of 540 views. Indeed we have committed an inverse crime howbeit the reasoning for this is left to Section 5.6.

5.4 Generating phantoms

We generate three different phantoms or test fields where two of the three only have smooth features and is expected to be less sensitive to algorithmic instabilities. The third phantom has jump discontinuities and is designed to highlight the limitations of the explicit reconstruction algorithm for discontinuous strain fields.

The smooth phantoms are constructed from smooth Gaussian functions, which should be relatively easy to reconstruct. We define a cubic domain $[-1, 1]^3$ on which the components of f are supported, defined by 3-dimensional Gaussians $b_\alpha(x)$ for each of the components f_{ij} according to Tables 5.1 - 5.2, where

$$b_\alpha(x) = \alpha \exp(-50|x - a|^2).$$

Additionally the trace is removed from the phantom described in Table 5.2, as this will be used for TTRT numerics. Our third phantom has jump discontinuities which we expect to be more challenging for the algorithms derived in Section 5.2. This is due to the magnitude of high frequency terms in the Fourier transform which are explicitly

Table 5.1: Phantom 1 - Smooth

f_{ij}	α	a_1	a_2	a_3
f_{11}	-1	-0.5	-0.5	-0.5
	1	-0.5	0.5	-0.5
	-1	-0.5	0.5	0.5
f_{12}	1	0.5	-0.5	0.5
	-1	0.5	0.5	-0.5
f_{13}	1	-0.5	-0.5	-0.5
	-1	-0.5	-0.5	0.5
	1	-0.5	0.5	0.5
f_{22}	-1	0.5	-0.5	-0.5
	1	0.5	0.5	0.5
	-1	0.5	0.5	0.5
f_{23}	1	-0.5	-0.5	0.5
	-1	-0.5	0.5	-0.5
f_{33}	1	0.5	-0.5	-0.5
	-1	0.5	-0.5	0.5
	1	0.5	0.5	0.5

Table 5.2: Phantom 2 - Smooth

f_{ij}	α	a_1	a_2	a_3
f_{11}	1	-0.5	-0.5	-0.5
f_{12}	1	-0.5	-0.5	0.5
f_{13}	1	-0.5	0.5	-0.5
f_{22}	1	-0.5	0.5	0.5
f_{23}	1	0.5	-0.5	-0.5
f_{33}	1	0.5	-0.5	0.5

Table 5.3: Phantom 3 - Sharp

i	j	I_1	I_2	I_3
1	1	[-0.4,0.4]	[-0.6,0.2]	[-0,8,0.8]
1	2	[-0.4,0.4]	[-0.2,0.6]	[-0.8,0.8]
1	3	[-0.8,0.8]	[-0.4,0.4]	[-0.6,0.2]
2	2	[-0.8,0.8]	[-0.4,0.4]	[-0.2,0.6]
2	3	[-0.6,0.2]	[-0.8,0.8]	[-0.4,0.4]
3	3	[-0.2,0.6]	[-0.8,0.8]	[-0.4,0.4]

stated in formulas such as (5.37) — (5.38) and (5.33) — (5.35). As in the smooth case, we define f on the cube $[-1,1]^3$, but set f_{ij} to be the characteristic function of $I_1 \times I_2 \times I_3$, according to Table 5.3.

5.5 Reconstruction procedure

For the TRT case, the recovery of *axial* components is relatively straight-forward as this is just plane-by-plane Radon inversion. We apply a ramp-filter to the data using a one-dimensional discrete Fourier transform and backproject to achieve the diagonal entries for each rotation axis. Such a procedure is outlined in Section 2.3. Errors in high frequency components are amplified by the ramp-filter, thus we regularise the ramp filter by limiting the attenuating high frequencies using a Hamming window defined earlier in (2.36). Since backprojection is the adjoint operator of ray integration, we reuse the ray tracing code to implement discretized backprojection as the transpose of ray integration.

From (5.29), we see the simulated data values J^1 and K^1 that are collected for each plane need to be differentiated in the p-direction, before any backprojection takes place. The implementation of such a process is done with the aid of a regularised derivative, introduced earlier in Section 2.3.3 where the Hilbert transform was used to reconstruct Radon data. Following on we backproject the differentiated plane by plane data onto the voxel grid and the tangential vector field components (i.e. λ) are calculated using a three dimensional FFT algorithm and application of a *ramp-filter* in frequency space. Then equations (5.33) to (5.35) are used to recover the off-diagonal terms in frequency space. The only exception is the voxel $(y_1, y_2, y_3) = (0, 0, 0)$, where $\hat{f}_{12}, \hat{f}_{13}$ and $\hat{f}_{23}$ are undefined. Here, the value is set using linear interpolation from nearby voxels. To complete our reconstruction, we employ the three dimensional inverse FFT to recover f_{ij}. One important remark here is that we know by definition that our phantoms have compact support. Thus if we pad the Fourier transform before Fourier inversions we should be able to avoid the artefacts arising from such a discontinuity.

We complete the discussion on the procedure for reconstruction by outlining how the diagonal entries are recovered for TTRT data. From (5.31) one realises that we must backproject simulated data values K^2 plane-by-plane before applying the FFT algorithm to shift everything into frequency space. Thereafter equations (5.37) — (5.39) are used to calculate the value of the diagonal terms which are passed onto spatial domain using an inverse FFT. Due to the division by zero we apply the same procedure mentioned above when reconstructing off-diagonal terms to avoid having values that are undefined near the origin.

5.6 Results and summary

In this section we illustrate the results of our implemented reconstructions showing the performance of the algorithm on smooth and discontinuous phantoms. Using the 2−norm error defined in (2.37) we calculate the errors component wise for each

Table 5.4: Relative Errors for TTRT

i	j	ϵ_{ij}
1	1	0.098117
1	2	0.34532
1	3	0.32919
2	2	0.098891
2	3	0.3323
3	3	0.095676

tensor phantom. The relative errors for the reconstruction of a strain tensor (trace-free symmetric rank two tensor - TTRT) are given in Table 5.4. Surprisingly the relative errors for the off-diagonals are large which are affecting the reconstruction of the diagonal entries since $\hat{\hat{f}}_{ii}$ depend on λ_i.

The justification for reconstructing the simulated data with inverse crimes is explained clearly by Sharafutdinov [40] where he mentions that differentiated data does not belong to the range of the Radon transform. This is why the author was encouraged to study the range of the Radon and Longitudinal transform shown in Sections 2.4 and 3.2.4. Such results illustrate that we can commute the ramp-filter with the backprojection operator like BPF inversion for the Radon transform mentioned in Section 2.3.1. Realistically, we have as yet a qualitative reconstruction procedure and the results can be seen in Figures 5.2, 5.3, 5.6 and 5.7. Furthermore, it is important to note that Figures 5.2, 5.3, 5.4 and 5.5 are related to the TRT, whereas Figures 5.6, 5.7, 5.8 and 5.9 are related to the TTRT.

On the other hand, since the diagonal entries for TRT is just plane-by-plane filtered backprojection we illustrate the effect of avoiding inverse crime in Figure 5.1. This portrays the relative error for the diagonal components of the tensor field whilst the noise level is increased. In actual fact the relative errors $\epsilon_{11}, \epsilon_{22}$ and ϵ_{33} are identical (three lines are seen as one) due to the way in which the phantom is generated. Furthermore Figures 5.4, 5.8 and 5.9 show the effect of introducing jump discontinuities in the components of a strain field. This would be the case when some material has a crack resulting in the reconstruction being inaccurate as expected. Many artefacts are also visible.

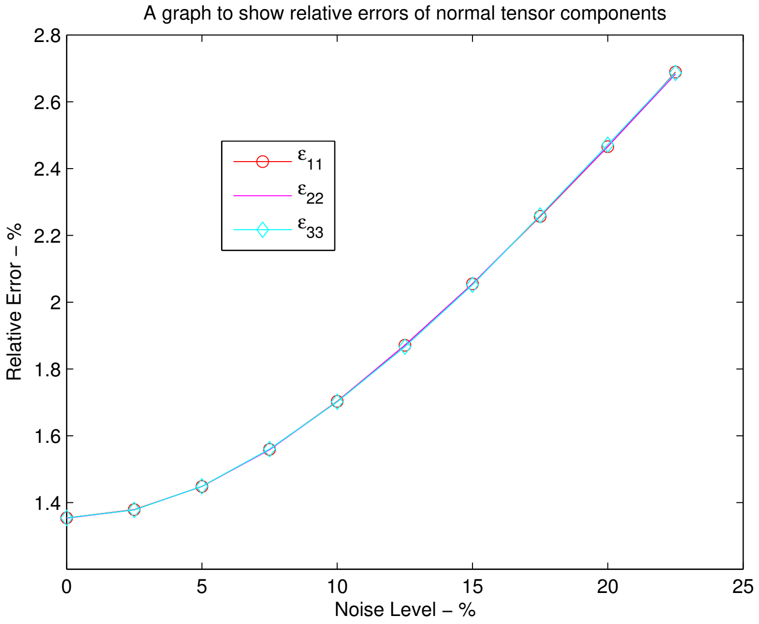

Figure 5.1: Change in ϵ_{jj} when noise is added

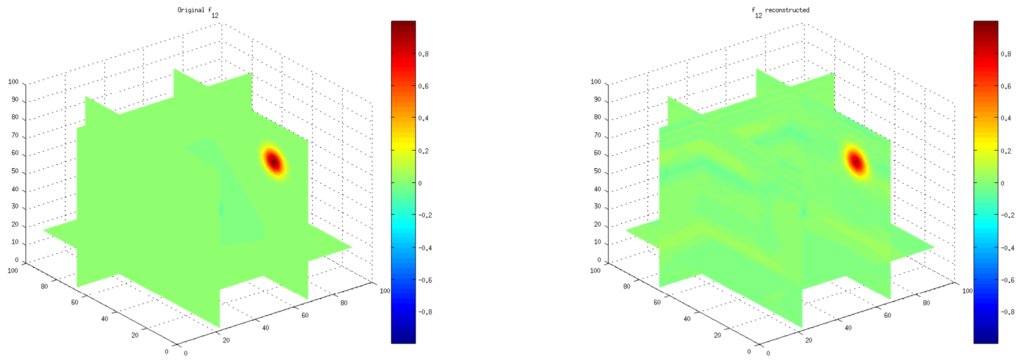

(a) Original f_{12} (b) Reconstruction of f_{12}

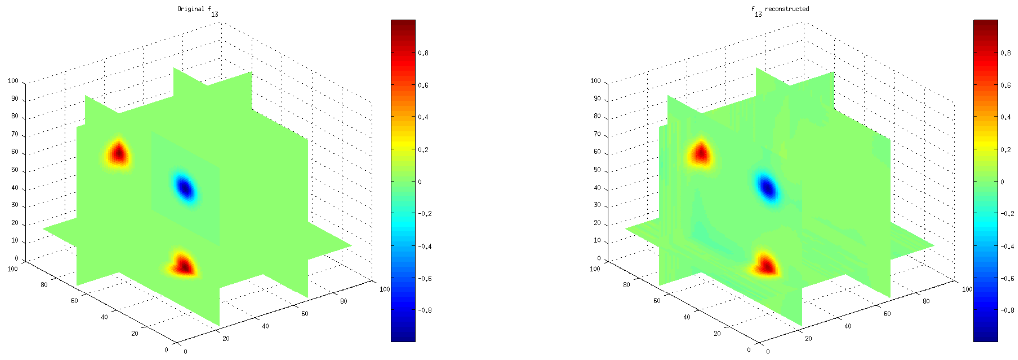

(c) Original f_{13} (d) Reconstruction of f_{13}

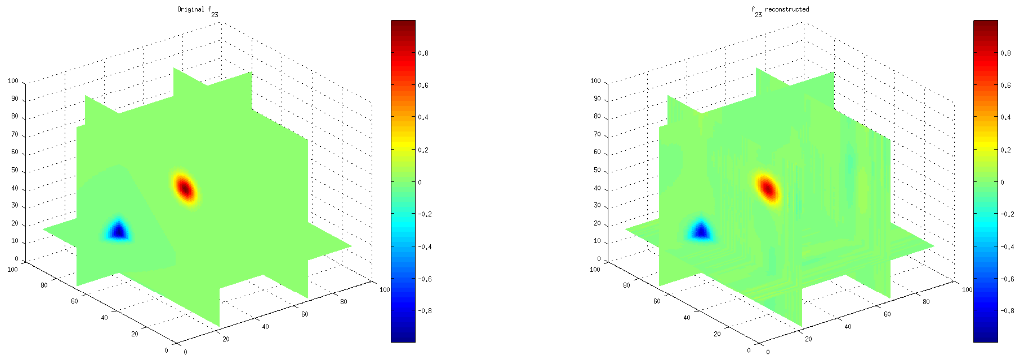

(e) Original f_{23} (f) Reconstruction of f_{23}

Figure 5.2: TRT off diagonals for smooth phantom 1.

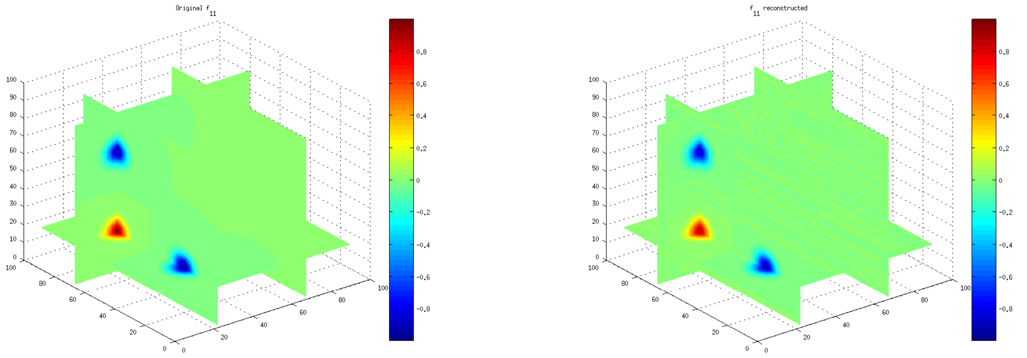

(a) Original f_{11} (b) Reconstruction of f_{11}

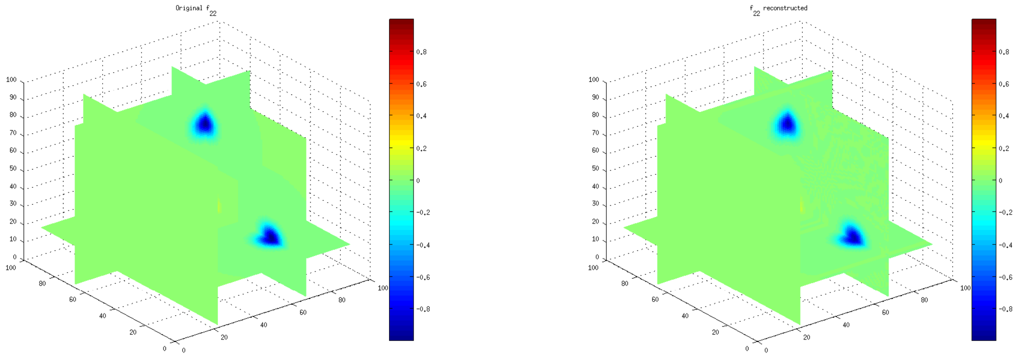

(c) Original f_{22} (d) Reconstruction of f_{22}

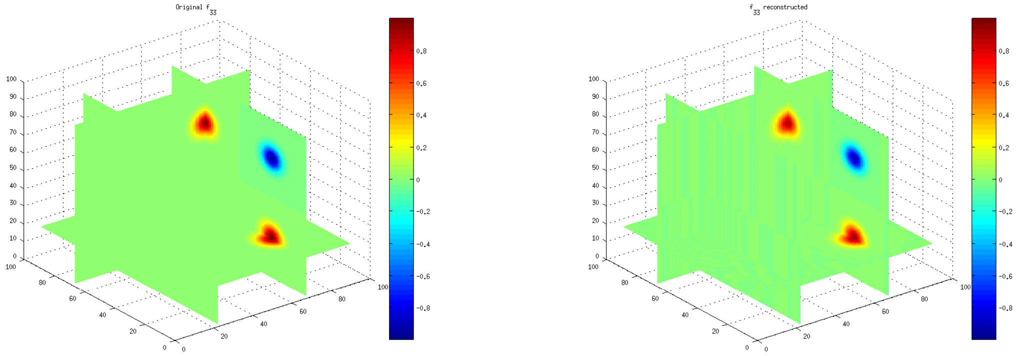

(e) Original f_{33} (f) Reconstruction of f_{33}

Figure 5.3: TRT diagonals for smooth phantom 1.

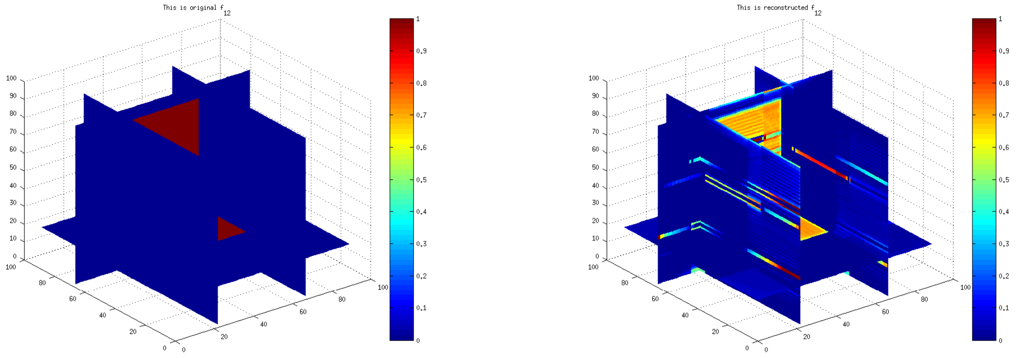

(a) Original f_{12} (b) Reconstruction of f_{12}

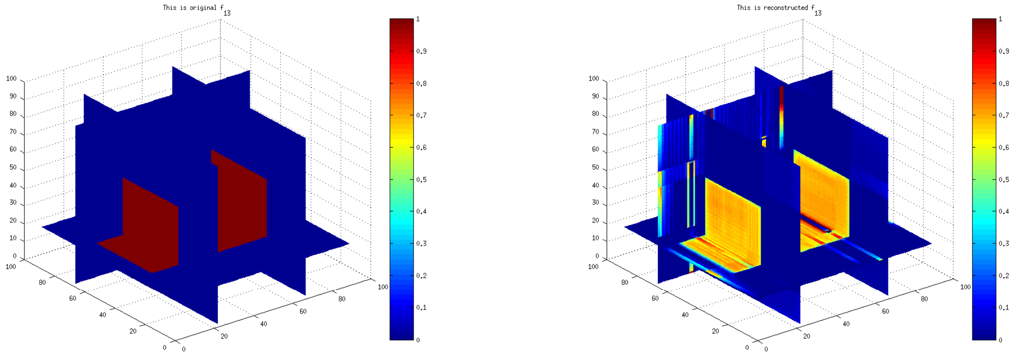

(c) Original f_{13} (d) Reconstruction of f_{13}

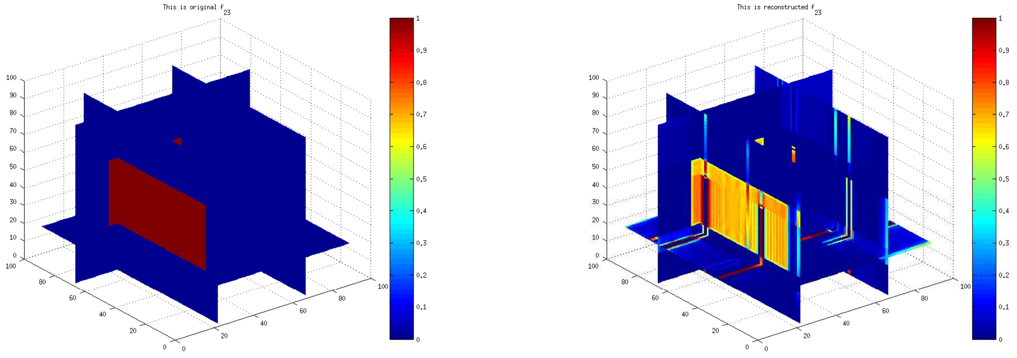

(e) Original f_{23} (f) Reconstruction of f_{23}

Figure 5.4: TRT off diagonals for discontinuous phantom.

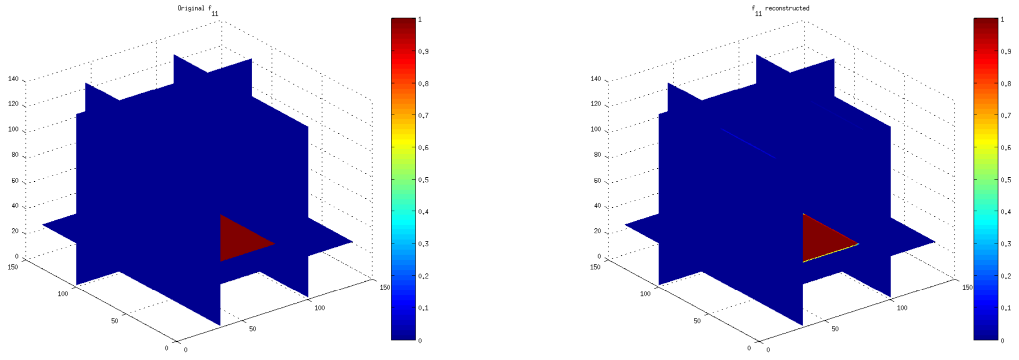

(a) Original f_{11} (b) Reconstruction of f_{11}

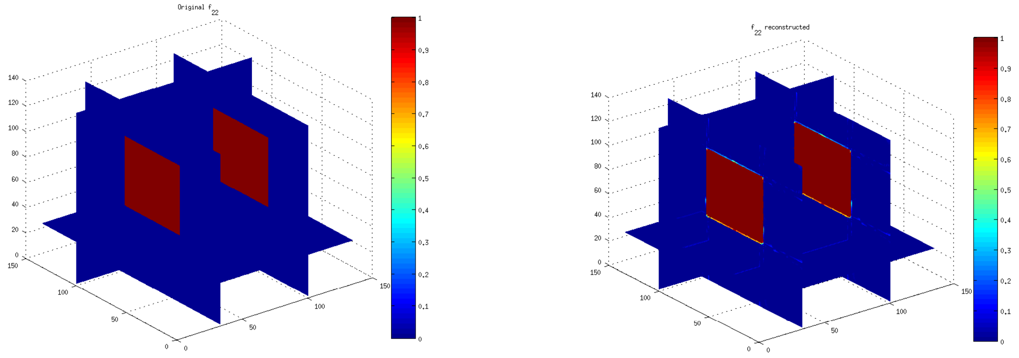

(c) Original f_{22} (d) Reconstruction of f_{22}

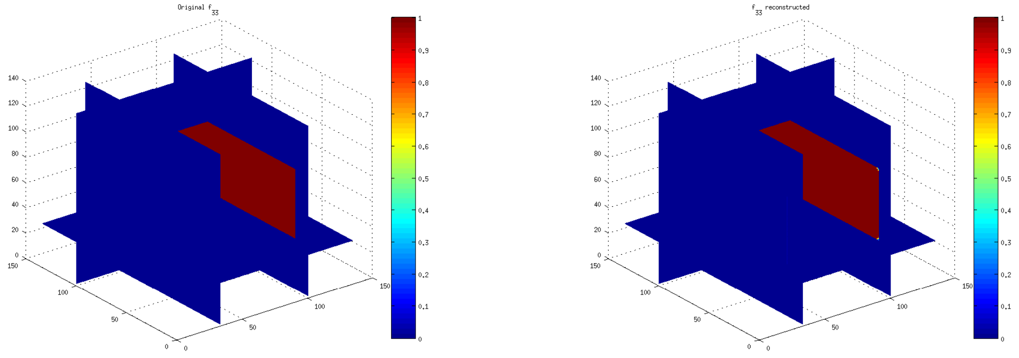

(e) Original f_{33} (f) Reconstruction of f_{33}

Figure 5.5: TRT diagonals for discontinuous phantom.

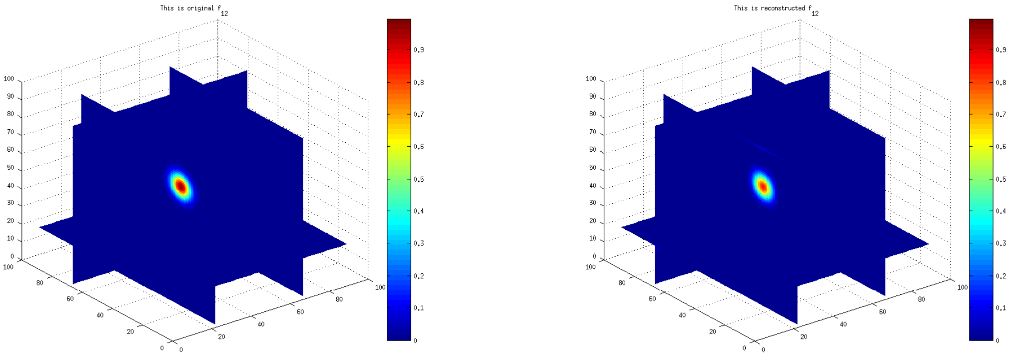

(a) Original $\tilde{f}_{12}$ (b) Reconstruction of $\tilde{f}_{12}$

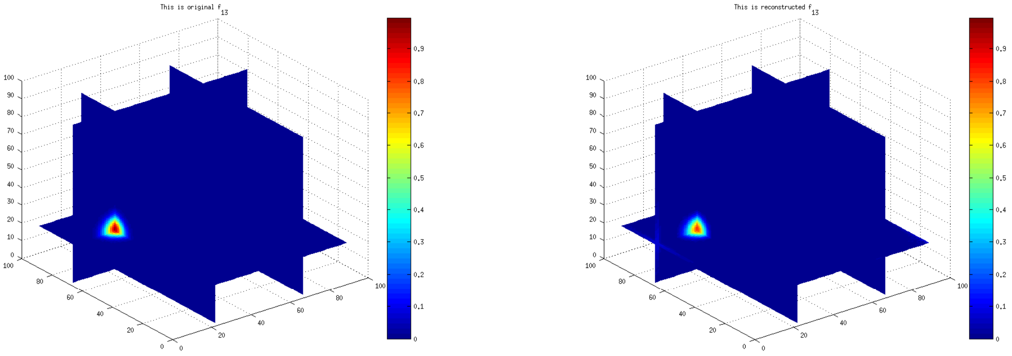

(c) Original $\tilde{f}_{13}$ (d) Reconstruction of $\tilde{f}_{13}$

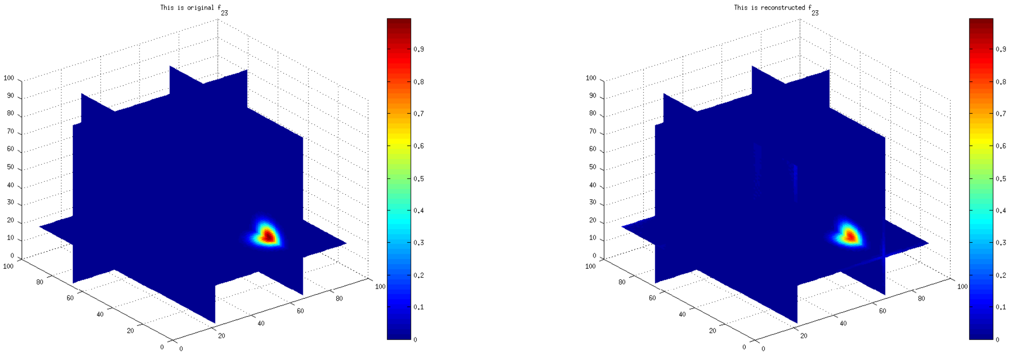

(e) Original $\tilde{f}_{23}$ (f) Reconstruction of $\tilde{f}_{23}$

Figure 5.6: TTRT off diagonals for smooth phantom 2.

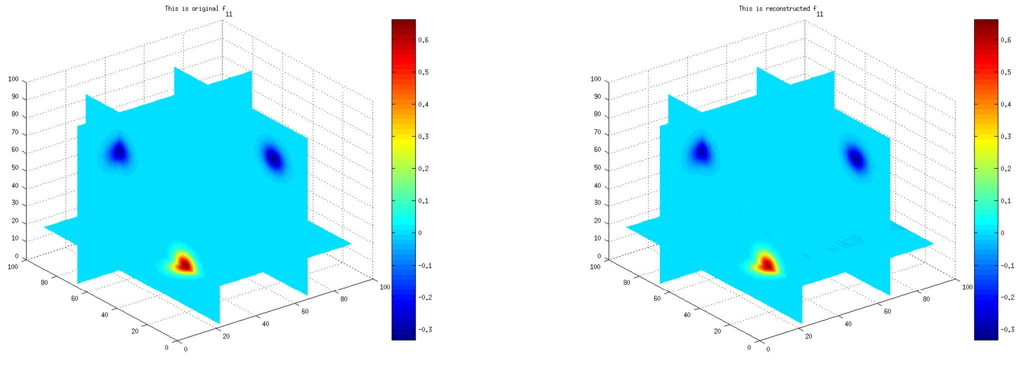

(a) Original $\tilde{f}_{11}$

(b) Reconstruction of $\tilde{f}_{11}$

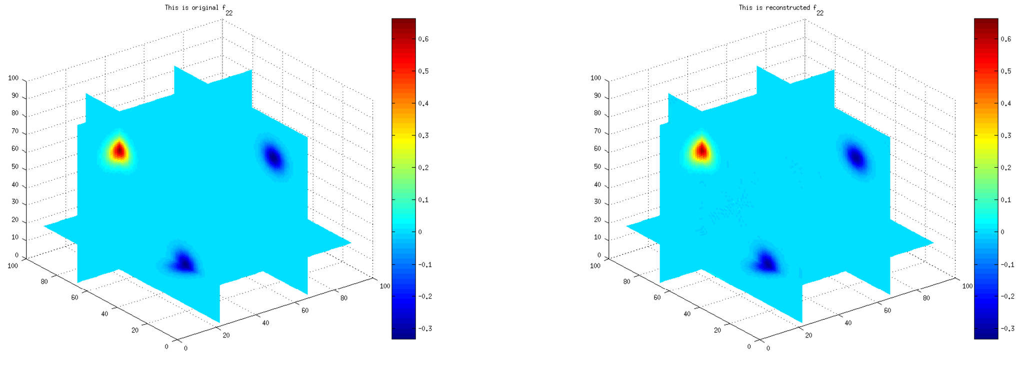

(c) Original $\tilde{f}_{22}$

(d) Reconstruction of $\tilde{f}_{22}$

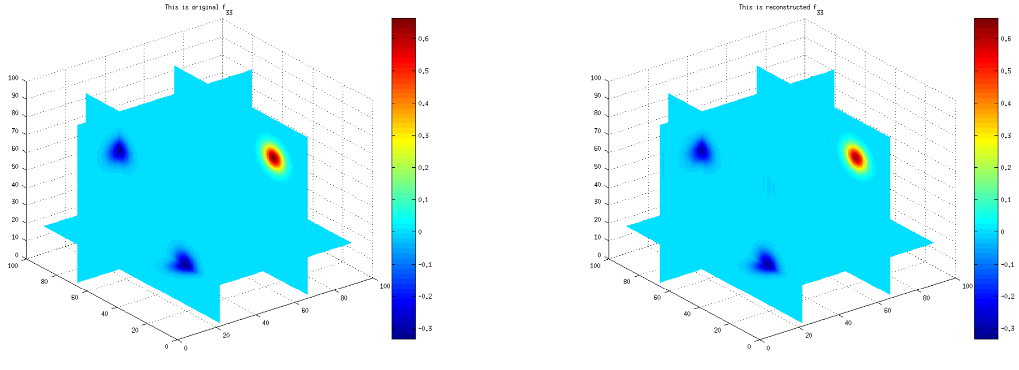

(e) Original $\tilde{f}_{33}$

(f) Reconstruction of $\tilde{f}_{33}$

Figure 5.7: TTRT diagonals for smooth phantom 2.

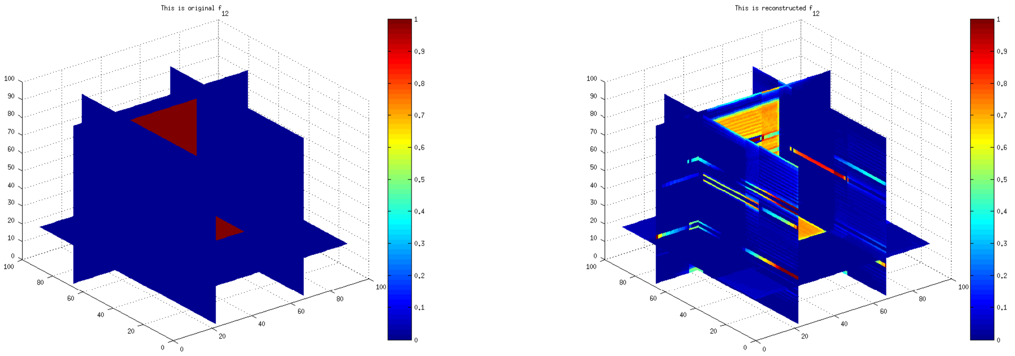

(a) Original $\tilde{f}_{12}$ (b) Reconstruction of $\tilde{f}_{12}$

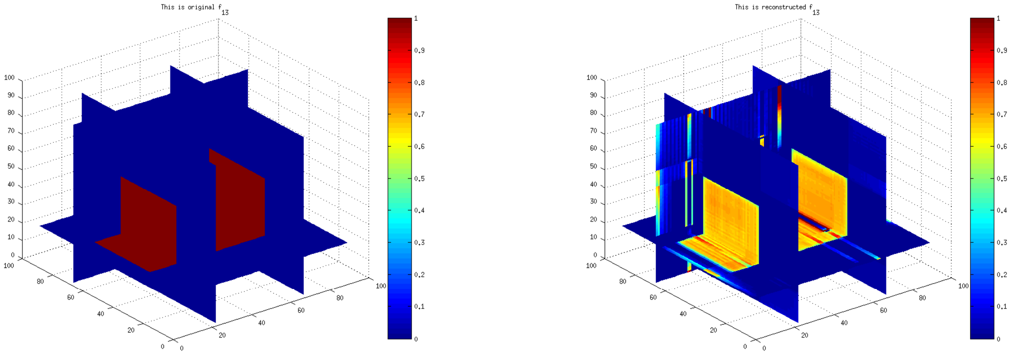

(c) Original $\tilde{f}_{13}$ (d) Reconstruction of $\tilde{f}_{13}$

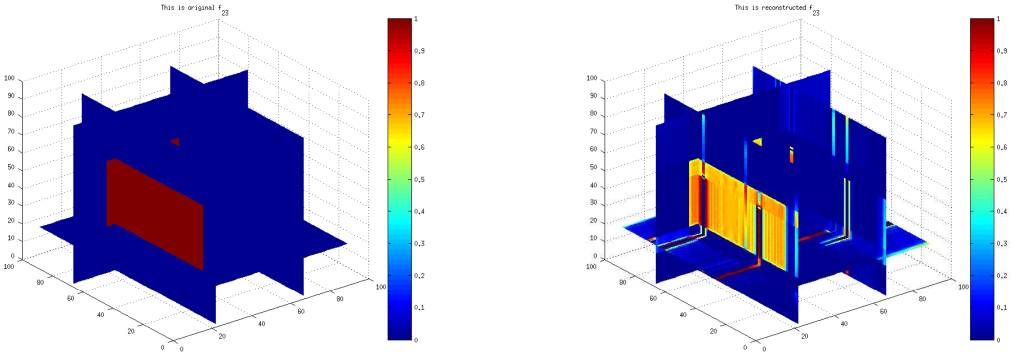

(e) Original $\tilde{f}_{23}$ (f) Reconstruction of $\tilde{f}_{23}$

Figure 5.8: TTRT off diagonals for discontinuous phantom.

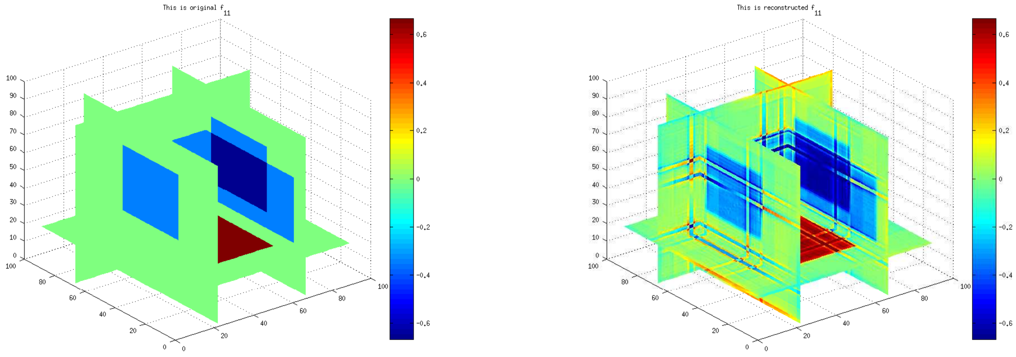

(a) Original $\tilde{f}_{11}$ (b) Reconstruction of $\tilde{f}_{11}$

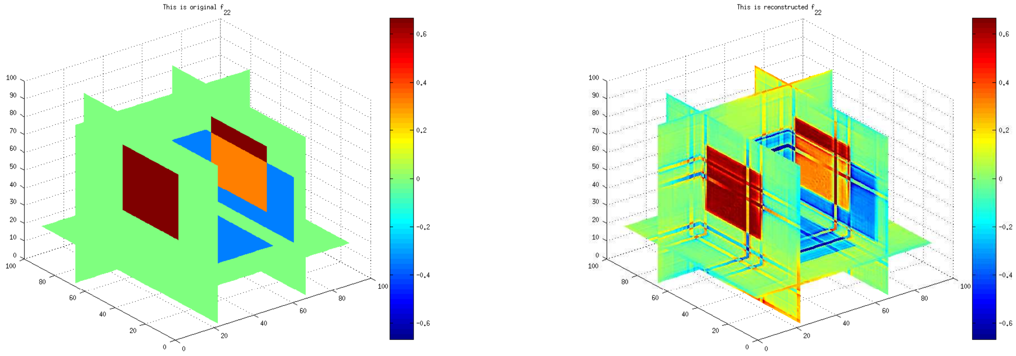

(c) Original $\tilde{f}_{22}$ (d) Reconstruction of $\tilde{f}_{22}$

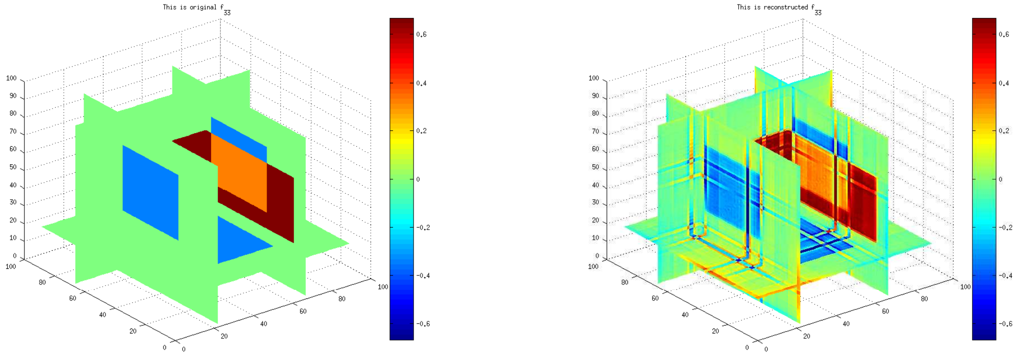

(e) Original $\tilde{f}_{33}$ (f) Reconstruction of $\tilde{f}_{33}$

Figure 5.9: TTRT diagonals for discontinuous phantom.

Chapter 6

Nonlinear Inverse Problems

An inherently more difficult family of inverse problems are collectively referred to as nonlinear inverse problems. Nonlinear inverse problems have a more complex relationship between data and model and in the case of PNMFT the relationship can be represented by the equation $\Sigma = \mathcal{F}(M(B))$. Here $\mathcal{F}$ is a nonlinear operator and cannot be separated to represent a linear mapping of the model parameters that take a magnetic field $M(B)$ into the data Σ. Now suppose we had two magnetic fields, B^1 and B^2, then our problem would only be classed as linear if $\mathcal{F}(\alpha M(B^1) + \beta M(B^2)) = \alpha \mathcal{F}(M(B^1)) + \beta \mathcal{F}(M(B^2))$. Indeed this is not the case as illustrated in Figures 6.1 and 6.2, where we compare the values of each of the nine sinograms in the data set obtained by letting $\alpha = 50$ and $\beta = 150$. Now for this example we take $B^1 = B^2$ and the magnetic field is the central slice of the solenoid utilized in Section 4.1. The cause of this nonlinearity lies within the Physics of the problem. If a single neutron precesses more than 180° we have *phase wrapping* issues. The spin on the neutron depends upon two things; the strength of magnetic field and the time spent by the neutron in the magnetic field. The logarithmic approach outlined in Section 4.2.2 will only recover magnetic fields up to phase wrapping which limits its use. Therefore we have to resort to methods in which we are able to solve nonlinear problems in order to successfully image magnetic structures in magnetic materials.

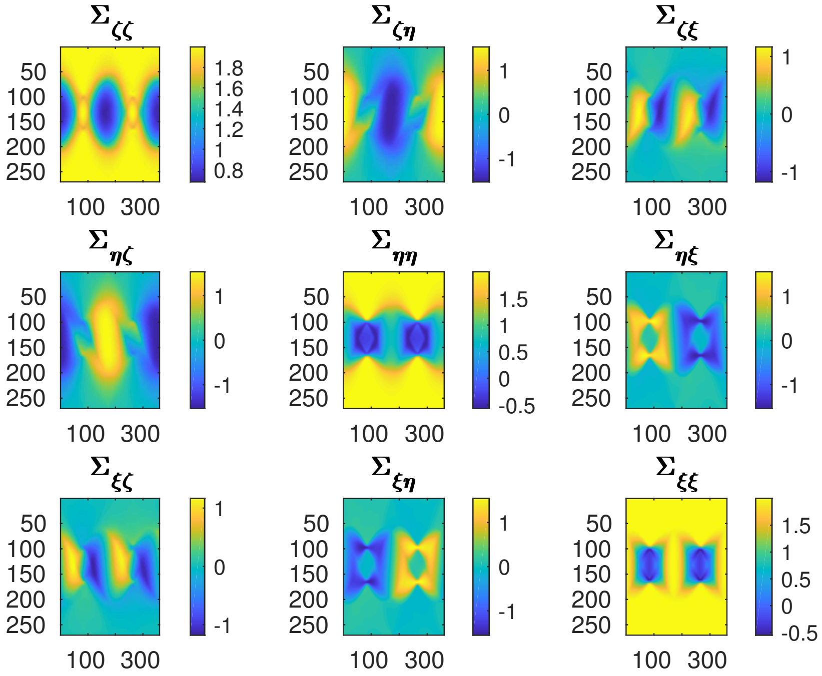

Figure 6.1: Spin Data Σ for $\mathcal{F}(50M(B)) + \mathcal{F}(150M(B))$.

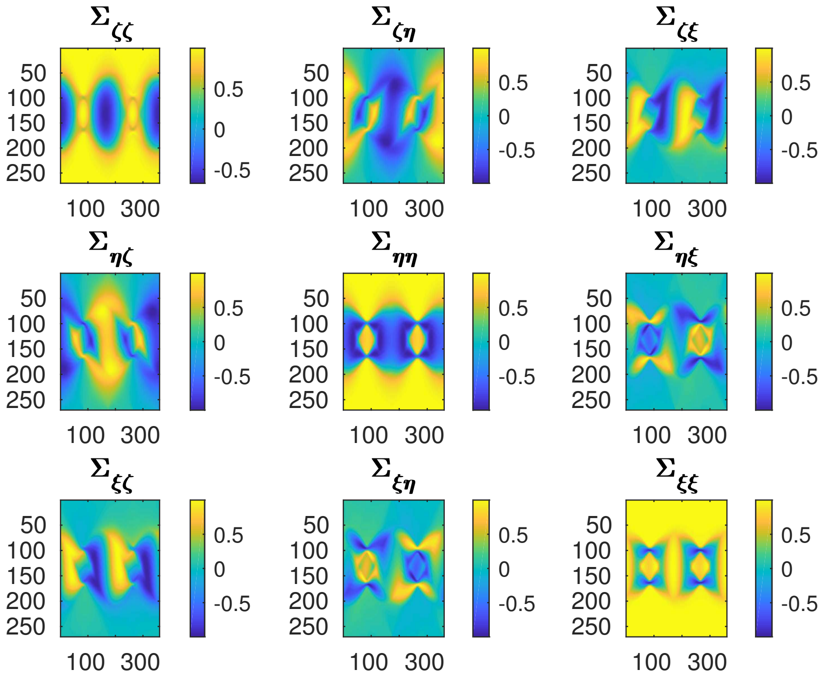

Figure 6.2: Spin Data Σ for $\mathcal{F}(50M(B) + 150M(B)) = \mathcal{F}(200M(B))$.

6.1 Modified Newton Kantarovich Method

Nonlinear inverse problems generally must be solved by either an approximate or iterative method. Usually an approximation is not known in which case the only possibility is an iterative method. One such iterative scheme is the Newton Kantarovich method which was utilized by [6] to solve several applications in which the resulting operator is nonlinear. Such an approach linearises the nonlinear operator equation about a current approximation resulting in a linear operator equation. This is solved to yield an update at each iteration. The Newton Kantarovich method is given by the following scheme

$$B^{n+1} = B^n + \delta B^n, \quad n = 0, 1, 2, ..., \tag{6.1}$$

where B is the magnetic field desired and δB is the update satisfying the linear operator equation

$$\mathcal{F}'(M(B^n))M(\delta B^n) = -\mathcal{F}(M(B^n)). \tag{6.2}$$

However the computational cost of calculating the Fréchet derivative (Jacobian) at every step is high so the Modified Newton Kantarovich Method (MNKM) may also be used. Here the Fréchet derivative is left fixed at the first iterate and the calculation of the update δB^n satisfies

$$\mathcal{F}'(M(B^0))M(\delta B^n) = -\mathcal{F}(M(B^n)). \tag{6.3}$$

A damped MNKM method has a linesearch parameter, α, which controls the extent of the update, given as

$$B^{n+1} = B^n + \alpha\ \delta B^n, \quad n = 0, 1, 2, ... \tag{6.4}$$

One should notice the Fréchet derivative $\mathcal{F}'(B = 0)$ for the problem of PNMFT has been calculated in Section 4.2 as

$$\lim_{t\to\infty} \delta\Sigma(x + t\xi, \xi) = \int_{-\infty}^{\infty} M(\delta B(t))\ \mathrm{d}t.$$

Thus we summarize the MNKM in th efollowing algorithm.

Algorithm 6.1 *(Modified Newton Kantarovich Method) Suppose B is a sufficiently small magnetic field and Σ is PNMFT data, then the iterative procedure converges in that $B^n \to B$, as $n \to \infty$. The procedure is as follows*

i. $B^0 = 0$,

ii. $\delta B_i^n = X^{-1}\left[e_j \cdot [\Sigma - \mathcal{F}(M(B^n))] \cdot e_k\right]$, *iii.* $B^{n+1} = B^n + \alpha(\delta B^n)$,

iv. $n = n + 1$.

A similar approach to the one mentioned in Algorithm 6.1 has been taken by [33] for the nonlinear polarization tomography problem. However this is still a theoretical result and no one has implemented a numerical recipe for such a reconstruction procedure as yet. This implies that a similar approach to the one for PNMFT maybe of use. In essence, the forward model used in the linearized problem will be employed to give a nonlinear update and the inversion procedure will solve the linearized inverse problem.

6.1.1 Drawback of MNKM

In order to test the MNKM the solenoid in Figure 4.2 is scaled up by a factor of 50 which means the magnetic field is of strength 290 μT. Using the forward model mentioned in Section 4.2.1, initial data is generated for the strengthened magnetic field. Thereafter the reconstruction process adopted in the linearized inversion process is utilized to yield the result from the first iterate. This is fed back into the forward model to obtain new data which is subtracted from the initial data to give the data set on which the reconstruction procedure will be employed. Upon completion of Radon inversion, the update, δB, is found. In reality, a linesearch is performed at every step to minimize the difference in data. This is performed by solving the forward problem thrice, each time with a different linesearch parameter, α. To limit the step in which the iterative procedure advances, a quadratic is fitted to the three different linesearch parameters chosen against the residuals obtained. The α value for which the residual is at the minimum, is chosen as the update parameter. The iterative procedure terminates at a predetermined tolerance, $\mathrm{TOL} = 10^{-5}$.

Figure 6.3 shows the results for the iterative reconstruction algorithm mentioned in Algorithm 6.1. The initial spin data was simulated using a 180×180 pixel grid where 270 rays of neutrons (uniform velocity with wavelength = 5 Å) were fired for every angular increment (1 degree in this case) of the usual tomographic data acquisition process. The data is binned by a factor of three to give the data which is three sets of 90×120 arrays. Furthermore, 5% pseudo-random gaussian noise was added. Reconstruction was performed on a grid which does not evenly divide the grid used for simulation, i.e. 67×67. The relative errors are 22%, 17%, 9% and 10% for the magnetic field strength, $|B(x(t))|$ and components $B_1(x(t)), B_2(x(t))$ and $B_3(x(t))$ respectively. It took 25 iterates to converge and the maximum a neutron precesses throughout this specific magnetic field is 88°.

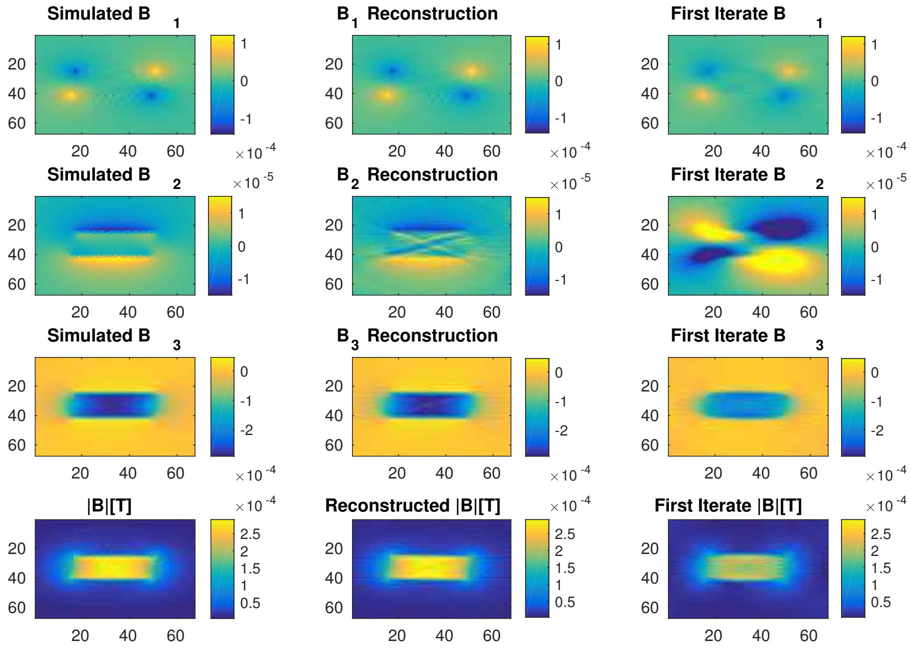

Figure 6.3: Convergence of iterative procedure.

However, one drawback of this method is illustrated when the solenoid in Figure 4.2 is scaled up by a factor of 100 which means the magnetic field is of strength of 580 μT. In this situation the MNKM converges to a wrong solution. Figure 6.4 illustrates this where the most a neutron can precess throughout the magnetic field is 176°. Thus the logarithmic approach is by far the better method since it can reconstruct magnetic fields wherein neutrons precess up to 180°. How then are we going to tackle the phase wrapping issue? Of course, the MNKN only uses the Fréchet derivative (Jacobian) at $B = 0$. Hence we must attempt to calculate the Jacobian at $B \neq 0$ and update it at every step in the iteration process.

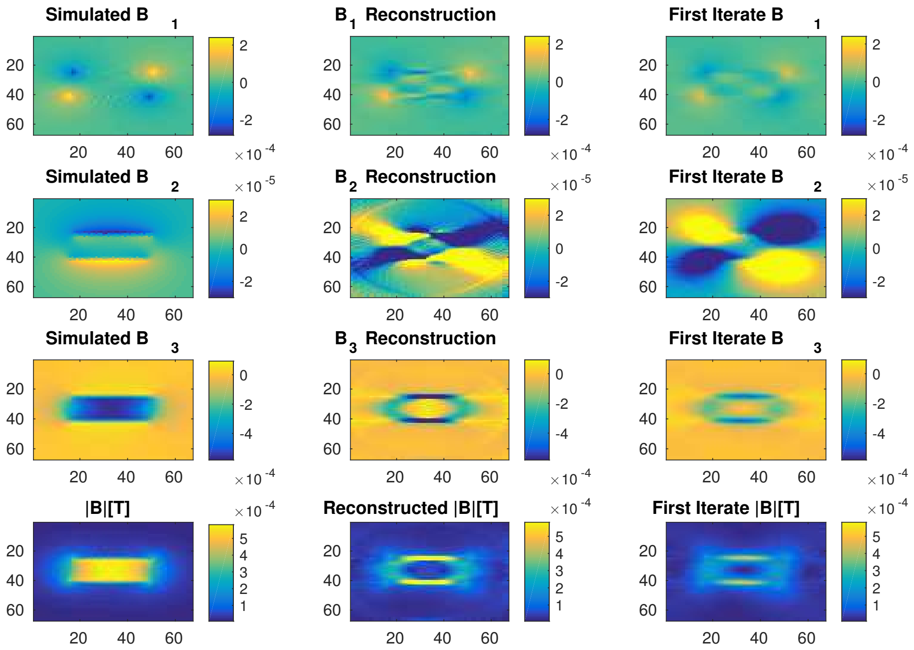

Figure 6.4: Drawback of iterative procedure.

6.2 Jacobian Update

We have already seen in (4.10) of Section 4.2 that for an arbitrary B field the Fréchet derivative can be calculated as

$$D\mathcal{F}(M(B^0))M(\delta B) = \lim_{t\to\infty} \delta\Sigma(x+t\xi,\xi) = \int_{-\infty}^{\infty} S_0(t)M(\delta B(t))\Sigma_0(t)\ \mathrm{dt}.$$

This allows us to update Algorithm 6.1 in the manner described below.

Algorithm 6.2 *(Newton Kantarovich Method) Suppose* B *is a magnetic field and* Σ *is PNMFT data, then the iterative procedure converges in that* $B^n \to B$*, as* $n \to \infty$*. The procedure is as follows*

i. $B^0 = 0,$

ii. $\delta B_i^0 = X^{-1}\left[e_j \cdot \Sigma \cdot e_k\right],$

iii. $B^1 = B^0 + \alpha(\delta B^0),$

iv. $n = 1.$

while $(B^{n+1} - B^n) < TOL$

v. *Calculate Jacobian.*

vi. *Use CGLS for* $\mathcal{F}'(M(B^n))M(\delta B^n) = \mathcal{F}(M(B + \delta B)) - \mathcal{F}(M(B))$.

vii. $B^{n+1} = B^n + \alpha(\delta B^n)$,

viii. $n = n + 1$.

Just a note for practical purposes. Suppose we have a matrix equation of the type $STU = V$, then using the kronecker product, we can rewrite this as

$$(U^T \otimes S)\mathrm{vec}(T) = \ \mathrm{vec}(V),$$

where the vec denotes vectorization of a matrix in the column sense. Thus the update, δB can easily be calculated as

$$\left(\Sigma_0^T \otimes S_0\right) \mathrm{vec}(M(\delta B)) = \mathrm{vec}\left(\mathcal{F}(M(B + \delta B)) - \mathcal{F}(M(B))\right) \tag{6.5}$$

using CGLS, introduced in Section 2.3.2. This provides us with a technique to image stronger magnetic domains but due to time constraints this has yet to implemented numerically. The next step would be to code the Fréchet derivative at $B \neq 0$. From (6.5) above it can be seen that we require an integrating factor, S_0, and the pixel spin data, Σ_0, from the previous iterate in the Newton Kantarovich scheme.

Chapter 7

Conclusions and Future Work

This concludes our investigations of tensor ray transforms, in particular applications such as diffraction strain tomography, photoelasticity and PNMFT. While this thesis comes to completion, this subject is by no means closed. Rather, some would say it is the introduction of methods able to solve rich tomography problems. Nevertheless, here are some of our thoughts and the possible next steps on where we would invest our time and energy, given more time.

We have derived an explicit reconstruction algorithm for three axes data with the application x-ray diffraction tomography in mind. Furthermore, for the first time reconstruction of simulated strain data is given outlining the limitation of the novel *unstable* method. This is outlined by the numerics where a discontinuous phantom was simulated and the algorithm never performed well, with artefacts appearing in the reconstruction. We have pointed out that as there are two distinct methods of calculating the diagonal components this provides a consistency condition on the data. Numerically one would apply a discrete three dimensional FFT to the normal components, as we have seen the reconstructions are quite accurate. Then using the data (μ_i) for the off-diagonals, we could investigate how well the alternative algorithm performs.

Moreover, we have derived that it is not possible to reconstruct a symmetric second rank strain tensor with data from less than three orthogonal axes. Nonetheless it is possible to use only two axes of rotation for the case that is the result of an infinitesimal strain, and recover the displacement field directly. However it might be better in practice to use the general procedure and then verify to what extent the compatibility condition holds on the reconstructed tensor.

The three axes algorithm for the TTRT suffers from similar issues. The reasoning behind such an effect is the off-diagonals for the TRT and TTRT are calculated in exactly the same manner. Quantifying the accuracy of the reconstruction suggests the issue is only in the off-diagonals (i.e. λ_i) since the relative errors are only 9% for the diagonal entries of the strain tensor, whereas the relative errors are approximately 33% for the off-diagonal entries. Surprisingly this is with inverse crimes. This motivated an interesting question, what exactly happens to data when we differentiate or apply a filter. So the range conditions for tensor ray transforms were studied, but this is still an unanswered question. One satisfactory result is the correction of some of the formulae present in David's thesis [46] and correcting the code on the instrumental setup currently in Sheffield.

As for PNMFT, we have an algorithm for reconstructing fairly weak magnetic fields, up to phase wrapping. Even though this is for simulated data, we have seen this is possible for experimental data, [37]. We have acquired a bound for which the MNKM works, namely the correct magnetic field can be retrieved if the angle by which the neutron precesses is under 90°. It is apparent that it works when the linearization fails (i.e. $\sin(x) \neq x$). It is yet an open question as to how Eskin's result (Theorem 3.1) can be shown numerically although this is a step in the right direction. Furthermore we have formulated the Fréchet derivative for $B \neq 0$ and have devised an algorithm to reconstruct magnetic field for data acquired from phase wrapping.

7.1 Further Work

While the system (5.32) can be solved in the frequency domain using a discrete Fourier transform in three dimensions, this is relatively computationally expensive even using the Fast Fourier Transform algorithm. Another method is suggested by multiplying the equations in (5.33), (5.34) and (5.35) by $-y_1y_2$, $-y_1y_3$ and $-y_2y_3$ respectively, and then on taking the inverse Fourier transform, we have

$$\frac{\partial f_{12}^2}{\partial x_1 \partial x_2} = -\frac{1}{2}\left(\frac{\partial \check{\lambda}_1}{\partial x_1} + \frac{\partial \check{\lambda}_2}{\partial x_2} - \frac{\partial \check{\lambda}_3}{\partial x_3}\right) \tag{7.1}$$

$$\frac{\partial f_{13}^2}{\partial y_1 \partial y_3} = -\frac{1}{2}\left(\frac{\partial \check{\lambda}_1}{\partial x_1} + \frac{\partial \check{\lambda}_3}{\partial x_3} - \frac{\partial \check{\lambda}_2}{\partial x_2}\right) \tag{7.2}$$

$$\frac{\partial f_{32}^2}{\partial y_3 \partial x_2} = -\frac{1}{2}\left(\frac{\partial \check{\lambda}_3}{\partial x_3} + \frac{\partial \check{\lambda}_2}{\partial x_2} - \frac{\partial \check{\lambda}_1}{\partial x_1}\right). \tag{7.3}$$

The right hand side terms can be calculated directly using a finite difference scheme and then numerical quadrature used to calculate the f_{ij}. Here $\check{\lambda}_i$ is the three dimensional inverse Fourier transform of λ_i. Notice that λ_i consists of the slice by slice data $J^1_{e_i}$ (off-diagonal), which is differentiated in the p variable, the projection coordinate in each plane, backprojected slice by slice and ramp filtered in each plane. This means that the data used in (7.3) is subjected to standard slice by slice back projection and filter operations that are commonly implemented in parallel beam x-ray CT reconstruction. The derivatives $\partial\check{\lambda}_i/\partial x_i$ are not local to the plane but numerical implementation would involve data only from near-by planes.

An alternative approach would be to try different modified ramp filters or explicit regularization methods such as total variation. Another avenue worth considering on the practical side is to develop a reconstruction algorithm involving general (non-orthonormal) axes. In experiments it is often not feasible to rotate the specimen through 90° and remain in the field of view of the measurement system. Explicit reconstruction algorithms such as the one we have given are useful practically for data that is complete and uniformly sampled. For partial, sparse or irregularly sampled data representing the forward problem simply as a sparse matrix and solving using iterative algorithms (like CGLS) with explicit regularization is generally better, although typically requiring large amounts of memory and parallel processors.

From earlier work in Section 2.3.3, it was shown that reconstruction for a volume is possible slice by slice. This approach can be applied to PNMFT data to give a three dimensional reconstruction of a magnetic field. Ideally a robust reconstruction algorithm is required which can take care of phase wrapping issues when dealing with strong domains in close proximity of $1T$. This is what experimentalists would like since this would certainly be a breakthrough in the neutron imaging community. With confidence the aforementioned statement can be written since the author presented this novel idea on the occasion of ICTMS 2017, in Lund, Sweden. The attentiveness and delight of the audience, majority of whom were neutron imaging scientists, was amazing as they showed great enthusiasm during the talk.

Ultimately for application purposes, e.g. quantum mechanical effects in superconductors and imaging electromagnetic devices, a further advancement is required. More often than not, the magnetic materials that we would like to image are composed of several discontinuous domains which largely affect the spin on the polarized neutron. To derive an innovative reconstruction algorithm for such a problem would really advance the field. The nonlinear inverse problem for PNMFT can be regarded as a warm up exercise for other nonlinear problems. Intuitively, the nonlinear polarized light problem involving the TRT and measuring the absolute phase change of polarized light will become conceptually easier to understand, if this is solved. Hence benefiting a whole new spectrum of applications.

Bibliography

[1] Keller, j.b. *Am. Math. Monthly*, 83:107, 1976.

[2] H. Aben, L. Errapart, L. Ainola, and J. Anton. Photoelastic tomography for residual stress measurement in glass. *Optical Engineering*, 44(9), 2006.

[3] V. Ambartsumian. Über eine Frage der Eigenwerttheorie. *Zeitschrift für Physik*, 53:690–695, 1929.

[4] A. Beer. Bestimmung der Absorption des rothen Lichts in farbigen Flssigkeiten (determination of the absorption of red light in colored liquids). *Annalen der Physik und Chemie*, 86:78–88, 1852.

[5] M. Bertero and P. Boccacci. *Introduction To Inverse Problems in Imaging.* IOP Publishing Ltd, 1998.

[6] T.J. Connolly. *Nonlinear methods for Inverse Problems.* PhD thesis, University of Canterbury, Christchurch, New Zealand, 8 1989.

[7] M. Dawson, I. Manke, N. Kardjilov, A. Hilger, M. Strobl, and Banhart J. Imaging with polarized Neutrons. *New Journal of Physics*, 11, 2009.

[8] E.Y. Derevtsov, A.V. Efimov, A.K. Louis, and T Schuster. Singular value decomposition and its application to numerical inversion for ray transforms in 2D vector tomography. *Journal of Inverse and Ill-posed Problems*, 9:689–715, 2011.

[9] E.Y. Derevtsov and A.P. Polyakova. Solution of the Integral Geometry Problem for 2-Tensor Fields by the Singular Value Decomposition Method. *Journal of Mathematical Sciences*, 202(1):50–71, 2014.

[10] N.M. Desai and W.R.B. Lionheart. An explicit reconstruction algorithm for the transverse ray transform of a second rank tensor field from three axis data. *Inverse Problems*, 32, 2016.

[11] N.M. Desai, W.R.B. Lionheart, M. Sales, M. Strobl, and S. Schmidt. Polarimetric Neutron Magnetic Field Tomography : a non-Abelian ray transform.

[12] G. Eskin. On non-abelian radon transform. *Russ. J. Math. Phys*, 11(4):391–408, 2004.

[13] I.M. Gelfand, R.A. Minlos, and Z.Y. Shapiro. *Representations of the Rotation and Lorentz Groups and their Applications*. Martino Fine Books, 2012.

[14] J. Hadamard. Sur les Problmes aux Drives Partielles et Leur Signification Physique. *Princeton University Bulletin*, 13:49–52, 1902.

[15] B.C. Hall. *Lie Groups, Lie Algebras, and Representations: An Elementary Introduction, Graduate Texts in Mathematics*. Springer, 2015.

[16] P.C. Hansen. *Rank-Deficient and Discrete Ill-Posed Problems : Numerical Aspects of Linear Inversion*. SIAM, Philadelphia, 1998.

[17] P.C. Hansen. Regularization Tools Version 4.0 for MATLAB 7.3. *Numerical Algorithms*, 46, 2007.

[18] S. Helgason. *The Radon Transform*. Birkhauser Basel, 1999.

[19] M. Hochhold, H. Leeb, and G. Badurek. Tensorial Neutron Tomography : a first approach. *Jornal of Magnetism and Magnetic Materials*, 157-158:575–576, 1996.

[20] F Jacobs, E Sundermann, B De Sutter, M Christiaens, and I Lemahieu. A fast algorithm to calculate the exact radiological path through a pixel or voxel space. *Journal of computing and information technology*, 6(1):89–94, 1998.

[21] A.C. Kak and M. Slaney. *Principles of Computerized Tomographic Imaging*. SIAM, Philadelphia, 2001.

[22] N. Kardjilov, I. Manke, M. Strobl, A. Hilger, W. Treimer, M. Meissner, T. Krist, and J. Banhart. Three-dimensional imaging of magnetic fields with polarized neutrons. *Nature Physics*, 4:339–403, 2008.

[23] S.G. Kazantsev and A.A. Bukhgeim. Singular value decomposition for the 2D fan-beam Radon transform of tensor fields. *Journal of Inverse and Ill-posed Problems*, 12(3):245–278, 2004.

[24] Alexander M. Korsunsky, Nikolaos Baimpas, Xu Song, Jonathan Belnoue, Felix Hofmann, Brian Abbey, Mengyin Xie, Jerome Andrieux, Thomas Buslaps, and Tee Khin Neo. Strain tomography of polycrystalline zirconia dental prostheses by synchrotron X-ray diffraction. *Acta Materialia*, 59(6):2501 – 2513, 2011.

[25] H. Leeb, M. Hochhold, G. Badurek, R.J. Buchelt, and A. Schricker. Neutron Magnetic Tomography : A Feasibility Study. *Australian Journal of Physics*, 51(2):401–413, 1998.

[26] W.R.B. Lionheart and V.A. Sharafutdinov. Reconstruction algorithm for the linearized polarization tomography problem with incomplete data. In *Imaging microstructures*, volume 494 of *Contemp. Math.*, pages 137–159. Amer. Math. Soc., Providence, RI, 2009.

[27] W.R.B Lionheart and P.J. Withers. Diffraction tomography of strain. *Inverse Problems*, 31(4):045005, 2015.

[28] P. Maass. The Xray transform : singular value decomposition and resolution. *Inverse Problems*, 3, 1987.

[29] I. Manke, N. Kardjilov, M. Strobl, A. Hilger, and J. Banhart. Investigation of the skin effect in the bulk of electrical conductors with spin-polarized neutron radiography. *Journal of Applied Physics*, 104.

[30] F. Monard. Efficient tensor tomography in fan-beam coordinates. *arXiv:1510.05132v2 [math.AP]*, 2015.

[31] F. Natterer. *The Mathematics of Computerized Tomography*. Classics in Applied Mathematics. Society for Industrial and Applied Mathematics, 2001.

[32] R.G. Novikov. On determination of a gauge field on $\mathbb{R}^d$ from it's non abelian radon transform along oriented straight lines. *Journal of the Institute of MAthematics of Jussieu*, 1(4):559–629, 2002.

[33] R.G. Novikov. On iterative reconstruction in the nonlinearized polarization tomography. *Inverse Problems*, 25, 2009.

[34] R.L. Parker. *Geophysical Inverse Theory.* Princeton University Press, 1994.

[35] J.I. Richards and H.K. Youn. *The Theory of Distributions - A Nontechnical Introduction.* Cambridge University Press, 1990.

[36] O. Rodrigues. Des lois géometriques qui regissent les déplacements d'un systéme solide dans l'espace, et de la variation des coordonnées provenant de ces déplacement considérées indépendant des causes qui peuvent les produire. *J. Math. Pures Appl*, 5:380–440, 1840.

[37] M. Sales et al. Three Dimensional Polarimetric Neutron Tomography of Magnetic Fields. *arXiv:1704.04887 [physics.ins-det]*, 2017.

[38] V. Sharafutdinov. The Reshetnyak formula and Natterer stability estimates in tensor tomography. *Inverse Problems, IOP*, 33-2:20pp, 2016.

[39] V.A. Sharafutdinov. *Integral Geometry of Tensor Fields.* Inverse and ill-posed problems series. VSP, 1994.

[40] V.A. Sharafutdinov. Slice-by-slice reconstruction algorithm for vector tomography with incomplete data. *Inverse Problems*, 23(6):2603, 2007.

[41] T. Shinohara et al. Quantitative magnetic field imaging by polarized pulsed neutrons at J-PARC. *Nuclear Instruments and Methods A*, 651(1):121–125, 2011.

[42] R.L. Siddon. Fast calculation of the exact radiological path for a three-dimensional CT array. *Medical physics*, 12(2):252–255, 1985.

[43] J. Singh. *Textbook on Electrotheraphy.* Jaypee Brothers Medical Publishers, 2012.

[44] M. Strobl et al. Imaging with polarized neutrons. *Physica B*, 404:2611–2614, 2009.

[45] M. Strobl, N. Kardjilov, A. Hilger, I. Manke, and J. Banhart. Topical Review : Advances in neutron radiography and tomography. *Journal of Physics D : Applied Physics*, 42, 2009.

[46] D. Szotten. *Limited Data Problems in X-ray and Polarized Light Tomography*. PhD thesis, The University of Manchester, Manchester, UK, 1 2011.

[47] A. Tremsin, N. Kardjilov, M. Strobl, et al. Imaging of dynamic magnetic fields with spin-polarized neutron beams. *New Journal of Physics*, 17, 2015.

[48] R. Woracek et al. Neutron Bragg edge tomography for phase mapping. *Physics Procedia*, 69:227–236, 2015.

[49] H. Yang, S. Gibson, and R.A. Tomlinson. Improvement of fourier polarimetry for applications in tomographic photoelasticity. *Experimental Mechanics*, 46(5):619 – 626, October 2006.

Appendix A

Supplementary Results

Integrals over $\mathbb{R}^n$

Integrals over $\mathbb{R}^n$ can be expressed as integrals over spheres by introducing polar coordinates $x = r\omega, \omega \in \mathbb{S}^{n-1}$

$$\int_{\mathbb{R}^n} f(x)\ dx = \int_0^\infty r^{n-1} \int_{\mathbb{S}^{n-1}} f(r\omega)\ d\omega\ dr. \tag{A.1}$$

Fubini's Theorem

One may switch the order of integration if the double integral yields a finite answer when the integrand is replaced by its absolute value. If $\mathcal{X}$ and $\mathcal{Y}$ are well defined spaces and $f(x, y)$ is $\mathcal{X} \times \mathcal{Y}$ integrable meaning that it is measurable and

$$\int_{\mathcal{X}\times\mathcal{Y}} |f(x, y)|\ d(x, y) < \infty, \quad \text{then} \tag{A.2}$$

$$\int_{\mathcal{X}} \left(\int_{\mathcal{Y}} f(x, y)\ dy\right)\ dx = \int_{\mathcal{Y}} \left(\int_{\mathcal{X}} f(x, y)\ dx\right)\ dy = \int_{\mathcal{X}\times\mathcal{Y}} f(x, y)\ d(x, y). \tag{A.3}$$

Cauchy Schwartz Inequality

For L^2, we have

$$\left|\int_{\mathbb{R}^n} f(x) g\bar(x)\ \mathrm{d}x\right|^2 \quad \leq \quad \int_{\mathbb{R}^n} |f(x)|^2\ \mathrm{d}x \cdot \int_{\mathbb{R}^n} |g(x)|^2\ \mathrm{d}x. \tag{A.4}$$